The Angular Momentum of Fission Fragments and its Effects on Neutron-Gamma Emission

by

Stefano Marin

A dissertation submitted in partial fulfillment
of the requirements for the degree of
Doctor of Philosophy
(Nuclear Engineering and Radiological Sciences)
in The University of Michigan
2022

Doctoral Committee:

Professor Sara A. Pozzi, Chair
Professor Igor Jovanovic
Dr. Vladimir A. Protopopescu
Professor Thomas Schwarz
Dr. Ramona L. Vogt

Stephan (left) and Stefano (right) in 2021.

Stefano Marin

stmarin@umich.edu

ORCID iD: 0000-0001-8219-1063

To M. Stephan Okar.

To the people who made this work possible, and those who will expand upon it.

ACKNOWLEDGEMENTS

This dissertation would not have been possible without the help of the incredible people I have had the pleasure of working with. First and foremost, I wish to thank Mustapha Stephan Okar, who worked intensely with me to solve the event-by-event problem, which I consider the hardest problem I have had to solve in my Ph.D.

Students

I also want to particularly acknowledge the undergrad students that I have worked with: Isabel Hernandez, Eoin Sansevero, Katie Ballard, James Baker, Caiser Bravo. I have had the pleasure of working and meeting these students while they were still freshmen, and in one case earlier than that. These students have been fundamental parts of my research, and I wish them the best in their future.

I want to thank all my graduate student peers in my group, singling out Christopher Meert (the MCNP wizard), Leah Clark, and Michael Hua. I have the pleasure of calling them my friends. All three have been very helpful in my research, each in their own different way.

The graduate student mentors that I had the pleasure of working with are Drs. Matt Marcath and Tony Shin, who taught me that there is a difference between being creative and having your head in the clouds. Thanks to them, my feet are on the ground. All these students and friends have made me feel welcome in this environment that I have grown to call my home. Patricia Schuster, a postdoc in our group at the time, helped me to think about research in a more holistic way, and not to obsess over small problems and losing track

of the big goals.

I believe that good research is one that pushes boundaries; sometimes there is already something or someone on the other side. In these situations, the goal of the research is then to tear down this wall. I am grateful to my friends outside of my group, Kyle Beyer, Matt Petryk, Maris Arthurs specifically, with whom I have had very productive discussions.

Lastly, I am thankful for Nathan Giha, my Ph.D. mentee. Nathan and I started working together after he told me that he wanted to do something more aligned with his interest in fundamental physics. I hope I have provided an environment for you to pursue your dreams. I am proud to see you work hard and climb upwards every day. Just remember to pause once in a while, and enjoy the view from where you already are.

Mentors

I want to thank Prof. Pozzi for taking a chance on me and accepting me into her research group. Admittedly, I don't believe I was the best candidate: I did not attend the most prestigious school for my undergrad, and I did not know the first thing about nuclear engineering. Michigan was the only school where I had a chance to visit, and I was ready to leave science entirely when my meeting with Dr. He, my only scheduled meeting, did not go very well... Serendipitously, Prof. Pozzi and I met and struck up a conversation during lunch, which led to me coming to Michigan. I am forever grateful for this opportunity, and I hope I lived up to her expectations. I hope to one day be able to give this same opportunity to someone.

Vlad and I met at the very beginning of my Ph.D. while he was visiting our department, and Angela Di Fulvio, a good friend and great researcher in our group at the time, introduced me to him. I had recently written a ridiculously long document detailing the inversion of a binomial response, and was sure that this was worthy of a Ph.D., even though I had been in the program for a little more than a month. Vlad listened to me, and then proceeded to show me how of the more than ninety pages I had written on the subject, I really only

needed less than one. My relationship with Vlad has evolved over the years, but looking at it in hindsight, it continued to be variations of this same theme set in our first meeting. I would bring in a comically inflated write-up for some new mathematical models, he would listen and read every sentence and equation carefully, and by the end I would end up with a paragraph or two of salvageable material to be used in a paper. I have learned - or, more accurately, I am learning - the value of conciseness and clarity from Vlad. I find it amusing to think that, after reading this paragraph, he is probably thinking that a simple "thank you Vlad for being the only person who has read every equation" would have sufficed.

I first met Ramona at the FIESTA conference in 2017. After she gave her presentation on FREYA, she came to sit next to me, all the way back in the conference room. I was very impressed by the talk, although at the time I knew more about Norse mythology than I did about fission. Of course, as is known to anybody who has been in a video-conference with Ramona, by inviting Ramona you often get Jørgen for free, usually just walking in the background and speaking from the other room (Jørgen always appears to be in the room with the worse internet connection). My collaboration with Ramona, Jørgen, and FREYA has been one of the most rewarding in my experience as a student. I admire both of them, and have learned so much from working with them and hearing their feedback. Thank you for being my mentors and my friends during these past few, crazy years.

One of the hardest thing I have had to do as a Ph.D. student was to perform an experiment measuring fragments in coincidence with neutrons and γ rays. It seemed like everybody wanted this experiment to happen, but somehow hidden forces were keeping it from ever starting. I gave a talk in June 2019 in Raleigh, North Carolina. I expressed my interest in performing an experiment with a fragment detector. Fredrik Tovesson approached me after the talk and said he would be interested in this, and that we should keep in touch. At the time I did not realize it, but this was to be one of the most important chance meetings in my Ph.D. career. The following year, Fredrik, who was now physics director at Argonne, spear headed the project and assembled a team of some of the greatest experimental scientists I

have had the honor of working with: Ivan Tolstukhin, Russell Knaack, Michael Oberling, Benjamin Kay, and Matt Gott. Together, throughout 2020 and 2021 we met regularly once a month to discuss the design of a new ionization chamber. Fredrik made experimental science sound possible, he is genuinely interested in the research, and knows how to get things done. I simply followed his lead, and I ended up performing the experiment I had dreamed about for years. Thank you Fredrik for making dreams come true, and thank you to all the people you have assembled to work on this incredible project. I hope one day I will be able to come work with all of you at Argonne.

Project collaborations

My first thanks goes to Paul Glässel and Darren Bleuel. I remember the excitement I felt when Paul sent me the unpublished version of Schmid-Fabian dissertation, in German, and I would spend hours translating it and learning about this great experiment of the past. Both Paul and Darren showed me kindness when I was lost in my research. Thanks to your help I found consistency and logic in chaos. In hist last email to me, Paul wished me good luck, but specified that the German "viel erfolg" expresses a feeling more profound than just wishing luck. It is the wish that hard work will bear fruits.

I have already thanked Stephan at length, but his contributions to the event-by-event project merit another mention. We spent many late nights writing on whiteboards, blackboards, cardboard, and wooden boards. Our relationship with work was not healthy, but we climbed the mountain together. I am happy to see that we have both found a way to live with this past.

I thank the developers of the codes that I have used in my analysis. Apart from Ramona and Jørgen, I want to thank Ionel Stetcu, Amy Lovell, and Patrick Talou at Los Alamos, and Olivier Litaize, Olivier Serot, and Abdelhaziz Chebboubi at CEA in France. I hope my collaboration with all of you will continue in the future. The work that both of these teams put in their codes will surely not go unnoticed. I also want to thank Patrick Talou

specifically for being one of the kindest people I have met in my entire life.

I thank the Chi-Nu team at Los Alamos: Matt Devlin, Keegan Kelly, and John O'Donnell. The month I spent at Los Alamos was one of the best experiences of my doctorate. All three of you have been kind and helpful, ready to spend time discussing, and always looking for ways to collaborate. I hope our collaborations will continue in the future.

Building the FS-3 was not an easy task. I want to thank Scott at the UM-LSA machine shop for working with Stephan, and Marco Locatelli at CAEN for helping set up the electronics of the system. Leah Clark helped set up hardware and testing. Too many people to name have worked on the projects that lay the foundation to this array, and I want to thank all of you. Paul Hausladen and Jason Nattress allowed us to come test the detector system in February 2020, and lent us a Cf source later that year. This collaboration was fundamental in creating this detection system.

Building the ionization chamber was an unforgettable experience. Ivan, Michael, and Russell could lead their own space program if they wanted to. I hope I have provided something valuable to our collaboration, although I believe my main role was to simply ask for less material on the chamber walls. I often felt like a Formula-1 pilot working with a team of the best engineers in the world. You built a great machine, and now it is my turn to drive it and get the trophy.

Further acknowledgements are provided in each chapter.

Conclusions

I thank my family and friends for their support throughout this. I have been absent to a lot of you the past five years, and I hope to make it up to you all. As my grandmother Angela would say, "semper ad meliora". Even though I think I have made progress in answering the question of angular momentum in fission, the question remains open. Only because the question has a decades-long history, it does not mean that we cannot hope to solve it within the next one or two years. To Kyle, Nathan, Isabel, and Dorthea, I wish to you "viel erfolg".

TABLE OF CONTENTS

LIST OF FIGURES

Figure

ABSTRACT

The emission of neutrons and γ-rays accompanying nuclear fission is a process that has been intensely studied since the discovery of fission. Surprisingly, some of the aspects of n-γ emission are still largely unknown and thus hard to model. The obstacle that hinders our efforts to model n-γ emission is the role played by the fragments' angular momenta. The characterization of this intrinsic property of the fragments is experimentally challenging and, as a result, the experimental evidence is riddled with inconsistent observations.

The purpose of this dissertation is to work towards a resolution of the issue of angular momentum in fission. We proceed to do so by presenting experimental and theoretical evidence of the effects of angular momentum on n-γ multiplicities, energy, and angular distribution, which are the observables of interest in fission modelling. We analyze data from three experiments, looking at three different observables regarding the correlations of fragment angular momenta with excitation energy. The first result is an event-by-event analysis of n-γ correlations in ^{252}Cf(sf), measured with the Chi-Nu array at Los Alamos National Laboratory. The second result, also collected with Chi-Nu, is an analysis of γ-ray emission with incident neutron energy in ^{239}Pu(n,f). Lastly, we have performed an experiment using an array of organic scintillators, the FS-3, in coincidence with a twin Frisch-gridded ionization chamber, a sensitive fragment detector.

The results of this dissertation have revealed a relationship between angular momentum and excitation energy that is more complicated than previously suspected. In fact, we find evidence of a saturated angular momentum mechanism; the angular momentum depends on the excitation energy of the nucleus only up to a certain energy, above which the angular momentum remains constant. We have also determined that while the angular momentum

is usually polarized in a plane perpendicular to the fission axis, there exist significant depolarization effects when one of the fragments approaches sphericity. Finally, we explain the observations made in this dissertation by introducing a theoretical model of angular momentum generation based on longitudinal vibrational modes of fissioning systems.

The mechanism we propose leads to fragment angular momenta that are predominantly parallel to one another, an observable that will be pursued in future work. Furthermore, we also explain how in induced fission larger values of fragment angular momenta can be reached. The results of this dissertation shed light on the importance of the scission process in determining the fragment angular momenta, an important theoretical challenge. Throughout, we also show the impact that angular momentum has on the emission and measurement of neutrons and γ rays, an important practical and technological challenge.

CHAPTER I

Introduction

In this dissertation, we study the emission of neutrons and γ rays accompanying fission in order to understand the role that the fragment angular momentum plays in fission. It is known that the angular momentum regulates the emission of γ rays, determining to a large extent their multiplicity [1, 2, 3], as well as their angular distribution [4, 5, 6]. In fact, the fragments' angular momenta act as antennae with reference to which the electromagnetic radiation, *i.e.* the γ rays, are emitted. While much is still unknown about the fission fragment angular momenta, in recent years a renewed interest in the precise modeling of γ rays in fission [7, 8] has sparked research in this field.

Understanding the generation of angular momentum in fission remains one of the last open questions in fission physics [9]. Scientifically, understanding angular momentum generation will help us understand the shape evolution in fission, and answer the question of how nuclei undergo fission in the first place. Improved models of angular momentum also have important applications in areas of nuclear nonproliferation, where coincident measurements of radiation from fission are used to identify and characterize nuclear material.

The work presented in this dissertation focuses on the dependence of the fragment angular momenta on the fragment excitation energy. Understanding this relationship is an important step in modeling the correlations between neutron and γ ray emission. The analysis of three experiments will be shown in this dissertation. In Chapter II, we analyze the event-by-event

n-γ correlations in ^{252}Cf(sf) collected with the Chi-Nu array in Los Alamos. In Chapter III we analyze the emission of γ rays from the ^{239}Pu(n,f) reaction, also collected with Chi-Nu. Lastly, in Chapter IV, we present the results of an experiment we conducted using a fragment-sensitive ionization chamber and an array of organic scintillators in collaboration with Argonne National Laboratory.

Unless otherwise stated, J represents the total angular momentum of the two fragments, *i.e.* the sum of the two angular momenta magnitudes, and E^* represents the total excitation energy, which has alternatively been called TXE in the literature. The results of the experiments presented in this dissertation point to the existence of an energy dependence of the angular momentum, J, on the total excitation energy E^*. The relationship is, however, more complex than previously suspected.

The relationship between E^* and J that we uncover here sheds light on previously unknown aspects of the fission process. The central question we wish to address is how a system with no angular momentum spontaneously decays to fragments possessing angular momenta, with the fragment orbital motion be such that angular momentum is conserved. Why should the fragments have any angular momentum at all? Why do the fragment angular momenta appear to be uncorrelated? What is the relative direction of the fragment angular momenta? We attempt to provide an answer to these questions in Chapter V, where experimental and theoretical results are distilled and summarized. Much more will need to be done to properly understand the fission process, but the work we show here will be of value to future students of this topic.

1.0.1 Overview of fission

The nuclear fission reaction begins with the deformation of the nucleus and leads to the emission of two large fragments and the release of a large amount of energy [10]. The most important aspect of the fission process in this dissertation is that the fragments emitted in fission are in excited states. In fact, while most of the total energy of fission, denoted

Q, is released in the form of the fragment kinetic energies, a fraction is found as fragment excitation energy E^* [11]. It is also experimentally known that fragments are also imbued with angular momentum J [4, 5, 6]. Angular momentum is a fundamental property of quantum mechanical objects that dictates the rotational symmetries of the wave function describing the system. Nonetheless, one can also understand angular momentum classically, as rotational motion around the direction of the angular momentum vector. An important property of angular momentum is that it is a quantized quantity, *i.e.*, it can only take on discrete multiples of the fundamental unit of angular momentum, $\hbar$.

The fission process can be divided in two parts: the *scission* stage, and the *de-excitation* process. The scission stage encompasses the processes by which an initial nucleus separates into two fragments. Scission calculations usually include microscopic forces between nucleons [12], or nuclear shape parameters [11], that are capable of predicting the deformation of nuclei. The main observables predicted by these codes are the fragment masses, kinetic energies, excitation energies, and angular momenta. The de-excitation processes begin immediately following scission. The excited states of fragments are short lived and promptly decay by neutron emission followed γ-ray emission, with this emission happening almost simultaneously with the fission event, 10^{-19} - 10^{-8} s. Because of their neutron excess, the fragments further undergo β-decay at much later times, starting at $\sim 10^{-3}$ s. These β decays are followed by emissions of neutrons and γ rays, which appear to be delayed with respect to the fission event. This dissertation will focus on the prompt n-γ emission.

We illustrate in Fig. 1.1 how the initial state of a fission fragment, in both excitation energy, E^*, and angular momentum, J, affects the subsequent emission of neutrons and γ rays. In Fig. 1.1 we illustrate an initial fragment E^*-J and its de-excitation, in the form of the emitted neutrons and γ rays. We note that, differently from the notation used later in this dissertation, the E^* and J in the figure refer to single-fragment properties. Neutrons are emitted by fission fragments as long as the intrinsic excitation energy is larger than the neutron separation energy. Some n-γ competition is expected in the vicinity of the neutron

separation energy. The intrinsic excitation energy is the energy that is not stored in collective nuclear motion, such as the energy associated with the fragment angular momentum. After having emitted all neutrons, the fragment dissipate the remainder of their intrinsic energy through statistical γ-ray emission. These transitions occur between states in the quasi-continuum of levels, and thus their emission can be treated statistically. Finally, when the fragment has sufficiently low energy and the density of states is significantly lower, collective γ-ray emissions de-excite the fragment to its ground state, or a long-lived isomeric state. Collective emission along rotational band is conventionally of electric quadrupole character, denoted as $E2$, and each emission removes $2\hbar$ of angular momentum from the fragment. The emissions removing the maximum allowed amount of angular momentum are known as *stretched*.

The central aim of this dissertation is to determine whether there exist correlations between the total excitation energy E^* and the total angular momentum J. For a single fragment, we can visualize the E^*-J relationship as a tilt in the initial fragment conditions, as indicated in Fig. 1.1. Thus, E^*-J correlations are a product of the scission process. Nonetheless, as we shall see in this dissertation, they also give rise to interesting emission patterns and are thus crucial to the description of the de-excitation process.

Very little is known regarding a relationship between E^* and J. In a seminal paper, Wilhelmy *et al.* [5] examined the yield of known γ-ray transitions for different excitation energies, and claimed that there are no noticeable E^*-J correlations within an error of $1 - 2\hbar$. However, over the decades experimental evidence has mounted for the existence of these correlations, not all in agreement with each other. For example, Nifenekcer *et al.* [3] and Schmid-Fabian *et al.* [14], both determined positive linear correlations, but of vastly different magnitude. More recently, the experimental investigations by Wilson *et al.* [7] and Travar *et al.* [8], found strong correlations between fragment deformations and angular momenta, indicating a possible E^* dependence. Lastly, the results of Chebboubi *et al.* [15] and Gonnenwein *et al.* [9] indicate that the angular momentum of fission fragments, while

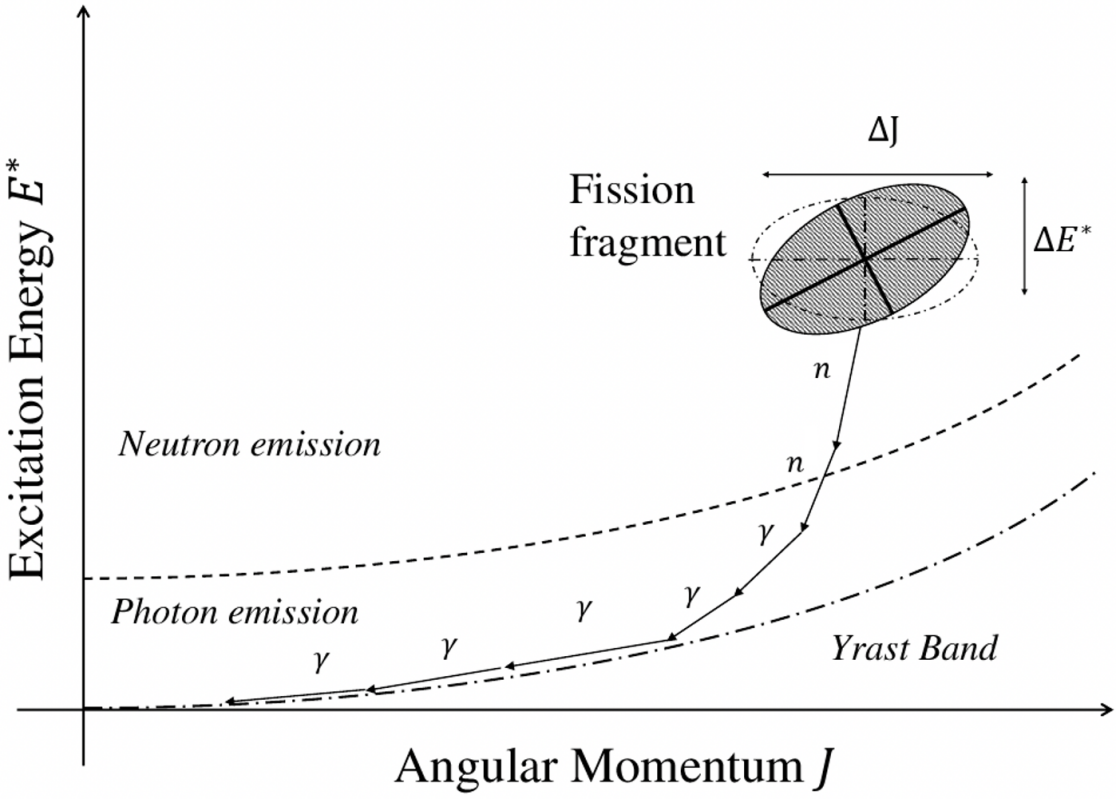

Figure 1.1: The excitation and de-excitation process of fragments can be viewed on the $E^* - J$ diagram. The initial distribution of excitation energy and angular momentum, with possible correlations, is shown as a shaded ellipse. The emission of prompt neutron and γ rays de-excites the fragments. Correlations in the emission of neutrons and γ rays is connected to correlations in the initial fragment distribution [13].

low on average, correlates strongly with excitation energy.

1.0.2 Outline

In Chapter II we begin by proving the existence of event-by-event emission correlations between neutrons and γ rays in ^{252}Cf(sf). These results show not only multiplicity correlations, but correlations between neutron and γ-ray spectra and angular distributions as well. We interpret the results as indicating the existence of E^*-J correlations and the polarization, *i.e.*, an alignment, of the fragment angular momenta in a plane perpendicular to the fission axis. However, due to the nature of the experiment, these observations are representative of

average fission events, in both fragment masses and excitation energy.

In Chapter III we continue our investigation by considering the dependence of γ ray emission on incident neutron energy in ^{239}Pu(n,f). The observed emission correlations indicate once again the existence of E^*-J correlations. Being able to select events with specified incident neutron energy, we find that the linear relationship holds over a larger energy range than could be determined in Chapter II.

In Chapter IV, we perform the most important experiment of this dissertation, involving the measurement of fission fragments in coincidence with the emissions of neutrons and γ rays. The results of this experiment give us an unprecedented insight into E^*-J correlations. While we confirm that on average the angular momentum positively correlates with E^*, we have also determined that these correlations disappear at sufficiently large E^*. We also have determined a reduction of angular anisotropy of γ rays when either of the two fragments approaches sphericity.

In Chapter V, we frame the experimental results of this dissertation and discuss them in light of past experimental evidence. We use these observations to put forward the basis of a mechanism of angular momentum production based on the vibrational motion of the nucleus. Conclusions and future work are discussed in Chapter VI.

CHAPTER II

Event-by-Event Correlations

The results of this chapter will show that there exist positive event-by-event correlations between neutron and γ-ray emission. These correlations, not only in n-γ multiplicity but also between their spectra and angle of emission, suggest the existence of positive correlations between the excitation energy, E^*, and the angular momentum, J. Due to their nature, event-by-event correlations receive contributions from all the fission characteristics that vary between events, *e.g.* fragment mass, energy, the specific de-excitation paths, and quantum-mechanical competition. For this reason, in this chapter, the connection between E^*-J correlations and n-γ correlations are mostly qualitative.

In Section 2.1 we present the experimental setup, the Chi-Nu liquid scintillator array at the Los Alamos Neutron Science Center (LANSCE). The main characteristics of this system are presented without delving too deeply in the details of how each detector performs. Discussion of these finer details can be found in the literature regarding Chi-Nu [16, 17]. In Section 2.2 we present the results of the event-by-event analysis. The goal of this section is to show the energy-differentiated and directionally-differentiated correlations. We present model calculations and previous experimental results in parallel with the results of our analysis. In Section 2.3, we discuss the results of this experiment and their implications on E^*-J correlations.

2.1 Experimental setup

The experimental determination of event-by-event n-γ correlations hinges on the simultaneous measurement of neutrons and γ rays in a fission event. The purpose of this section is to present the experimental apparatus used, both in its physical form as well as in its mathematical representation as a system response.

2.1.1 Setup

The experimental determination of n-γ emission correlations is based on an analysis of data collected using the Chi-Nu array at LANSCE. The data was collected by Matthew Marcath and collaborators at LANSCE in 2015 [17]. The detector array is intended to be a neutron spectrometer, but the data collected using the array of organic scintillators has also been analyzed for n-γ correlations. A detailed description of the experimental system is provided by Marcath *et al.* [17].

The detector array, pictured in Fig. 2.1, consists of 54 EJ-309 liquid organic scintillation detectors. Each detector is a right circular cylinder with a diameter of 17.78 cm and a depth of 5.08 cm. The detectors are arranged in a hemispherical geometry, with each detector face at a distance of approximately 1 m from the center of the hemisphere. Variations of 1-3 cm in this average distance are recorded for each detector. The detectors are arranged in nine arches, each consisting of six detectors.

The fission source in the experiment is a hemispherical-plate ionization chamber designed and fabricated at Oak Ridge National Laboratory in 2010 [18]. Following a fission event, one or both of the fission fragments traverse the small ~ 1 mm gap between two hemispherical electrodes, depositing a fraction of their energy through ionization of the gas. A diagram of the ionization chamber used in this experiment is shown in Fig. 2.2.

A general concern when designing and characterizing a fission trigger is the capability of distinguishing between α decays and fission events. For most isotopes of interest, the branching fraction for α decay is many times larger than the branching fraction for fission.

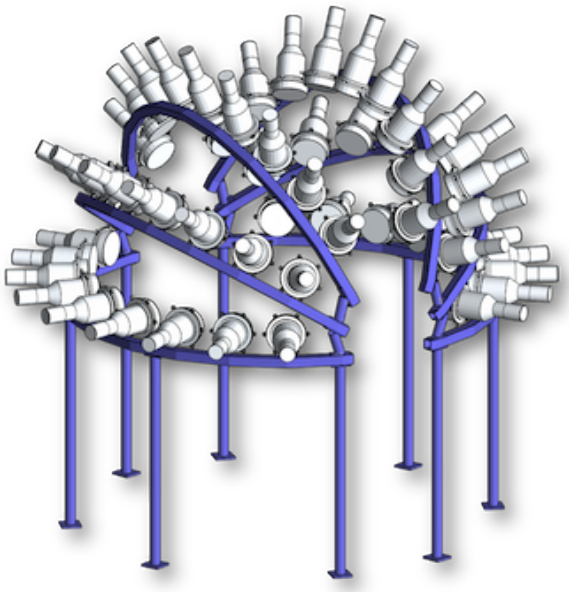

Figure 2.1: Schematic drawing of the Chi-Nu detector array. The detectors are EJ-309 liquid organic scintillators mounted on photo-multiplier tubes (PMTs). The fission source sits at the center of the hemisphere, at a distance of 1 m from each detector.

In the case of ^{252}Cf, an isotope known for its high specific fission activity, the fission branching fraction is 3.09 %: the rest of the decays are α decays. Other common fissionable isotopes used in fission experiments, such as plutonium and uranium isotopes, have much higher α decay branching fractions. For this reason, it is important in all fission experiments to characterize the expected contamination of data due to α emission. While neither α decays nor fission fragments are fully stopped in the chamber, the stopping power of fission fragments is much higher due to their significantly higher electric charge [18]. Therefore, the signal from the ionization chamber can be analyzed in pulse-height analyses, and a simple energy threshold can eliminate virtually all α decays.

At the time of the measurement, the fission activity of the source was $\gtrsim 99.7$ % ^{252}Cf(sf), with the primary contamination from ^{250}Cf(sf) and negligible rates of ^{248}Cm(sf). The ionization chamber used in this experiment provides a fission time t_0, with an excellent timing resolution with standard deviation of $\sigma(t_0) \approx 0.5$ ns.

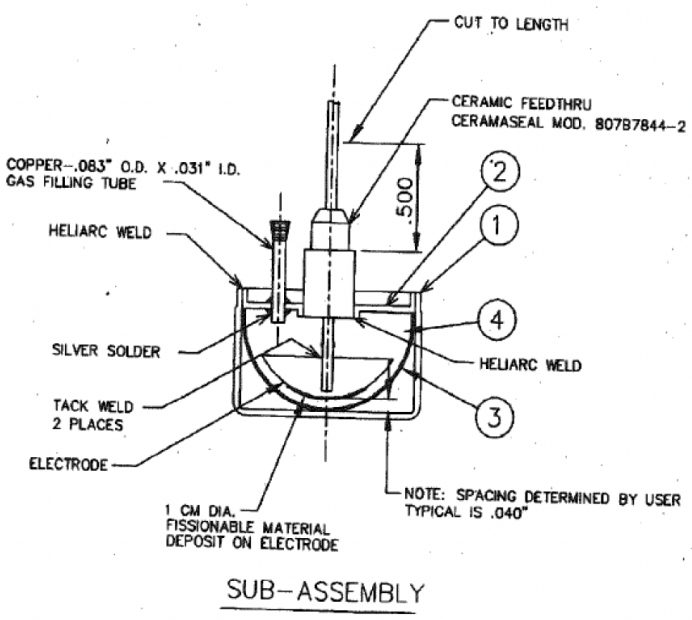

Figure 2.2: The fission detector used in the experiment. The ^{252}Cf source is placed between two hemispherical electrodes. Fission fragments and α decays deposit a fraction of their energy in the small gas-filled spacing between the two hemispherical electrodes. The signal produced by the detector is proportional to the stopping power of the detector and is capable of discriminating fission fragments from α particles.

The Chi-Nu liquid organic scintillators are sensitive to both neutron and γ radiation. Neutrons are detected by elastic scattering on hydrogen nuclei, while γ rays interact through Compton scattering on the atomic electrons. Furthermore, the material of the detector, EJ-309, is capable of pulse-shape discrimination (PSD). Specifically, the scintillation process for the protons scattered by neutron interactions leads to a larger component of *delayed fluorescence* compared to the electrons scattered by γ rays, which instead lead predominantly to *prompt fluorescence*. The pulses generated can be analyzed by charge integration and the type of particle inducing the interaction can be determined on an event-by-event basis.

The integral over time of a voltage pulse generated in the scintillation detector provides an estimate of the total scintillation light produced in an event. Similarly, the integral taken only over the tail of the pulse, *i.e.* after the pulse peak, can be optimized to yield a higher ratio of delayed-fluorescence scintillation. The ratio of the tail integral to the total integral

gives an estimate of the ratio of delayed-fluorescence scintillation to total scintillation and can thus be used to discriminate between neutron and γ-ray interactions. An example of PSD analysis, from Ref. [17] and for the data analyzed in this chapter, is shown in Fig. 2.3.

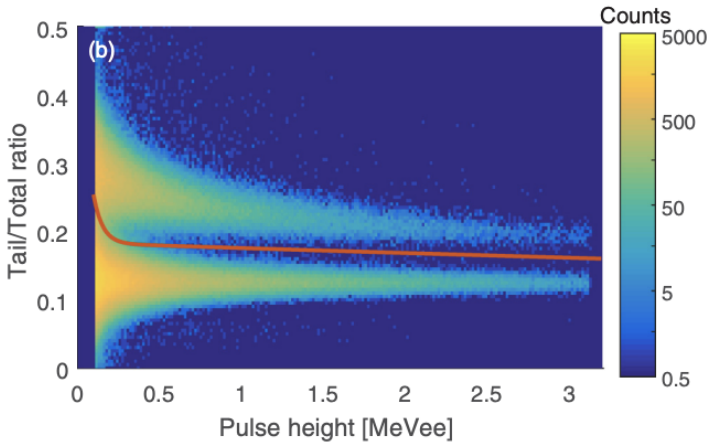

Figure 2.3: Neutron and γ-ray interactions in organic scintillators can be discriminated by analyzing the fraction of delayed scintillation light to the total light output. This plot shows the ratio of the integral of the scintillation pulses over a time-delayed window (tail) to the total integral of the pulse, as a function of the total light output. Figure reproduced from Ref. [17].

Scintillation detectors provide excellent timing for radiation interactions. The signal from the detectors is digitized using CAEN V1730 digitizers, with a sampling rate of 500 MHz, a dynamic range of 2 V, and 2^{14} ADC channels on this range. The signal timing is determined through digital constant fraction discrimination (dCFD) in post-processing, thus achieving a higher resolution than the time-frequency of the digitization rate. The detector time resolution is determined to be ≈ 0.6 ns. The determination is performed using both a coincident ^{22}Na source as well as by fitting the γ-ray peak in the time of flight (ToF) distribution collected during the experiment.

Due to the relatively poor PSD performance of EJ-309 at low energies, a threshold of 100 keVee is applied to the interactions. At the opposite end, saturated pulses with light output greater than ≈ 3.2 MeVee are also removed due to the limited range of the digitizer acquisition window. Characterization of background is performed by looking at n-γ

multiplicity in a coincidence window before the trigger t_0 signal. The data from background is treated exactly like experimental data for energy and time differentiation. Thus, each fission trigger is used to collect both data and background. The background is determined to be small in magnitude but with strong correlations between background neutrons and γ rays. This might have been due to the presence of radioactive sources in the vicinity of the experiment.

The timing information provided by the detector is used for two purposes. The ToF, $t - t_0$, is used to further discriminate between neutrons and γ rays. Because of the long flight path of Chi-Nu, γ rays arrive at the detectors approximately 3 ns after the fission chamber signal, whereas neutrons emitted in fission are only detected $20 - 25$ ns after t_0 for the highest energy neutrons. Using both PSD and ToF discrimination, the misclassification rates between neutrons and γ rays are determined to be negligible. In addition, the neutron ToF is used for neutron spectroscopy. In fact, we can assign an event-by-event ToF energy T_n for neutrons based on their detection time,

$$T_n = \frac{1}{2} m_n \left(\frac{l}{t - t_0} \right)^2 , \tag{2.1}$$

where m_n is the neutron mass, and l is the distance from the source to the interaction vertex, *i.e.*, the position of the interaction within the detector. The nonrelativistic expression for the kinetic energy is appropriate for the energies of neutrons emitted by ^{252}Cf(sf).

The integral of the pulse generated by the interaction in the detector, related to the total scintillation light produced in the interaction, is also related to the energy deposited in the interaction. For n and γ pulses, as assigned by combined PSD and ToF discrimination, we define the total light output as F_n and F_γ, respectively.

Three digitizers are used for this experiment, each capable of digitizing 16 input channels. The ionization chamber signal is provided individually to each digitizer, occupying the first two channels of each digitizer. Therefore, the data from 42 of the 54 detectors is being analysed in this experiment.

2.1.2 Experimental response

We present here the response of the Chi-Nu detector, defined as the capability of the system to properly measure features of the emitted radiation. The system response is an important ingredient in the unfolding of experimental data. We show response matrices and resolutions of the system for the various aspects of the radiation we measure: their spectra and angular distributions.

2.1.2.1 MCNPX-PoliMi simulation

The Chi-Nu system response is determined by the properties outlined in the previous section. The absolute detection efficiencies, ϵ_n and ϵ_γ, which are source-dependent quantities, are determined using an MCNPX-PoliMi simulation [19]. The detector geometry, materials, and radiation transport physics are faithfully simulated using a detailed input for the MCNPX simulation. The MCNPX-PoliMi built-in ^{252}Cf(sf) source spectrum is used to determine the efficiency of the detector array to an energy-undifferentiated source. The source is modeled as fully isotropic. We determined a geometric coverage of $\approx 8.3\%$, while the intrinsic efficiencies are approximately 32% and 23%, for neutrons and γ rays, respectively. The resulting efficiencies of the Chi-Nu array for the fission spectrum, averaged over all energies, are $\epsilon_n \approx 2.6\%$ and $\epsilon_\gamma \approx 1.9\%$.

After sampling source particles from the simulated source, MCNPX uses Monte-Carlo radiation transport to simulate the movement of the particles within the detector geometry. For any interaction of sufficiency energy, > 0.001 MeV, PoliMi records the relevant interaction information in an output file, including the position of the interaction vertex and the energies of the reaction products.

The output file is processed using our suite of Python codes: the FAME (Fission-Angle Multiplicity Energy) code. The energy deposited in each interaction is converted to scintil-

lation light output using Birks' empirical formula [20],

$$F(E_d) = S \int_0^{E_d} \frac{dE}{1 + k_B \; dE/dx} \tag{2.2}$$

where F is the light output and E_d is the energy deposited in the interaction and transmitted to a charged particle that undergoes scintillation. The stopping power of the detector material, dE/dx, will in general depend on the energy of the particle. The parameter S serves as a calibration between the units of light output and energy, while the Birks' constant k_B, with units inverse of stopping power, is used to model the effects of light output quenching. Specifically, a charged particle depositing a lot of energy in a short distance will not be able to excite many scintillating states in the molecule. The stopping power for protons is much larger than for electrons; thus, the light output is proportional to the energy deposited by γ rays, but varies non-linearly with the energy deposited by neutrons, and is generally lower than an equivalent-energy γ-ray interaction. We express light output in units of MeVee (MeV electron equivalent) such that, for γ-ray interactions, the light output is numerically equivalent to the energy deposited. The simulated total light output is calculated by summing the light output of all scatterings the particle has undergone within the pulse rise time of the detector, 4 ns.

In order to improve the unfolding process to follow, both the distance of each detector from the source and the Birks light output parameters are tweaked in simulation until excellent agreement between the simulated and measured ToF distributions, < 5 % difference throughout. Most of the changes in the distance are within $2 - 3$ cm, which is also the uncertainty in the measurement of the geometry. The determined variations in the light output are also small and can be explained by variations in gain applied to the scintillator PMT and other material properties of the detectors.

2.1.2.2 Response matrices

As stated, the simulations based on the MCNPX-PoliMi built-in fission source inform the geometry and parameters of the simulations. This procedure introduces a bias that prevents us from presenting absolute results on the particle spectra. Notwithstanding this limitation, the goal of the present experiment is to determine correlations that will be eventually normalized to the spectrum. Therefore, while the spectra we will show are tuned to some extent to agree with reference data, the correlations maintain their independence insofar as they are related to the same reference spectra.

The energy response of the array is determined by performing simulations with monoenergetic, isotropic sources of radiation, separately for neutrons and γ rays. In the simulation, as in experiment, we measure particles energies using the γ-ray light output, F_γ in units of MeVee, and the neutron ToF energy, T_n, in units of MeV. We write the responses using the simplified notation

$$\epsilon_\gamma(E_\gamma)\frac{dE_\gamma}{dF_\gamma} \quad \text{and} \quad \epsilon_n(E_n)\frac{dE_n}{dT_n} \ . \tag{2.3}$$

The notation of Eq. (2.3) makes it clear that the response is made up of an energy-dependent efficiency term, ϵ, multiplying a differential of two spaces, namely the spaces of emitted energies E_n, E_γ, and the spaces of measured energies T_n, F_γ. Differentials of this form are matrices with components x, y given by conditional probability distribution[1]

$$\left(\frac{dY}{dX}\right)_{x,y} = \mathbb{P}\left(X = x | Y = y\right) \ , \tag{2.4}$$

where x, y are indices enumerating the elements of the discretized spaces X, Y. Matrices of this form are called *response matrices*. In the case of Eq. (2.3), the response matrix dictates the probability that a neutron (γ-ray) of emitted energy E_n (E_γ) will be measured having an energy T_n (F_γ).

[1]To be precise, this should be written in terms of a conditional differentiation of a random variable defined on the space Y. To avoid introducing otherwise unused notation, we can take Eq. (2.4) to be the defintion of the differential between two spaces

The energies of the source particles are sampled uniformly in narrow bins of width 10 keV, with bin edges ranging from 0 to 4 MeV for γ rays and 0 to 10 MeV for neutrons. The response matrices calculated in MCNPX are visualized in Fig. 2.4.

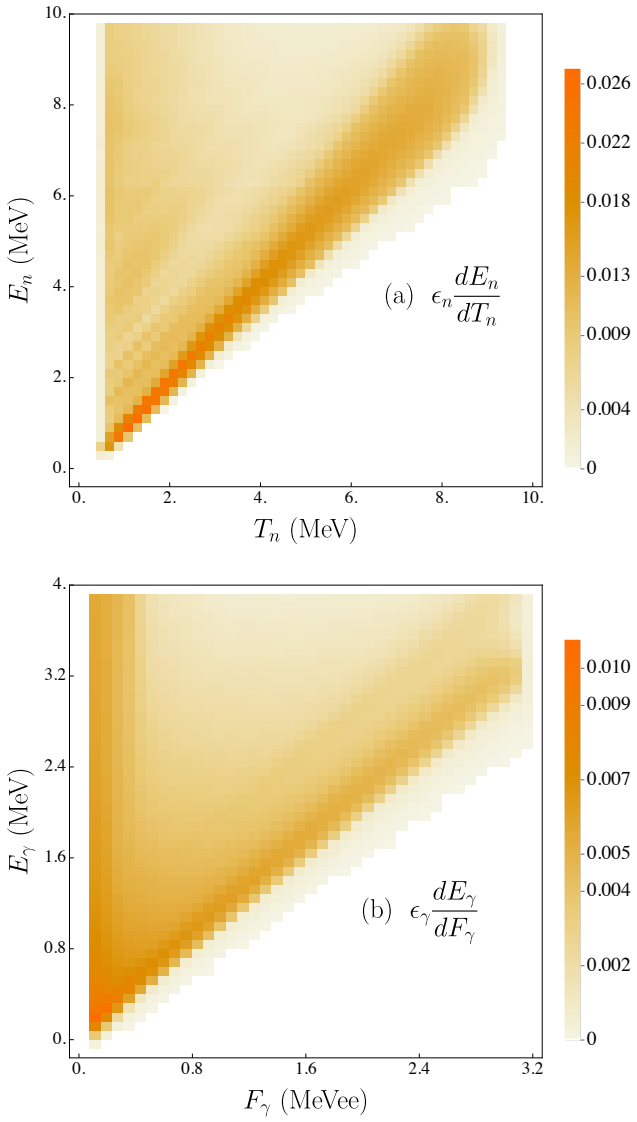

Figure 2.4: Energy response of the Chi-Nu system for (a) neutrons and (b) γ rays. The value of a matrix elements corresponds to the conditional probability distribution of measuring a single particle of a given measured energy (F_γ, T_n), given an emitted energy (E_γ, E_n).

The absolute detection efficiency of the Chi-Nu array can be readily calculated by summing the response matrix over all measured energies for a fixed incident energy. Furthermore, the absolute detection efficiencies for the fission spectra are determined by integrating the

energy-dependent efficiencies weighted by the fission spectra. The results of the efficiency analysis, including the weighting spectra, are shown in Fig. 2.5.

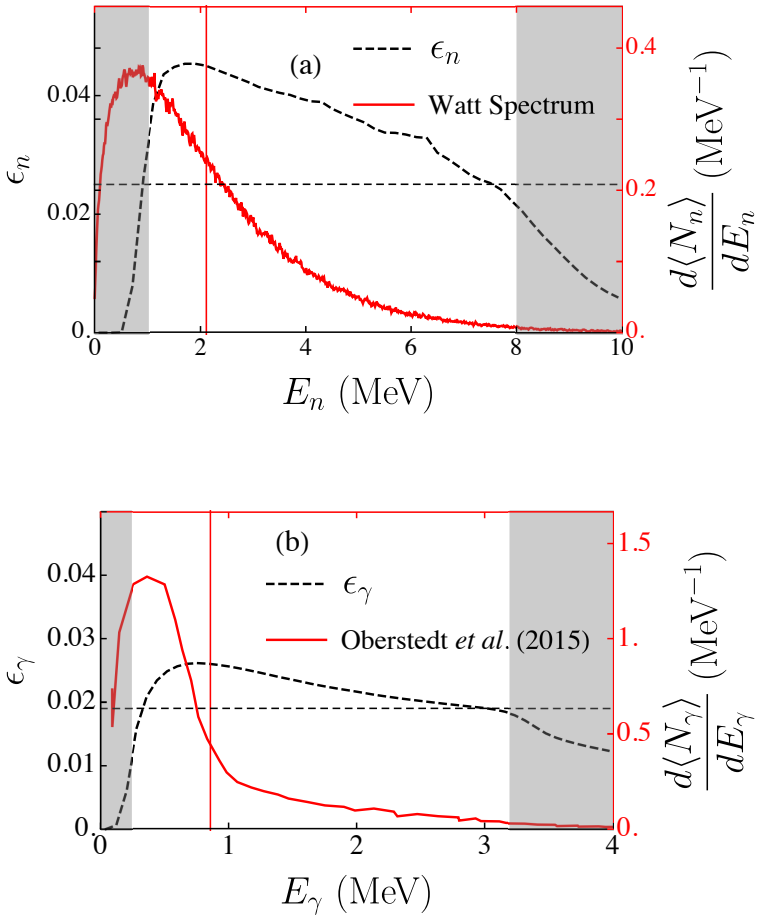

Figure 2.5: The energy-dependent absolute detection efficiencies of the Chi-Nu array for (a) neutrons, and (b) γ rays, as black lines. In red, we show the reference spectra: the MCNPX-PoliMi reference Watt spectrum for neutrons and the recent experimental data for γ rays by Oberstedt *et al.* [21]. The average energy of the reference spectrum is indicated by vertical red lines, while the efficiency averaged over the reference spectra is shown by a horizontal line. Gray bands indicate the energy-rejection region of the experiment, as determined from the unfolding procedure.

2.1.2.3 Angular response

To determine the angular response of the system we simulate the coincident detection of a neutron and γ ray. The neutron is emitted isotropically and the γ ray is emitted at

an angle $\theta_{n\gamma}$ with respect to the neutron. The azimuthal angle is sampled uniformly. To simplify the calculations, we have also assumed neutrons of energy $E_n = 2$ MeV and γ-rays of energy $E_\gamma = 0.8$ MeV, chosen because they are the average energies of the fission spectra.

As before, the response can be written as the product of two components

$$(\epsilon_n \epsilon_\gamma) \frac{d\phi_{n\gamma}}{d\theta_{n\gamma}} \ . \tag{2.5}$$

where the term in parenthesis is the product of the neutron and γ-ray efficiencies for detectors making an angle $\theta_{n\gamma}$ with one another, and the differential $d\phi_{n\gamma}/d\theta_{n\gamma}$, a matrix, represents the distribution of measured angles. We investigate the two factors separately, beginning with the matrix term.

We have determined that the systematic bias in the angular response is negligible, *i.e.*, the mean measured n-γ angle corresponds to the mean angle between them at emission. On the other hand, the angular resolution, expressed as the standard deviation of the measured angles, is significant. The angular resolution as a function of n-γ angle is shown in Fig. 2.6. The dominant source of angular resolution is emission independent and is related to the physical width of the scintillation detector, but small corrections can also arise due to the penetrability of the emission and scattering.

In n-γ experiments on spontaneous fission, there is no preferred coordinate system other than the one defined internally in each event. The fission axis is isotropically oriented in the lab frame and, without a measurement of the fragment motion, the only angle of physical significance is that between neutrons and γ rays. Thus, the analysis of the angular response of Chi-Nu begins with the analysis of the angles between any two detectors in the array. For the 42 active detector pairs, with each detector being considered either as a neutron or a γ-ray detector, we have 1722 detector pairs.

To analyze the response, we use experimental data on the product of the n-γ singles rates. The product of the rates between the detectors is proportional to the product of the individual detector efficiencies. The distribution of product efficiencies and angles between

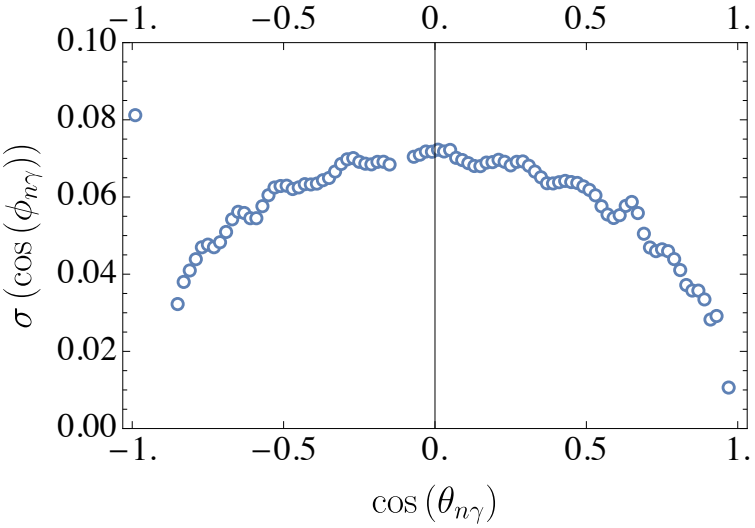

Figure 2.6: The angular resolution of the Chi-Nu array is estimated by computing the standard deviation of the simulated measured angle $\phi_{n\gamma}$ as a function of initial emission angle $\theta_{n\gamma}$.

detector pairs is shown in the top panel of Fig. 2.7, and is histogrammed in the lower panel with uniformly spaced cosine bins, providing the density of detector pairs as a function of the angle, $\theta_{n\gamma}$, between their centers. As expected from the hemispherical configuration of Chi-Nu, the detection system has more pairs making acute angles with one another than an ideal spherically symmetric configuration would have. This bias is visible in Fig. 2.7, where we find more detector pairs with $\theta_{n\gamma} < \pi/2$.

2.2 Results

The main result of this section is the triply differentiated correlation C

$$C_{E_n E_\gamma \theta_{n\gamma}} = \frac{\partial^3 \mathrm{cov}(N_n, N_\gamma)}{\partial E_n \partial E_\gamma \partial \theta_{n\gamma}} \left[\frac{\partial}{\partial \theta_{n\gamma}} \left(\frac{\partial \langle N_n \rangle}{\partial E_n} \frac{\partial \langle N_\gamma \rangle}{\partial E_\gamma} \right) \right]^{-1} . \tag{2.6}$$

This quantity is indicative of the magnitude of the n-γ multiplicity correlations, and it is simply the ratio of the covariance of n-γ multiplicities to the product of their spectra, with gates on different energies and relative angles.

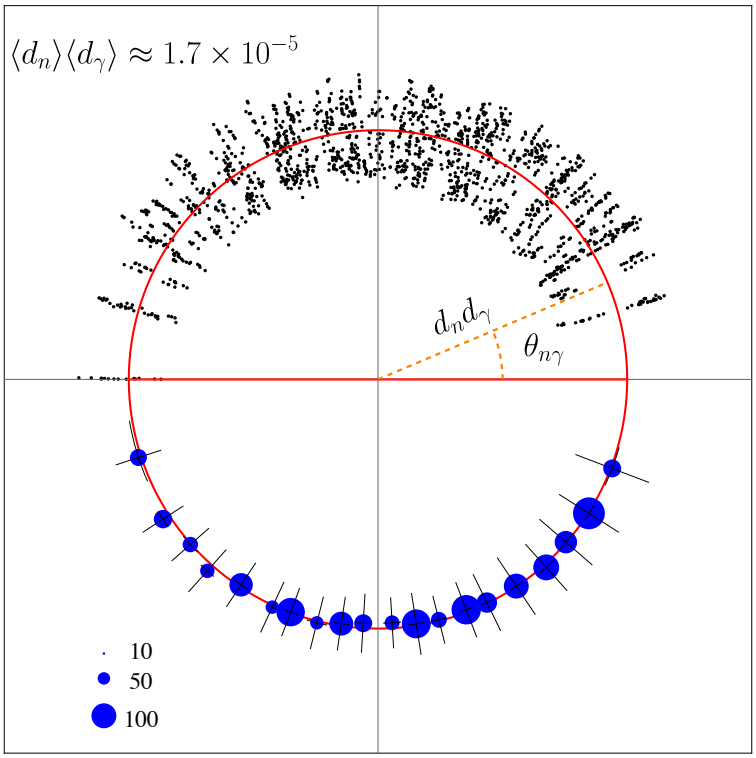

Figure 2.7: Angular efficiency plot of the Chi-Nu array. Each detector pair is represented as a black point on the top half of the figure, with the polar angle being the angle between the two detectors, and the distance from the origin being the product of the two detector efficiencies. The red line shows the product efficiency averaged over all detector pairs. In the bottom half of the figure, the detector pairs are binned with uniform cosine bins, each 0.1 in width. The radial and polar error bars show the spread in the detector-pair efficiency and angle within the bin. The size of each marker is proportional to the number of detectors in that bin, as indicated in the legend.

We present the experimental results and compare them with previous experimental data, when available, and with model calculations. The section is limited to the presentation of the experimental results and the salient patterns therein; a discussion of the physical implication is provided in the following section.

We have begun our research into the topic of event-by-event n-γ correlations [22] with undifferentiated correlations and over the years applied more and more differentiations [13, 23]. Instead of presenting the results in this chronological order, we have decided to present them in a more precise and logical manner: the final triply-differentiated correla-

tions will be presented first, after which integrations will be performed to "undifferentiate" the result. This procedure yields superior results as it eliminates many of the experimental biases associated with the system response. Each differentiated degree of freedom is unfolded, or otherwise corrected, and the integration is performed only over those ranges where the data can be trusted.

2.2.1 Differentiated correlations

Differentiations with respect to energy are performed using the γ-ray light output, F_γ, and the neutron ToF energy, T_n. We differentiate the data event-by-event using energy bins of width 0.2 MeV for neutrons, in the range $0 < T_n < 10$ MeV, and 0.08 MeVee for γ rays, in the range $0 < F_\gamma < 4$ MeVee. Differentiation with respect to angle is performed by considering cosine bins of width 0.1 in the range $-1 < \cos(\phi_{n\gamma}) < 1$. This width corresponds approximately to the angular resolution of a single pair of detectors, see Fig. 2.6. The multiplicity data for pairs of detectors in which the angle between detectors are in the same bin are then summed.

In experiment, we measure neutron and γ-ray multiplicities, D_n and D_γ respectively. The differentiated correlations are determined by treating the neutron and γ-ray multiplicity at each energy and angle as separate random variables. From the differentiated data we then obtain differentiated covariances, $\mathrm{cov}(D_n, D_\gamma)$, and products of averages, $\langle D_n \rangle \langle D_\gamma \rangle$ which now take the form of three-dimensional arrays, one for each combination of T_n, F_γ, $\phi_{n\gamma}$. Each entry in the array is independently corrected for background. The correction due to pile up, of dominant importance in the undifferentiated correlations [22], is naturally removed by angular differentiation by not considering the most forward angles in the integration. Misclassification and particle production biases have been corrected for, but these effects are found to be negligible.

We do not unfold the angular correlations, since it is found that the measurement does not introduce a bias but only broadens the angular resolution. Rather, the angular response

is corrected by using the familiar *angular attenuation coefficients* [24]. These corrections are applied to Legendre polynomial fits of the n-γ angular correlations, and are found to be only small corrections. Thus, in the following we can take $\phi_{n\gamma}$ to be equivalent to $\theta_{n\gamma}$.

The differentiated product of the averages is used in combination with the energy response matrices, Fig. 2.5, to optimize the unfolding algorithm until reference energy spectra are reproduced. The result of the energy unfolding procedure is shown in Fig. 2.8. We determine the acceptance region of the experiment based on the agreement between the unfolded spectra and the reference spectra. We have determined an energy acceptance region of $0.24 \leq E_\gamma < 3.2$ MeV and $1.0 \leq E_n < 8.0$ MeV.

The optimized unfolding procedure is then applied to the differentiated covariance between neutrons and γ rays. The ratio between the unfolded covariance and spectra defines C in Eq. (2.6). The final result of this analysis is shown in Fig. 2.9, where each point in the cube represents the correlations between neutrons and γ rays of specified energy making a defined angle between one another.

While the cube shown in Fig. 2.9 contains all the information about the event-by-event correlations we can obtain from this experiment, it is certainly not the best way to visualize the result. In the following sections we will integrate, project, and analyze portions of this cube to better understand the properties of n-γ correlations.

2.2.2 Integrated correlations

We begin the analysis of the n-γ correlations by considering the simplest observable, the integrated correlations across all energies and angles. We note that the integration is performed across the energy acceptance region and may thus change if an improved acceptance region is chosen. The integrated correlations for the Chi-Nu experiment we have analyzed are

$$C = -0.016 \pm 0.003 \ . \tag{2.7}$$

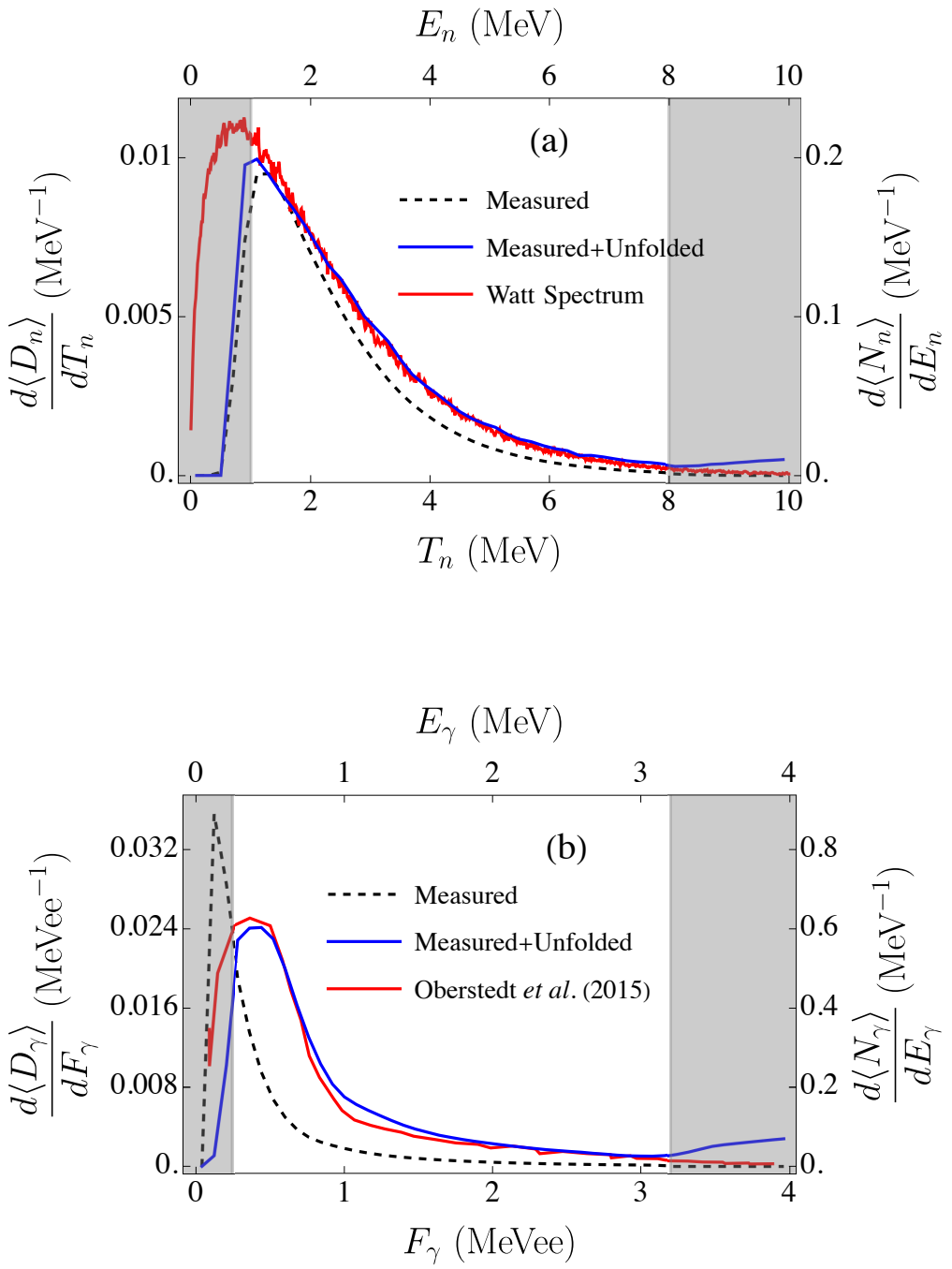

Figure 2.8: Measured and unfolded neutron (a) and γ-ray (b) spectra, compared to the reference spectra. The energy acceptance and rejection are determined from the agreement between unfolded and reference spectra.

meaning that, on average, we expect to observe 2% fewer γ rays for each observed neutron, and *vice versa*. This result agrees qualitatively well with past experimental determinations of event-by-event n-γ correlations, after the corrections outlined in Ref. [22] are applied to

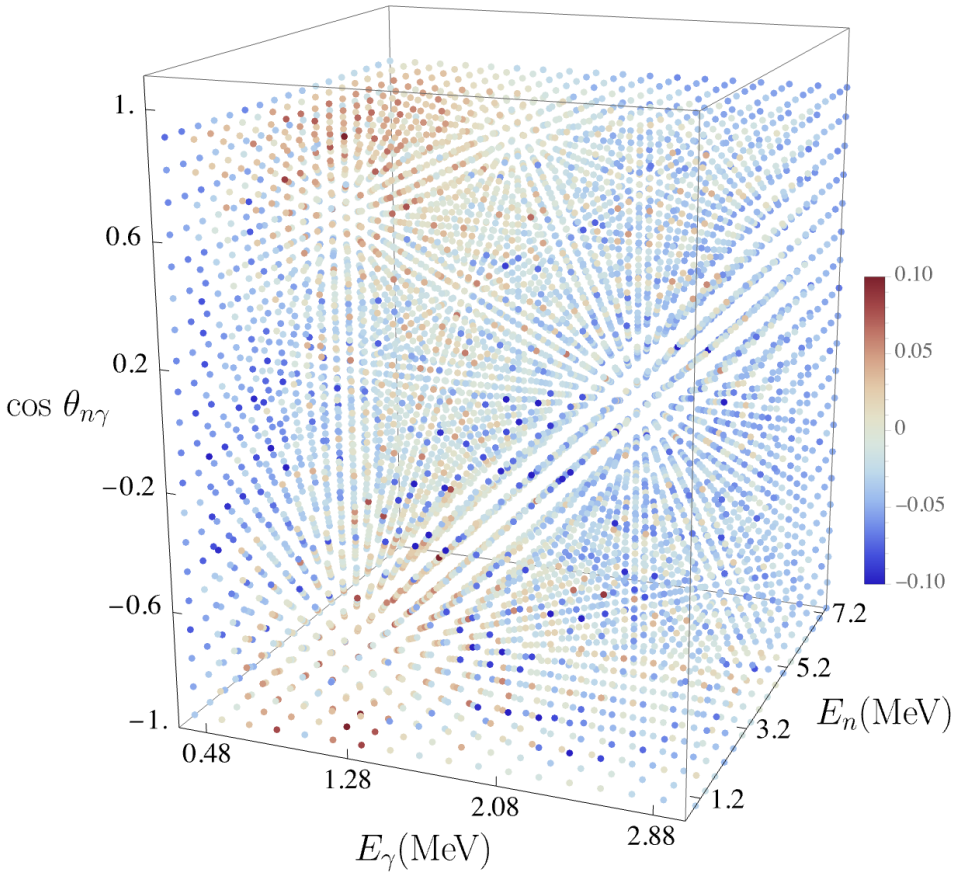

Figure 2.9: Result of the event-by-event n-γ correlations analysis presented as a cube. Each point in the cube represents the level of the correlations C between neutrons and γ rays at the specified neutron, γ-ray energy and angle between emissions.

them.

The only other independent experiments present in the literature are those by Glässel and Schmid-Fabian *et al.* [14, 25], and Bleuel *et al.* [26]. None of these publications determined C directly. Instead, Bleuel *et al.* determined the regression slope of γ-ray multiplicity on neutron multiplicity, while Schmid-Fabian determined the regression of neutron multiplicity on γ-ray multiplicity. In either case, the quantity C corresponding to these regression slopes can be determined using known values of mean and variances of neutron and γ ray multiplicities. We summarize past experimental determinations in Table 2.1. The procedure of determining C from the regression slopes adds an uncertainty to the results, which is reflected in the uncertainties given in Table 2.1.

Table 2.1: Comparison of the correlations determined by the experimental determinations of an event-by-event multiplicity correlation found in the literature, after the corrections outlined in Ref. [22] have been applied.

Experiment	$C(N_n, N_\gamma)$
Glässel *et al.* [25] (1989)	-0.023 ± 0.003
Bleuel *et al.* [26] (2010)	-0.022 ± 0.003
This work (2018-2022)	-0.016 ± 0.003

The experiment of Glässel *et al.* was performed using the Darmstadt-Heidelberg Crystal Ball [27], an array of 162 NaI(Tl) scintillators capable of distinguishing neutrons and γ rays based on their ToF. The experiment by Bleuel *et al.* employed the LiBerACE [28] detector array, composed of clover HPGe detectors. Both our determination and that of Glässel *et al.* are direct determinations, whereby event-by-event measurements of both neutron and γ-ray multiplicities are performed. The difference between the two experiments is the vastly superior efficiency of the Crystal Ball, $\epsilon_n \approx 60$ % and $\epsilon_\gamma \approx 98$ %, in contrast with the significantly better timing response of the Chi-Nu detectors. On the other hand Bleuel *et al.* measured the event-by-event multiplicity indirectly by comparing the mean γ-ray multiplicity distribution for fission events where known multiplicities of neutrons were emitted, as determined by γ-ray spectroscopy and mass balance.

The agreement between these three different independent determinations of the event-by-event n-γ correlations is reassuring, and gives us confidence regarding the results from the Chi-Nu array. The small disagreement between our estimates and the other two experiments can be explained in terms of the threshold. Glässel *et al.* used a threshold of 150 keV, Bleuel used a threshold of 100 keV, both significantly lower than our threshold of 240 keV. The threshold of the Chi-Nu system could not be pushed to these lower energies due to particle discrimination and energy resolution degradation. Similar considerations on the neutron spectrum also apply. This comparison indicates that low energy γ rays and neutrons are a source of negative correlations that are not probed in the Chi-Nu experiment.

2.2.3 Energy-angle dependence

Another useful perspective we can take in analyzing the data is to separate the dependence on energy from the dependence on the angle of emission. For this purpose, we express the correlations for fixed neutron and γ-ray energies using Legendre polynomials. We determined that the dominant terms in the Legendre-polynomial expansion are the 0^{th} and 2^{nd} order terms, with other terms, while not completely negligible, only add a small correction. Thus, we express the correlations as

$$C_{E_n E_\gamma \theta_{n\gamma}} = A_0(E_n, E_\gamma) + A_2(E_n, E_\gamma) P_2(\cos\,\theta_{n\gamma}) \ . \tag{2.8}$$

where both A_0 and A_2 depend only on the particle energies and the angular dependence is fully encoded in the second-order Legendre term, P_2. For this reason, we refer to A_2 as the *angular correlation* coefficient. The 2-D surface of these coefficients is shown in Fig. 2.10. The procedure we use to determine the Legendre-polynomial coefficients is not fitting, but rather an expansion of the data by numerical integration. This means that the results are not affected by the choice of function in Eq. (2.8). In fact, we can retain other coefficients without affecting the value of the dominant ones shown in the equation.

The statistical uncertainties for both A_0 and A_2 are shown in Fig. 2.10 (b) and (d), respectively. The uncertainties are larger for the higher energies, where fewer particles are measured. However, the uncertainties are several times smaller than the magnitude of the Legendre coefficients in the regions of enhancement that we discuss below. The discrete sampling of points in the angular space can introduce a systematic bias of up to 0.01 in A_2. These effects are corrected for using simulated angular attenuation coefficients.

2.2.3.1 Energy dependence

The coefficient A_0 has a simple physical interpretation: it represents the magnitude of the n-γ covariance averaged over all emission angles. The result in Fig. 2.10 (a) shows structure developing in the regions $E_\gamma \approx 0.7$ and ≈ 1.2 MeV. The development of this enhancement

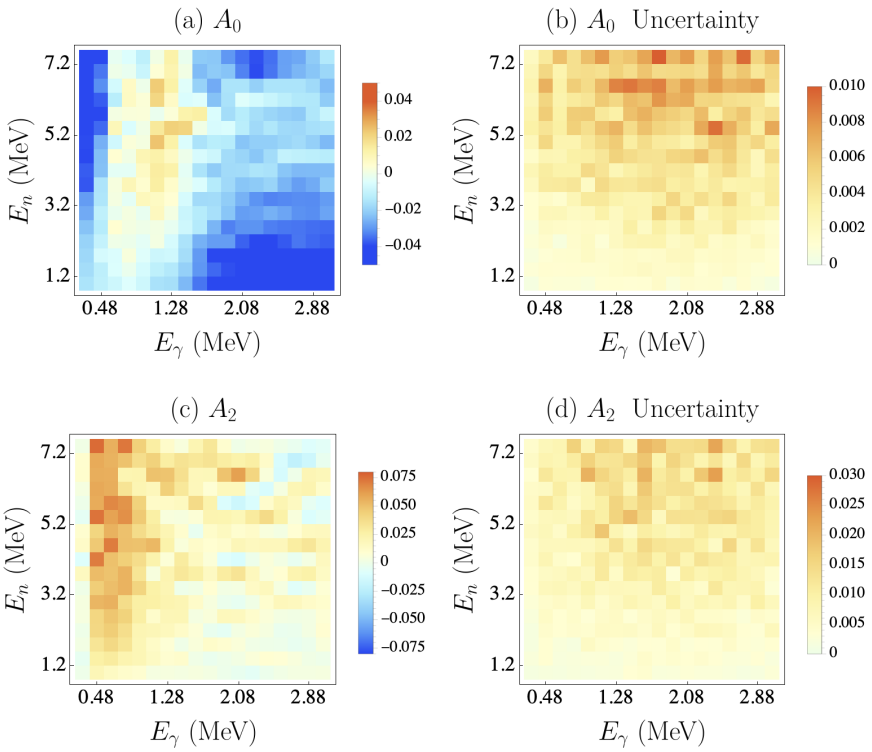

Figure 2.10: Legendre polynomials coefficients of $C_{E_n E_\gamma, \theta_{n\gamma}}$, see Eq. (2.8). The overall magnitude of the correlations is expressed in A_0, while the angular dependence is expressed in A_2.

structure is even clearer when we present slices of fixed E_n of the surface A_0, as shown in Fig. 2.11. We note that while the enhancement at $E_\gamma \approx 0.7$ MeV remains relatively unchanged in magnitude with increasing E_n, the enhancement at 1.2 MeV grows larger with neutron energy.

Unfortunately, no experimental data exist to describe any level of differentiation of C. Instead, the experimental results are compared to model calculations `CGMF` [29, 30], `FIFRELIN` [31, 32, 33], and `FREYA` [34, 35]. The released versions of `CGMF` and `FREYA` are used here. `FIFRELIN` simulations are performed using both an energy independent (constant) and an energy-dependent (E^*-dependent) model of the angular momentum generation in the fragments [36]. For consistency with the data, a Gaussian smoothing informed by the energy resolution of the system is applied to all model calculations.

Apart from the enhanced correlations at 0.7 and 1.2 MeV, there are other important

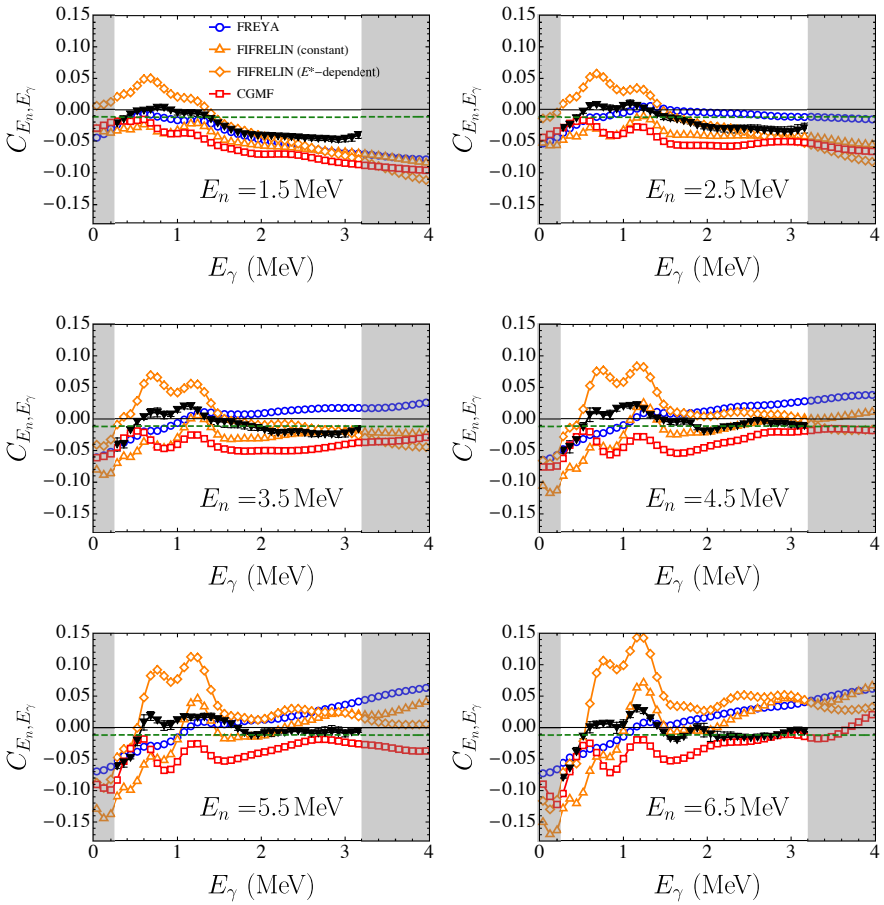

Figure 2.11: Slices of fixed E_n for the A_0 coefficient, showing the dependence of the n-γ correlations on E_γ and the development of enhanced structure. The black triangles are the experimental points, while the green dashed line is the value of the integrated correlations, Eq. (2.7). The data is compared to model calculations.

features of C when differentiating with respect to E_γ, specifically its behavior at low and high E_γ. In both of these regions the correlations are strong and negative, with correlations at low E_γ becoming more negative with increasing E_n. The correlations at high E_γ are approximately constant - albeit with a small linear dependence on E_γ - between $2 < E_\gamma < 3$ MeV, and negative for low E_n. The magnitude of these correlations tends to become more positive with increasing E_n. As expected from the comparison with previous experiments, we see that the correlations tend to become more negative at the lowest neutron and γ-ray energies.

Lastly, we turn our attention to the correlations integrated over both angles and neutron

energies, shown in Fig. 2.12. It is in this plot that the appearance and features of the enhanced correlations are most visible. The results are also compared to model calculations and to the integrated value, see Eq. (2.7).

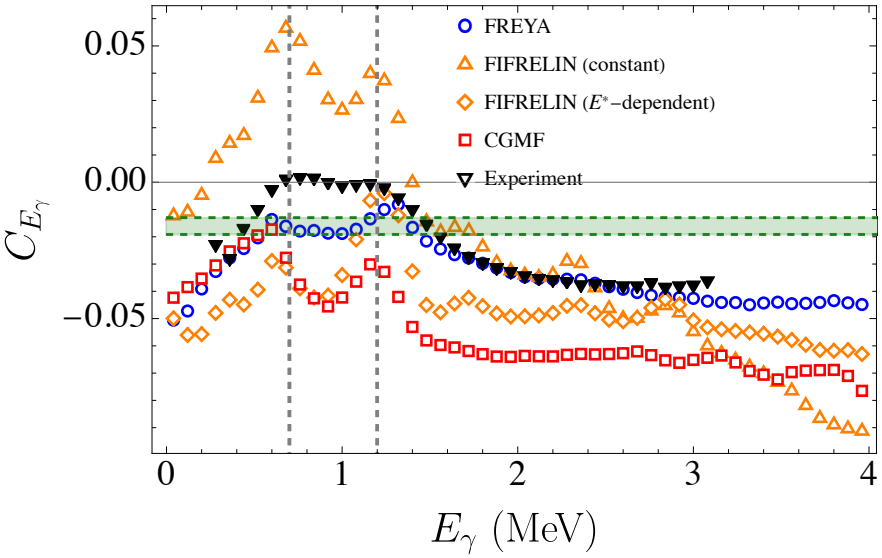

Figure 2.12: The dependence of the event-by-event n-γ correlations is determined by integrating the triply differentiated correlations with respect to both neutron energy and angle. We observe negative correlations throughout, with an enhancement at intermediate energies. The appearance of the enhancement is understood via the model calculations in terms of two unresolved structures at 0.7 and 1.2 MeV, highlighted by two vertical dashed lines. The dashed horizontal line and the shaded area represent the correlations integrated over all energies and angles, with uncertainties. Model calculations are also shown on the same figure.

2.2.3.2 Angular dependence

The coefficient of the second Legendre polynomial, A_2, in Fig. 2.10 (c) shows the dependence of the correlations on the emission angle between neutrons and γ rays. Positive A_2 indicates γ rays are aligned predominantly along the direction of neutron emission, both parallel and anti-parallel, while negative A_2 indicates γ rays are aligned perpendicular to the neutron emission. Because the multiplicities are non-negative, we have $C + 1 > 0$, which puts a limits on the strength of the angular correlations, $A_2 > -(1 + A_0)$.

We note enhanced positive structure at $0.4 \leq E_\gamma \leq 0.8$ MeV in A_2. This enhancement

overlaps with the structure observed in A_0 at 0.7 MeV but extends to lower energies and does not extend to higher energies. Importantly, we do not observe any pronounced A_2 enhancements at $E_\gamma \approx 1.2$ MeV, as we do in A_0. Overall, we observe a trend of enhanced angular correlations with increasing neutron energies. The magnitude of the angular correlations in this region is approximately $A_2 \approx 0.07 \pm 0.01$.

At high E_γ the angular correlations are much smaller and consistent with 0 within uncertainties. Angular correlations are also weak at the lowest γ-ray energies, but caution should be used in interpreting this region as it borders the lower edge of the E_γ acceptance and the unfolding might lead to artifacts. We do not observe significant dependence on neutron energy in either the low or high E_γ region. In Fig. 2.13, we show slices of the triply differentiated C at fixed E_n and E_γ, showing how the correlations vary with respect to the angle between neutron and γ radiation. The angular correlations become more pronounced with increasing E_n. To highlight the dependence of the n-γ angular correlations on E_n, we show slices of the A_2 in Fig. 2.14.

At the time of writing, none of the popular codes for fission emission used in the previous discussion of energy dependence predict n-γ angular correlations. However, this topic is one of significant current interest, and steps are being taken to include this capability [37].

2.3 Discussion

In this section, we discuss the experimental results and offer physics-based explanation for the appearance of the observed behavior. The presence of negative n-γ integrated correlations is understood in terms of a competition between neutrons and statistical γ rays over the intrinsic fragment excitation energy. This competition is of such large magnitude that when the correlations are integrated over all particle energies and directions, the resulting correlations are negative.

Correlations between neutrons and statistical γ rays can be determined by examining the high E_γ portion of the differentiated correlations. In fact, the emission of statistical γ rays is

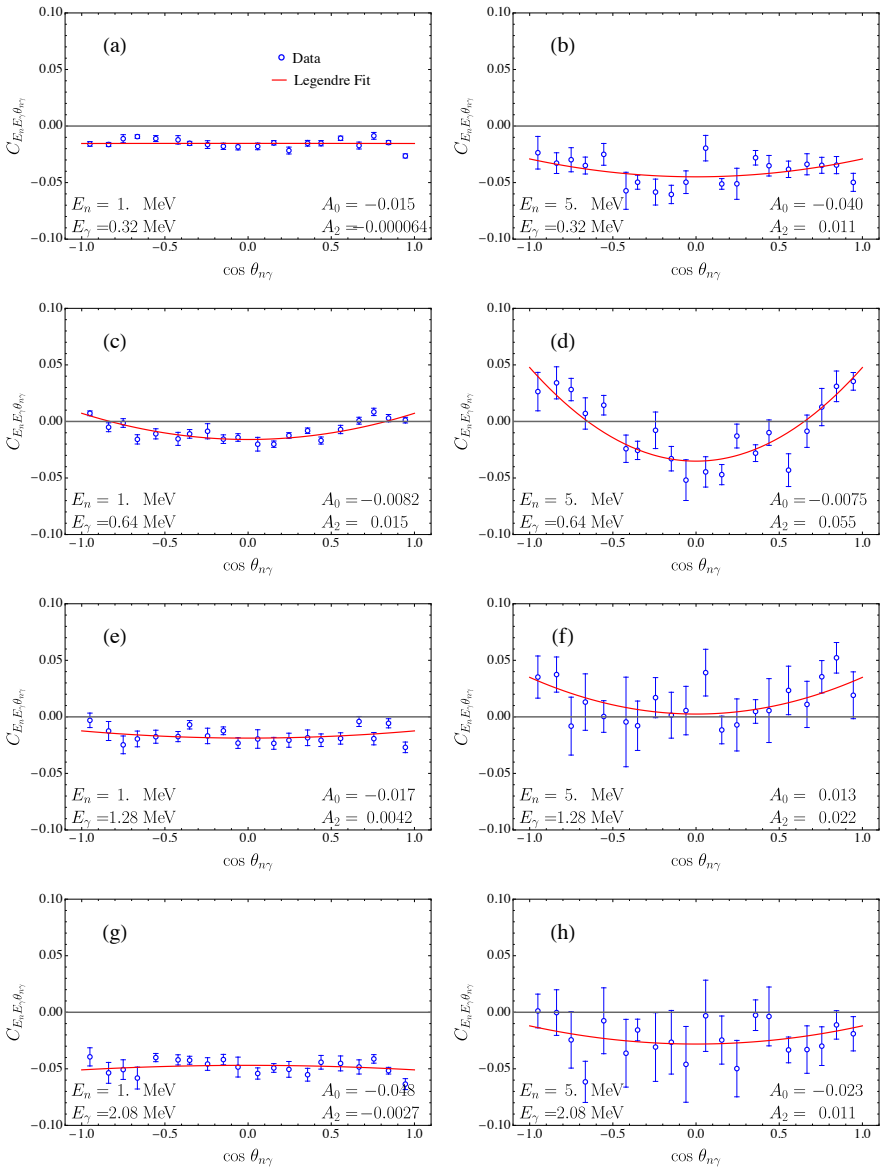

Figure 2.13: Slices of the triply-differentiated correlations C at fixed E_n and E_γ. The cures show the Legendre polynomial retaining only the 0^{th} and 2^{nd} order terms. Uncertainties on the determined A_0 and A_2 coefficients are shown in Fig. 2.10.

much more probable than collective emission at these energies. The strength of the negative n-γ correlations, presented in Fig. 2.12, as well as the dependence of these correlations on E_n, shown in Fig. 2.11, is quite different than what is obtained in the model calculations. In fact, the observed correlations are consistent with fragment excitation energies being uncorrelated relative to one another, as suggested by past experiments [38, 39]. Furthermore, the n-γ angular distributions for statistical γ rays appears to be almost isotropic, indicating that

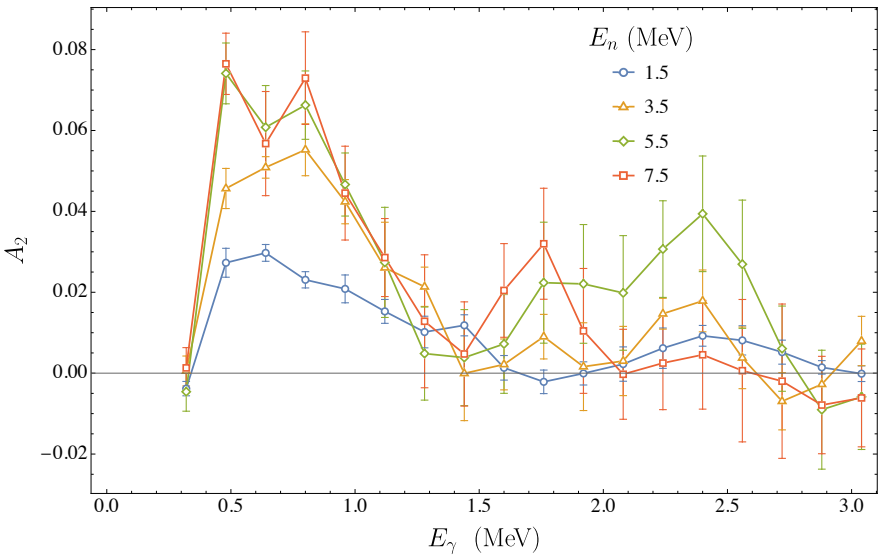

Figure 2.14: Slices of the angular correlation coefficent A_2 of $C(N_n, N_\gamma)$, see Eq. (2.8). The angular distribution becomes more anisotropic with increasing E_n.

statistical γ rays do not carry a significant amount of angular momentum.

The appearance of two concentrated n-γ enhancements at $E_\gamma \approx 0.7$ and 1.2 MeV, shown in Fig. 2.11, Fig. 2.10 (a), and most clearly in Fig. 2.12, is a result of the similar energies of band transitions in many fission fragments. Stretched quadrupole, $E2$, band transitions, *i.e.*, γ-ray transition where the fragment changes state within a rotational band and changes its angular momentum by $2\hbar$, can be recognized by their energy signature, determined from the rotational energy states of fission fragments and their angular distributions. Typical light and heavy fission fragments have $E2$ transitions with energies in the range 0.5 to 0.9 MeV, whereas fragments produced in symmetric fission, with masses closer to the shell closure of ^{132}Sn, have much larger energies, 1-1.5 MeV [23]. Nucleon shells are closed when nucleons populate all the available states, and when major shells are closed the nuclei tend to be more spherical and stable. Thus, from this energy argument alone, there is an indication that an increase in neutron multiplicity correlates positively to stretched $E2$ γ rays along rotational bands. This observation is consistent with positive correlations between E^* and J

The proposition that stretched $E2$ γ-ray emission positively correlates with neutron emission is further strengthened by the presence of significant n-γ angular correlations. Stretched

$E2$ γ rays tend to be emitted in a plane perpendicular to the direction of the fragment angular momentum. Because the angular momentum is on average polarized in a direction perpendicular to the fission axis, see Refs. [4, 5, 6], the $E2$ γ-rays appear to be emitted preferentially parallel and anti-parallel to the fission axis, and thus with kinematically-boosted neutrons. The n-γ angular correlations shown in Fig. 2.10 and Fig. 2.14, indicate that the γ rays that correlate positively to neutron emission are of stretched $E2$ character. The n-γ angular correlations in the $E_\gamma \approx 1.2$ MeV enhancement are small, indicating that fragments created in symmetric fission are not as polarized as typical fission fragments.

Fragments are assumed to emit stretched $E2$ γ rays to dissipate the largest share of their angular momenta, while neutron are emitted to dissipate the majority of their excitation energies. The existence of positive correlations between stretched $E2$ transitions and neutrons is consistent with the existence of positive E^*-J correlations in fission, but it does not provide a strong enough argument. The experiments presented in the next two chapters will provide evidence for this claim.

Comparison with model calculations provides insight into the E^*-J correlations, and their effects on the emission correlations. Specifically, we draw attention to the large n-γ correlation enhancements in the `FIFRELIN` calculations. The appearance of the enhancement at 0.7 MeV is almost entirely due to E^*-J correlations. Thus, we conclude that the observed enhancements in the event-by-event correlations are consistent with positive E^*-J correlations.

CHAPTER III

Neutron-Induced Correlations

3.1 Introduction

In this chapter we will take a closer look at how γ-ray emission correlates with external sources of energy. This study allows us to better investigate E^*-J correlations in fission by exercising control over the excitation energy of the system and subsequently studying the emission of γ rays. Specifically, we will show new results on the neutron-induced fission of ^{239}Pu with incident neutron energies in the range 2-40 MeV. We focus on new results in the already rich topic of neutron-induced fission, the γ-ray multiplicity and spectra and how these features are affected by changes in incident neutron energy. The motivation is the following: γ rays carry information about the fragment angular momentum, while the incident neutron energy provides a way to probe the excitation energy of the system; by studying γ ray correlations with incident neutron energy, we also probe E^*-J correlations.

The results shown in this chapter are the first direct experimental determination of γ-ray multiplicities in the fast neutron-induced fission of ^{239}Pu. We analyzed these data to determine the correlations between angular momentum and excitation energy. Our findings are in good agreement with the results from Chapter II. Specifically, we have once again determined the existence of positive E^*-J correlations. Furthermore, because the incident neutron energy is now used as a control variable, we have determined that these correlations

appear to be roughly linear, however over a range too narrow to rule out nonlinearity.

Notably absent from this chapter are correlations between neutron emission and incident neutron energy. There are several reasons for this deliberate omission. In the first place, the study of neutron emission does not provide, in this experiment, any new insights into the E^*-J correlations that are not already provided by the study of the incident neutron energy. Next, from a practical perspective, the experiment is not built to study neutron multiplicities and the amount of work required to extract the emitted multiplicities would have warranted its own chapter, with results of lower quality than those obtained in dedicated neutron multiplicity experiments. Lastly, neutron emission as a function of incident energy is one of the *benchmark* quantities in nuclear fission for both peaceful and military applications, and any data we could provide from this experiment would fall far short of being a valuable addition to an already rich literature.

3.1.1 Outline

In Section 3.2, we briefly present the experimental setup and the elements of the system response that are important for this experiment. The Chi-Nu array at LANSCE, which is already employed in Chapter II, is used for this experiment as well. The fission trigger and the incident neutron beam are new to this experiment, and their characteristics are presented in this section and mathematically analyzed in Section 3.3. In this chapter we also discuss the contamination of the fission signal and the background analysis, which have a far more important role in these results than in the other results of this dissertation.

The results of our experiment, in the form of energy-differentiated γ-ray multiplicity conditioned on incident neutron energy, are presented in Section 3.4. In this Section we also compare our experiment to past literature and model calculations. As stated, this experiment is the first of its kind for this reaction. Therefore we compare our measurement to similar reactions which are expected to yield somewhat similar results. We also determine the correlations of γ rays with the pre-fission excitation energy E^x, which results in roughly

linear correlations. Section 3.5 employs the results of Section 3.4 to understand the physics of E^*-J correlations.

The experiment analyzed in this chapter is performed by the Chi-Nu group at Los Alamos National Laboratory. The data are provided to us by Keegan Kelly, John O'Donnell, and Matthew Devlin. Nathan Giha, a graduate student I mentored, is responsible for much of the analysis in the final steps of this chapter. Isabel Hernandez coauthored a large fraction of the scripts used for this experiment. Some of the results of this chapter appear in Ref. [40].

3.2 Experimental setup

The detection system used in this experiment, the Chi-Nu array, is the same employed in Chapter II. The main difference in this experiment is the presence of an incident particle beam and the use of PPAC detectors as the fission trigger. Furthermore, all 54 detectors of the Chi-Nu array are operational in this measurement. The description of the experimental system is based on the description provided by Kelly *et al.* [16], and the reader is referred to that journal publication for detailed information.

3.2.1 Beam

The LANSCE linear accelerator is used to produce neutrons for this experiment. Protons are accelerated in the linear accelerator to an energy of 800 MeV. These protons are then delivered to a tungsten converter at the weapons neutron research (WNR) facility over a time interval of 150 ps. This short interval of proton delivery to the WNR converter is known as a beam *micropulse*. Micropulses are separated from one another by 1.8 μs, to allow measurements to occur in between micropulses. Nominally, 347 micropulses are delivered to WNR in a *macropulse*. The separation between macropulses is much larger, with an approximate frequency of 100 macropulses per second.

The incident protons from the linear accelerator hit the WNR tungsten converter and undergo *spallation*. The violent process of spallation generates neutrons, photons, and neu-

trinos as well as charged particles such as protons and mesons. Charged particles are removed from the outgoing beam by shielding. The products of the spallation reaction travel a flight path of approximately 21.5 m and reach the ^{239}Pu target at the center of Chi-Nu. An electromagnetic signal is collected shortly before the proton is incident on the spallation converter, giving us a time for the generation of neutrons that is used for neutron ToF. The simulated spectrum of neutrons from the spallation target, calculated by Kelly *et al.* [16], is shown in Fig. 3.1.

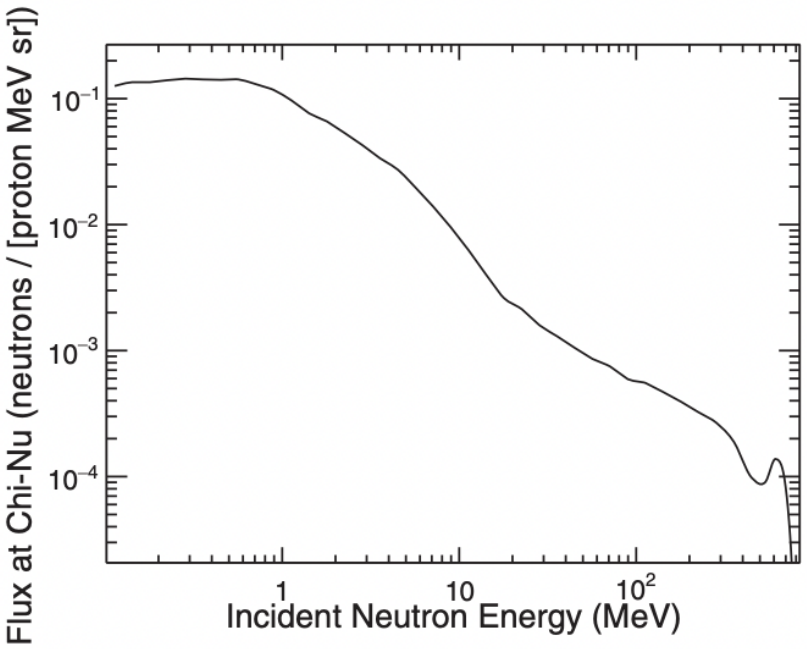

Figure 3.1: The simulated spectrum of spallation neutrons generated by the LANSCE proton linear accelerator incident on the WNR tungsten converter. As pointed out in Ref. [16], some attenuation along the 21.5 m neutron flight path is not captured in the simulation and it is expected that the lower energy portion of the neutron spectrum will be suppressed in experiment.

Spallation photons, travelling at the speed of light, reach the fission target after approximately 72 ns. The spallation photons interact with the fission target and with the gas of the *parallel-plate avalanche counter* (PPAC) detector, described in the next section, giving rise to a prompt increase in the measured PPAC count rate. This feature, shown as the fast rising edge in Fig. 3.2, is used to adjust the timing delays between the PPAC channel

time and the spallation signal. Spallation neutrons reach the PPAC and the fission target at different times, depending on their energy. Several incident neutron energies are labeled on the beam-PPAC plot in Fig. 3.2.

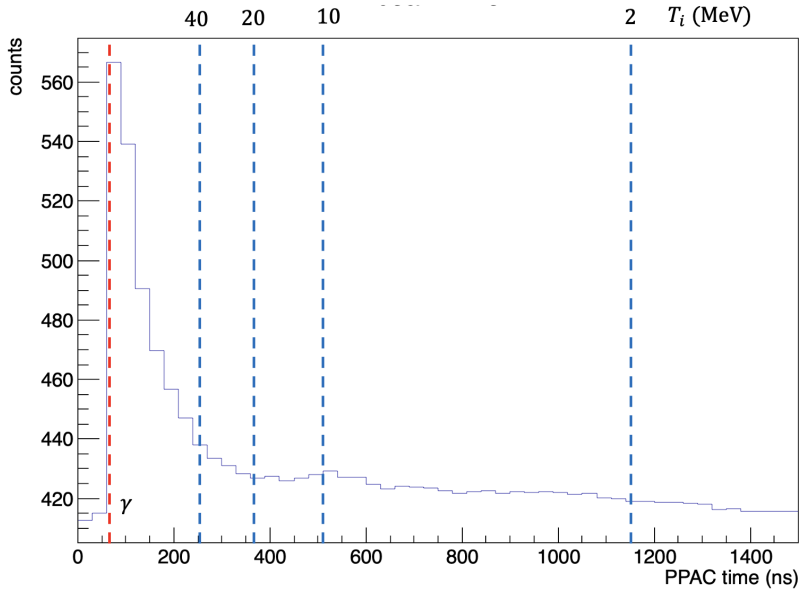

Figure 3.2: ToF distribution between the PPAC detector and the spallation signal. The fast γ-rays reach the detector immediately, giving rise to a prompt increase in PPAC counts. Neutrons, with the broad energy spectrum shown in Fig. 3.1, reach the detector at different times depending on their energy. The count rate before the arrival of the photons indicates the presence of count rates due to a constant α-decay rate and counts due to the preceding micropulse. Vertical dashed lines correspond to the time of arrival of the indicated neutron energies.

3.2.2 PPAC detector

The fission trigger in this experiment is provided by the PPAC detector shown in Fig. 3.3 (see Ref. [41]). The PPAC consists of 10 volumes, each containing a ^{239}Pu deposit, and each possessing an independent readout channel. The plutonium targets, approximately 10 mg for each target, are deposited on 5 μm titanium backings, resulting in a target thickness of approximately 400 μg cm^{-2}. Fission fragments and α particles ionize the 4.2 torr isobutane gas that fills the PPAC. The ionization track is amplified by an applied potential difference of 375 V between the aluminum plates. The large electric field generated by this poten-

tial difference causes an electron avalanche to form in the volume. The different identical segments of the PPAC detector are separated by platinum foils to isolate their signals.

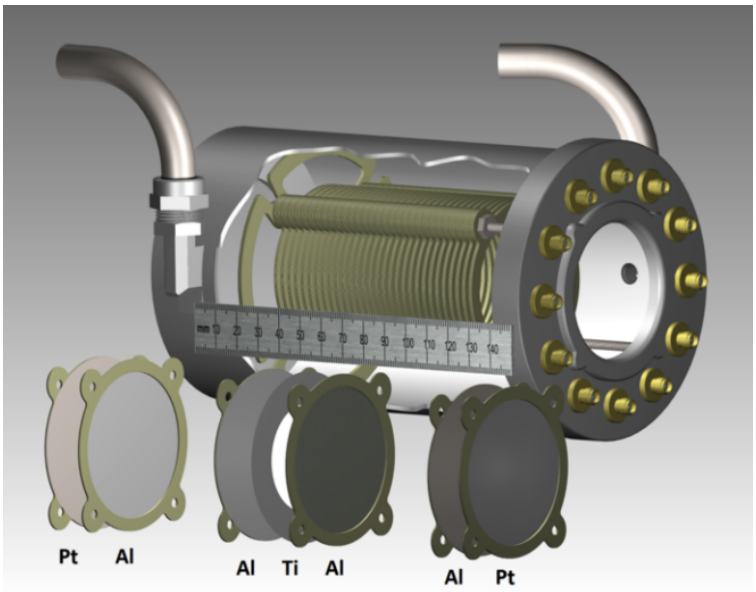

Figure 3.3: Diagram of the PPAC detector used in this experiment. The construction and material used in each separate volume are shown. The chamber is filled with isobutane gas, which is ionized by fission fragments and other charged particles. An applied voltage cause the ionization track to cause an avalanche and a very fast signal.

The advantage of the PPAC detector is its excellent timing resolution, < 1.0 ns FWHM, comparable to the time resolution of the fast scintillation detectors. Because of the low gas pressure, fragments and α particles deposit only a small fraction of their energy in the gas volume. The energy resolution suffers from this design, and the separation between α particles and fission fragments is imperfect. The spectrum of PPAC-detected events is shown in Fig. 3.4. We estimated the background α activity by measuring the PPAC count rate between macropulses. These count rates are then scaled by the measurement window and subtracted from the spectra measured in coincidence with the beam. The subtracted PPAC spectrum, corresponding to what we call fission events, is also shown in Fig. 3.4. A Gaussian distribution has been fit to the fission events, as shown on the figure, but is not used in the analysis; rather, the actual subtracted spectrum is used.

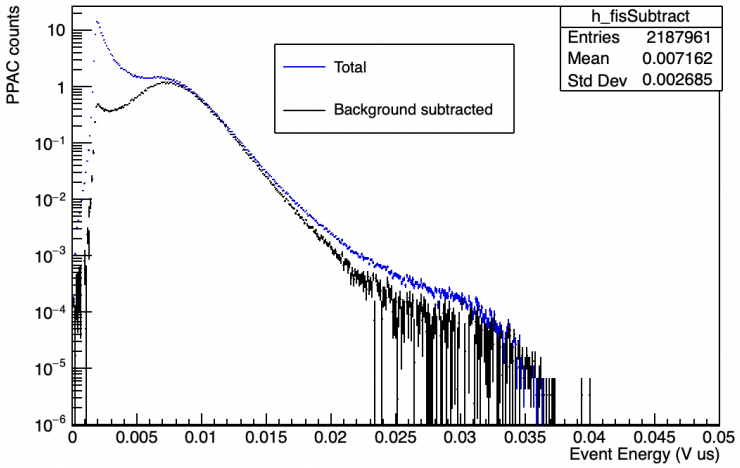

Figure 3.4: Spectrum of events from the PPAC. The background α-decay count rate, estimated from count rates in between beam pulses, is subtracted from the data to estimate the actual fission count rate.

3.3 Experimental response

The response of the Chi-Nu detectors has been extensively explored in Chapter II. The focus of this section is the response of the PPAC and the beam to accurately measure fission events and associate them with an incident neutron energy.

3.3.1 Beam energy

The energy of the incident neutron beam, E_i, is estimated from the time of flight of neutrons between the spallation converter and the PPAC plate. The time resolutions of the PPAC and beam system, estimated at 1 ns, results in $\sigma(E_i)$ of 0.004, 0.04, 0.12, 0.34, and 1.0 MeV at $\langle E_i \rangle = 2$, 10, 20, 40, and 80 MeV. The time resolution alone does not represent an important bias, but it sets a limit on the granularity with which incident neutron energy is differentiated. Because of this time resolution, we use bins in E_i of width 1 MeV, and limit our analysis to E_i below 40 MeV, avoiding any significant misclassification of incident neutron energies.

The main source of bias in the determination of E_i is the *wraparound* effect. The slowest neutrons from a spallation event, $E_i < 1$ MeV, reach the fission target at the same time as the

fast neutrons from the next spallation event. An illustration of the wraparound effect between micropulses, taken from Ref. [16], is shown in Fig. 3.5. The energies of neutrons decreases very slowly over the entire beam coincidence window, such that wraparound neutrons with $E_i = 0.6$ and 0.3 MeV arrive simultaneously with $E_i = 40$ and $E_i = 2$ MeV neutrons from the following event. We approximate all wraparound fission events to be caused by neutrons with incident energy $e_w = 0.5$ MeV, without introducing a significant source of error. In fact, as we shall determine, the γ ray multiplicities vary slowly with incident beam energy and the error in assuming 0.5 MeV compared to using the exact wraparound energy is negligible.

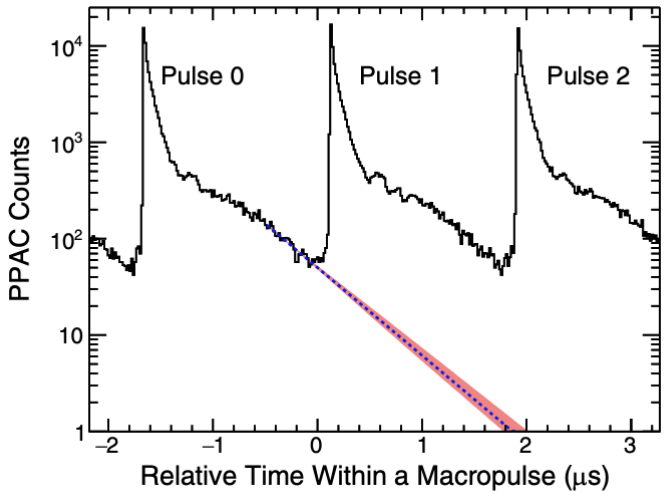

Figure 3.5: Low energy neutrons from one micropulse can reach the fission target simultaneously with faster neutrons from the next micropulse. This effect is called wraparound, and it can cause a response bias for the determination of the incident neutron energies.

We estimate the wraparound probability w using the simulated spectrum shown in Fig. 3.1, which is transformed to a flux rate, *i.e.* incident neutrons per unit time, on the fission target. It is pointed out in the figure label that the low-energy portion of the spectrum is over-estimated in the simulation, as additional shielding takes place in the neutron flight path. The wraparound probability estimated in such manner is shown in Fig. 3.6.

Although we do not measure the γ-ray multiplicity at e_w, we can infer the γ-ray properties by extrapolation. As we will confirm in our analysis, for energies $E_i \lesssim 6$ MeV the regression

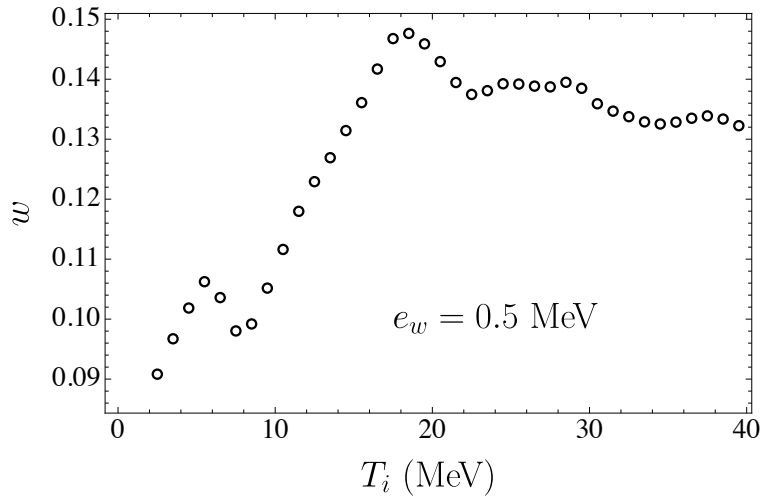

Figure 3.6: The wraparound probability w as a function of the incident neutron energy, as assigned by ToF. The energy of the wraparound neutrons varies slowly over the coincidence window, and it is taken to be 0.5 MeV. The n-γ observables of fission induced by wraparound neutrons are deduced by extrapolation.

of γ ray multiplicity on E_i is linear, warranting the extrapolation. The unfolding of the wraparound bias is performed by inverting the simulated wraparound response and applying it to experimental data with the addition of the extrapolated multiplicity of γ rays at the wraparound energy.

3.3.2 Contamination

In Section 3.2, we saw how the background α decay can be subtracted from the overall PPAC spectrum to obtain the spectra of fission events. This correction cannot be performed event-by-event, but is used to obtain a probability that a recorded event with measured incident energy T_i and a measured integrated-voltage signal F_i in the PPAC is a valid fission event.

We have determined that the PPAC spectrum depends very weakly on the incident neutron energy. Thus, we find that the probability that a given PPAC event is a fission is separable into the product of two components, depending respectively on F_i and T_i. In the first place, we have determined the ratio of fission events to the total number of PPAC

events as a function of F_i, by taking the ratio of the subtracted and unsubtracted PPAC spectrum, see Fig. 3.1. This conditional probability, which we call the *fission fraction*, is shown in Fig. 3.7 (a). This procedure is repeated for all incident energies T_i. As stated, the subtracted PPAC spectrum is not observed to change significantly with T_i, so the same threshold of 0.005 V μs is used for all of them. The probability $\mathbb{P}(G|T_i)$ is determined by fixing G and integrating the fission fraction over all measured T_i. The ratio of fission event as a function of T_i is shown in Fig. 3.7(b).

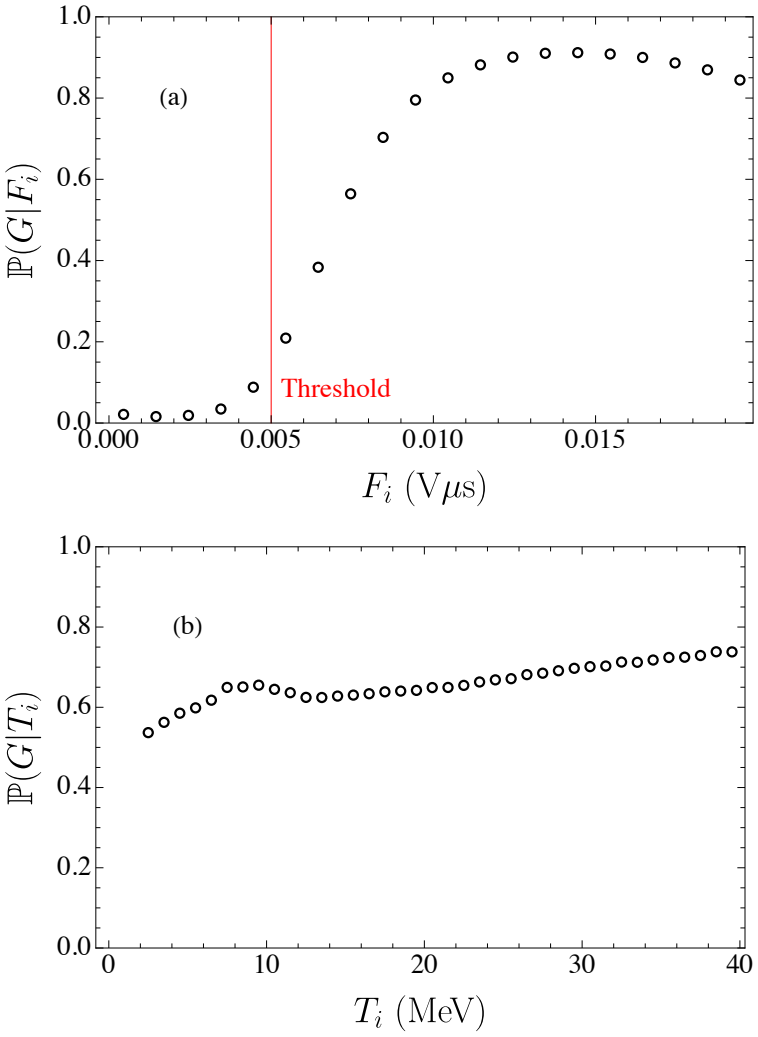

Figure 3.7: The estimated fraction of fission events to the overall number of events as a function of the PPAC pulse height F_i and the measured incident neutron energy T_i.

The behavior of the fission fraction as a function of F_i is intuitively explained. PPAC

events induced by α decays tend to dominate at lower energies, but their effect is quickly reduced by increasing the energy threshold. At the highest F_i, both fission and α decay are unlikely, and electronic noise and other sources of measurement error become likely. This explains the onset of a small decrease in the fission fraction at high F_i. At the lowest F_i, we see a small increase, cause by the imperfection of the background subtraction technique. In fact, a small portion of the PPAC background events are beam-correlated, and their effects are observed at the lowest F_i. These effects are eliminated using the indicated F_i threshold.

The behavior of the fission fraction as a function of T_i is determined uniquely by the fission reaction rate and the collection window for each T_i bin. Even in the absence of cross section changes, we expect the fission fraction to increase with T_i. In fact, the collection window of higher T_i, using uniformly spaced T_i bins, decreases and the number of α decays, which are expected to have a uniform time distribution, scale down accordingly. The structure around $8 - 10$ MeV is instead most likely caused by the local changes in the cross section of the neutron-induced reaction.

3.3.3 Background

We recognize three types of background in this experiment: an α-decay-correlated background, A_γ, due to the emission of γ rays following α-decay; a beam-correlated background, B_γ, composed of particles from the beam that are measured because the α-decay event opens a collection window during which these particles are measured; and a background uncorrelated with both α decays and beam, for example caused by other sources in the room, cosmic rays, *etc.* We have found this last background source to be vanishingly small.

We characterize the background multiplicity A_γ by opening, in post-processing, a γ ray coincidence window at times between macropulses, thus virtually eliminating beam-correlated background. The beam-correlated background is instead determined by introducing *random triggers* in the data. These random triggers are then used as fictitious fission events for coincidence purposes. The timing of the random trigger event is used to assign to it a fictitious

incident energy T_i. On the other hand, the fictitious pulse height is chosen to be a constant above the acceptance threshold, $F_i = 0.01$ V μs, since no correlations between T_i and F_i have been observed in the data. Neutrons and γ rays collected in coincidence with the random triggers are then equivalent to the background multiplicity B_γ.

The random-trigger method of determining background is more accurate than the *time-reversed* method employed in Chapter II. For a time-independent background, the two methods are identical. The presence of the beam, with its characteristic time-dependence shown in Fig. 3.2, breaks the symmetry.

3.3.4 Energy acceptance

The last step in the analysis of the detection system is the analysis of the response of the scintillation detector to the γ radiation. A comparison of the measured, unfolded, and ENDF-evaluated spectra [42], is shown in Fig. 3.8. Because we could not find spectra of particles for non-thermal neutrons, we unfolded our data at the lowest incident energy bin, E_i = 2-3 MeV, and compared it to the spectra from the thermal neutron-induced fission of ^{239}Pu.

The detector calibrations and gains are not controlled as carefully in this experiment as they were in the previous experiment with ^{252}Cf. Thus, the acceptance region is narrower than in Chap. II, and only γ rays of energy $0.4 < E_\gamma < 2.2$ MeV are properly reconstructed. In future work, the experiment should be repeated with optimized detector parameters. This acceptance region corresponds to a coverage of $\approx 60\%$ of the γ-ray spectrum, as deduced from the evaluated spectrum of ^{239}Pu($n_{\rm th}$,f).

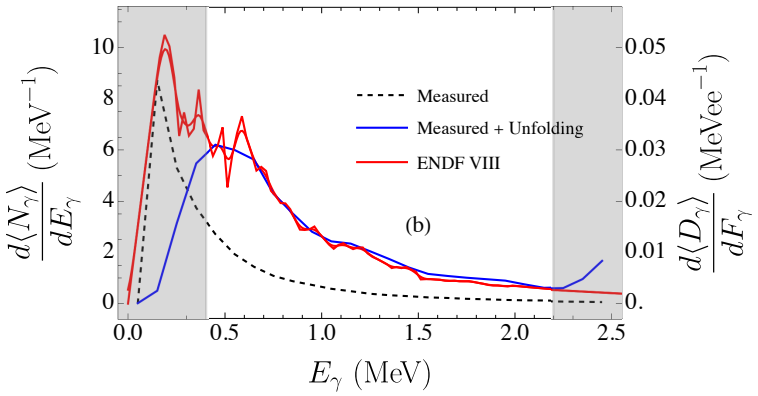

Figure 3.8: Measured γ-ray spectrum, using the right axis, compared to the unfolded spectrum, using the left axis. The unfolded spectrum is compared to the evaluated data from the ENDF evaluation [42].

3.4 Results

The main result we extract from this experiment is the energy differentiated γ-ray multiplicity conditionally differentiated on the incident neutron energy,

$$\left\langle \frac{dN_\gamma}{dE_\gamma} \middle| E_i \right\rangle \ . \tag{3.1}$$

The differentiated multiplicities are corrected for background, alpha contamination, wraparound corrections, and their spectrum is unfolded. The results are shown in Fig. 3.9.

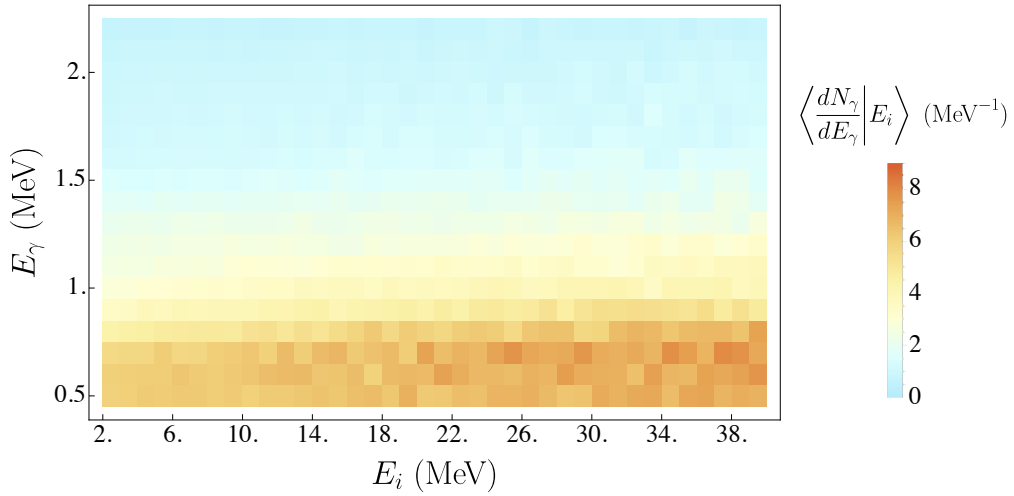

Figure 3.9: The beam-differentiated γ ray spectra.

While the data in this form contain all the information we have extracted from this experiment, its meaning is not immediately intuitive. To aid in the data visualization, we integrate the measured spectra in the acceptance region and determine the increase in the γ-ray multiplicity with increasing incident energy.

In stark contrast with the situation for neutron observables, γ-ray studies of the kind shown here have been few and far between. Perhaps the most notable study is the one performed by J. Fréhaut [43] in the early 1980s. This makes our results, shown in Fig. 3.10, all the more useful to the nuclear fission community. We have determined that the dependence of γ-ray multiplicity on E_i is linear below the second-chance fission threshold, which onsets for $E_i > 6$ MeV. Above this energy, the nucleus can evaporate a neutron and still have enough energy to proceed to fission. For even higher energies, more neutrons can be evaporated, leading to n^{th}-chance fission, indicating the emission of $n-1$ neutrons before fissioning. The process of pre-fission emission can complicate the analysis, as the fissioning nucleus has a statistically distributed excitation energy, depending on the relative probabilities of pre-fission evaporation. In the region below the onset of pre-fission emissions, we have determined that there is a linear increase of $\approx 0.085 \pm 0.010$ γ MeV^{-1}. Above the second-chance fission threshold, the dependence is nonlinear.

The error in the measurement is a combination of statistical errors and systematic errors. The largest source of systematic error is the spectrum unfolding procedure. We have created a covariance matrix associated with this unfolding procedure by varying the regularization parameter in the unfolding procedure. Other possible sources of error to be explored in future work are the errors in the fission fraction calculation, and variations in background multiplicities.

While little is known about the dependence of γ-ray multiplicity on E_i, there are a few experiments that can be compared to our results. These experiments use a threshold of 0.1 MeV, lower than the one used in this experiment. Thus, a correction factor, based on the ratio of the accepted spectrum at $E_i = 2$ MeV is applied to all measurements. There is an

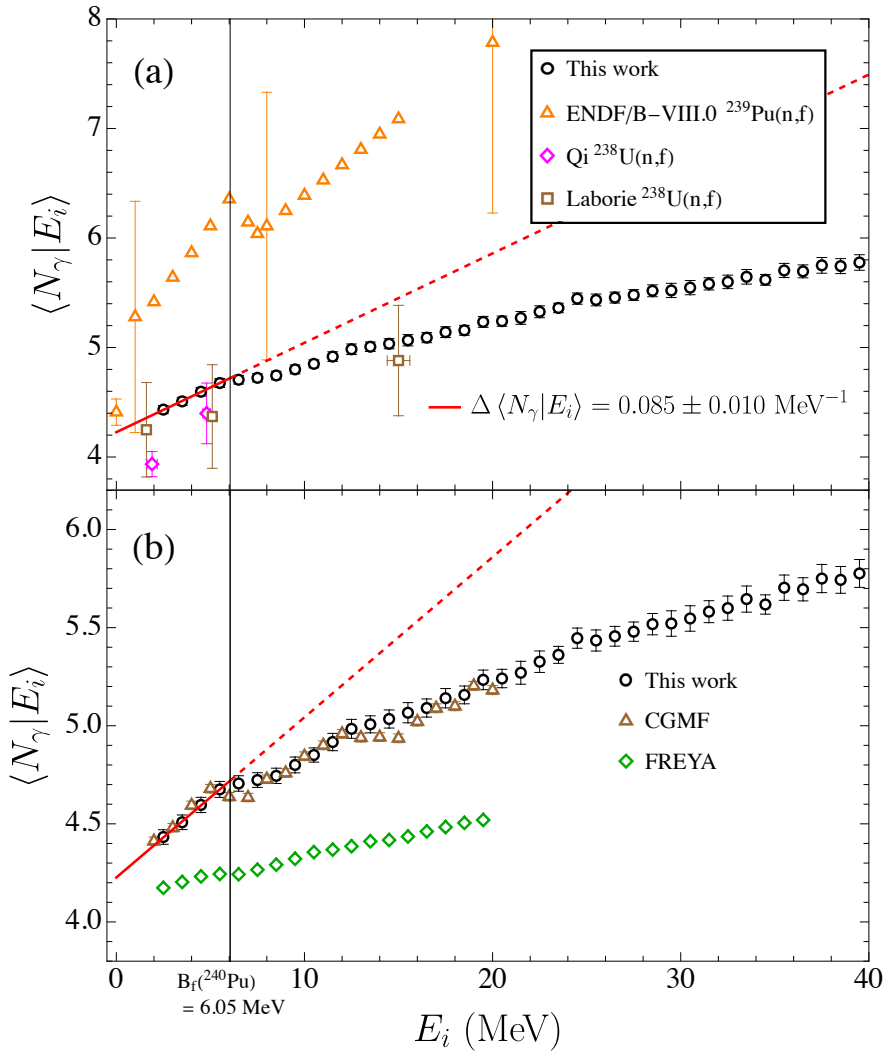

Figure 3.10: Regression of γ-ray multiplicities on incident neutron energy. We compare our experimental results with (a) other experimental data and (b) with model calculations.

existing evaluation of the γ-ray multiplicity in the most recent ENDF evaluation, [42], itself based mostly on the results by Gatera *et al.* [44]. Our results agree well with the evaluation when extrapolated to thermal energies, $E_i \approx 0$ MeV. The thermal-neutron induced fission data point is by far the most well known, and it is encouraging that our results are in good agreement. For higher E_i, the evaluation immediately jumps to much higher multiplicities. These results, which have been included in the evaluation with a 20 % error - shown only on a select number of points in the figure - could not be reproduced in our experiment.

We compare our results to two experiments that studied $\langle N_\gamma | E_i \rangle$ in the reaction ^{238}U(n,f), by Qi *et al.* [45] and Laborie *et al.* [46]. These results, which are not expected to agree exactly with ours due to the different reaction, also cannot be compared in terms of their quality. In the first place, the error bars on their measurements are an order of magnitude larger than those in this work. Second, both investigations only measured the γ-ray multiplicity at two incident energies, thus not being able to determine any nonlinear trend. Nevertheless, to the extent that valuable information can be extracted from these measurements, our results qualitatively agree with these investigations insofar as they also observe an increase in the number of γ rays with E_i. However, neither of these investigations could claim statistically significant results.

Lastly, we compare $\langle N_\gamma | E_i \rangle$ with model calculations. Both `FREYA` and `CGMF` are capable of predicting these regressions. Unfortunately, `FIFRELIN` cannot handle multiple-chance fissions, but its results conditioned on E^x will be shown in the next section. The agreement with `CGMF` is remarkable, with excellent agreement below the second-chance fission threshold. Above this energy, we do see that `CGMF` tends to react too strongly to the onsets of multiple-chance fission, with drops in the γ-ray multiplicities not reproduced in our data. Nonetheless, even above this energy `CGMF` closely reproduces the experimental results. On the other hand, `FREYA` predicts a much smoother relationship between $\langle N_\gamma \rangle$ and E_i, but its absolute scale and the predicted correlations are severely underestimated. All model calculations use evaluated yields as input, and are limited in the range $E_i < 20$ MeV.

3.4.1 Pre-fission excitation energy

The nonlinearity in the multiplicity of γ rays with incident energy is an artifact of the nonlinear relationship between incident neutron energy and the pre-fission excitation energy E^x. In fact, above the second chance fission barrier, the emission of neutrons before fission can significantly alter the excitation energy E^x of the target with respect to its energy immediately following the absorption of the incident neutron. We can correct for these nonlinearities

by determining the conditional means $\langle E^x|E_i\rangle$ using calculations performed with CGMF and reaction cross sections compiled in ENDF VIII [42]. The conditional means $\langle N_\gamma|E_i\rangle$ and $\langle E^x|E_i\rangle$ are associated with one another to form conditional correlations $\langle N_\gamma|E^x\rangle_{E_i}$. These conditional correlations are shown in Fig. 3.11. We see that the fit applied before the second-chance fission onset, shown in the figure, remains approximately valid above this threshold, $E^x > 12$ MeV. The occurrence of outliers near the discontinuity at $E_i \approx B_f$ is expected in these type of conditioned correlations.

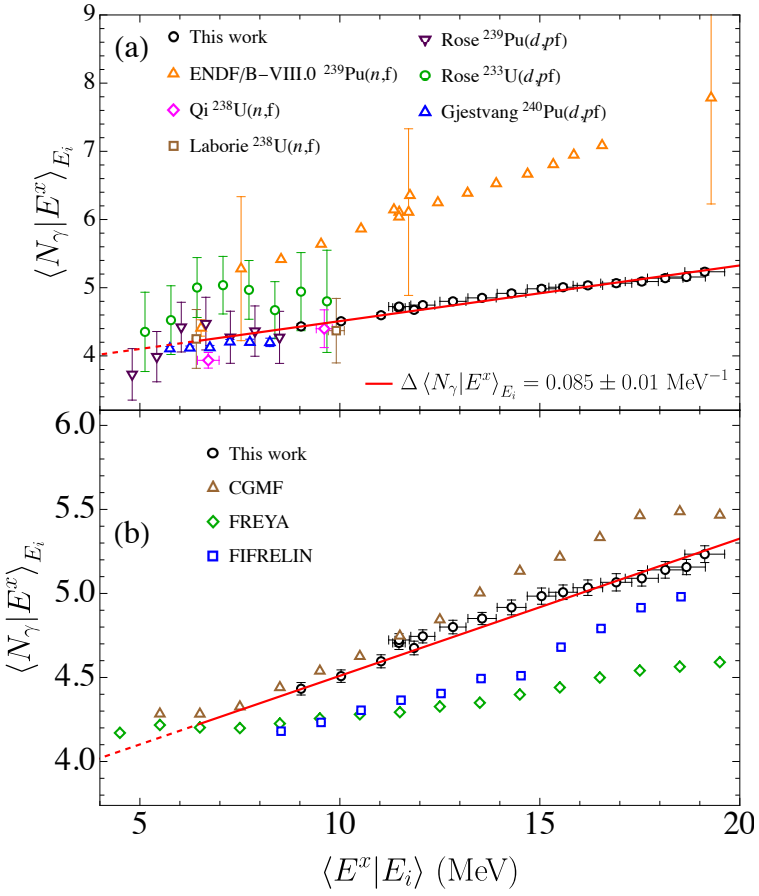

Figure 3.11: The correlations between γ ray multiplicity and pre-fission excitation energy E^x. A linear fit applied to the points with $E_i < B_f$ is also shown. Our experimental results are compared to literature data (a) and model calculations (b) [40].

In addition to the experimental investigations already shown in the previous section, we also show in Fig. 3.11 (a) the results obtained by Rose *et al.* [47] and Gjestvang *et al.* [48]. Both measurements were performed at the Oslo cyclotron accelerator, and involved the

stripping reaction of a deuteron on a target, *i.e.* the neutron from the deuteron is stripped and absorbed by the target nucleus, which then proceeds to fission. The stripping reaction controls the excitation energy E^x through inverse kinematics, by the measurement of the outgoing proton. The two measurements at the Oslo cyclotron differ in the isotope used as the fission target and thus the investigated reactions, namely ^{239}Pu(d,*p*f) for Gjestvang *et al.* and both ^{240}Pu(d,*p*f) and ^{233}U(d,*p*f) for Rose *et al.* These measurement differ rather strongly also in the level of uncertainties, with the latter having much smaller calculated systematic uncertainties than the former.

We find our measurement to be in good agreement with the linear slope predicted by Gjestvang *et al.*, the most precise of the data shown in Fig. 3.11 with a predicted an increase of 0.08 ± 0.02 γ/MeV in the ^{240}Pu(d,*p*f) reaction. Among the models, `CGMF` has the best agreement with the experimental data, with again too large dips corresponding to pre-fission neutron emissions. `FIFRELIN` predicts the correct slope, but slightly underestimates the number of γ rays in the acceptance. Lastly, `FREYA` predicts a slope that is too shallow, which does not reproduce the experiment.

To establish the dominant $E2$ nature of the γ rays increasing with E^x, we present in Fig. 3.12 the regression slope of the E_γ differentiated γ rays,

$$\left\langle \frac{dN_\gamma}{dE_\gamma} \middle| E^x \right\rangle_{E_i} , \tag{3.2}$$

with fits applied to both the entire E^x range as well as just those values corresponding to $E_i < B_f$. The agreement between these two sets of slopes indicates that there is evidence for linearity of the correlations across a larger energy range.

It is noted that the spectrum begins to develop a quadrupole resonance, similar to the one shown in Chapter II, at $E_\gamma \approx 0.7$ MeV. This resonance is a strong indication of the presence of stretched quadrupole transitions. In future work, we plan to pursue a study of the angular distribution of the γ rays to further validate the conclusion that stretched $E2$ transitions increase with E^x.

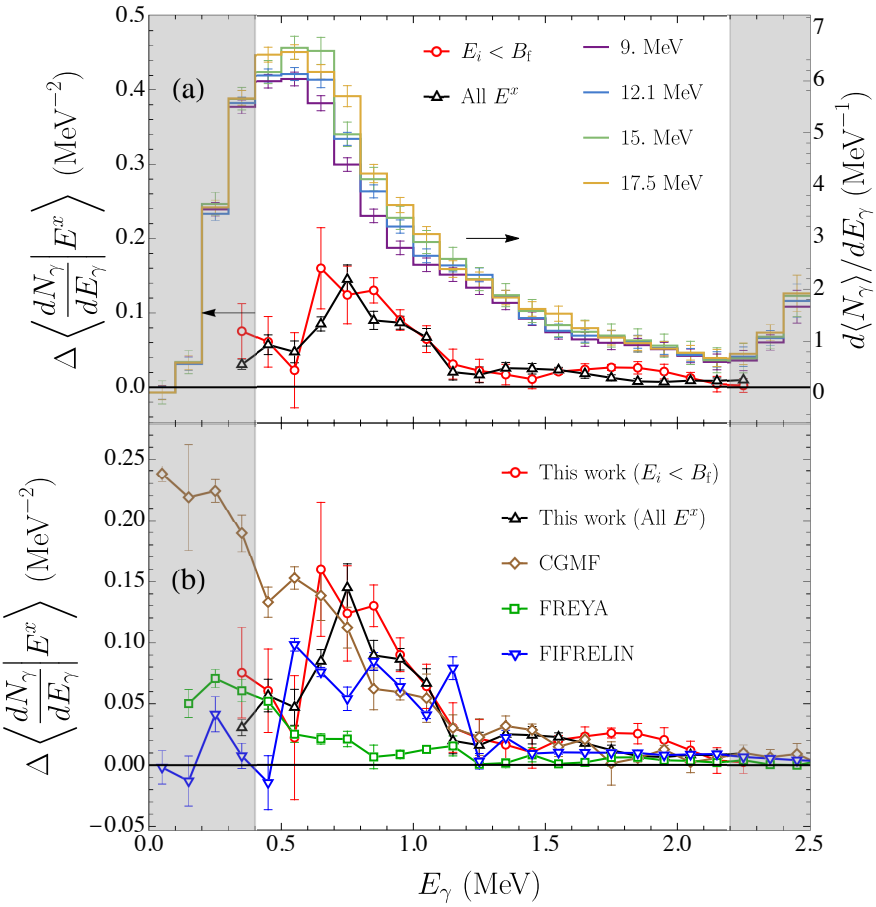

Figure 3.12: Linear regression slopes of the different portions of the γ ray spectrum with pre-fission excitation energy. We compare the fits applied to the entire energy range ($E_i < 20$ MeV), as well as just the points below the fission barrier ($E_i < B_f$). In (a) we show the γ-ray spectra for different excitation energy values, showing the development of a quadrupole resonance around 0.8 MeV. In (b), we compare the data to model calculations [40].

The comparison with model calculations shows that both `CGMF` and `FREYA` predict a preponderance of low-energy γ rays, and a strong quadrupole resonance is not observed in either of these codes. On the other hand, `FIFRELIN` reproduces the spectral enhancements rather well. This agreement is likely due to two causes: the inclusion of artificial levels in the levels scheme, connected using Hartree-Fock-Bogoliubov parametrization of the strength functions, and the strong E^*-J correlations modeled in `FIFRELIN`, which allow the angular momentum to grow with excitation energy and strongly populate rotational bands.

3.5 Discussion

We have determined that the contribution of statistical γ rays, representing a background to the signal of collective $E2$ emission we are interested in, is very small in the acceptance region of this experiment. Of the increase 0.081 ± 0.01 γ/MeV we have determined from the spectral analysis, shown in Fig. 3.12, that only 0.01 γ/MeV of the increase is due to statistical emission. Therefore, an increase of 0.07 γ/MeV can be attributed to stretched $E2$ transitions. The unusually low impact of statistical γ rays is due to the high γ-ray threshold.

We note that the energy E^x differs from the total fragment excitation energy E^*. In fact, fragments with larger E^x tend to have lower total kinetic energy, such that each additional MeV of energy in the pre-fission nucleus results in ≈ 1.3 MeV of fragment excitation energy, for the E_i range investigated in this chapter [49]. Therefore, knowing that stretched $E2$ transitions carry $J \sim 2$ $\hbar$ of angular momentum from the fragments, we can estimate that 0.055 ± 0.01 $\hbar$ of total angular momentum is added for each additional MeV of total fragment excitation energy. This roughly linear relationship is approximately valid in the range of total excitation energy $E^* \sim 24 - 38$ MeV, as determined in `CGMF`. As shown in Fig. 3.11, the correlations are indeed quite linear over this range of E^*. A slight concavity is seen to develop at the highest energies, which may be indicative of developing nonlinearities.

Finally, we recognize that there is a fundamental difference between neutron-induced fission and the spontaneous fission reaction discussed in the last chapter. With regard to angular momentum, it is known that spontaneously fissioning even-even isotopes, such as ^{252}Cf(sf), have a ground-state angular momentum of 0; on the other hand, neutrons absorption can lead to highly-excited nuclear states in ^{240}Pu* in the reaction ^{239}Pu(n,f). These states can have large values of intrinsic angular momentum that may affect the angular momenta of the fission fragments. This process of angular momentum transmission remains largely unknown and unexplored in the literature.

From both classical calculations and quantum mechanical considerations, it is possible to estimate that the change of intrinsic angular momentum of the fissioning nucleus due to the

incident neutron orbital angular momentum is $\sim 1\ \hbar$ at $E_i = 2$ MeV and $\sim 5\ \hbar$ at $E_i = 20$ MeV. If the angular momentum of the fissioning nucleus translated immediately to fragment angular momenta, it would result in a much larger increase in γ rays than observed in the experiment. Considering that we have already observed E^*-J correlations in ^{252}Cf(sf) where the angular momentum of the nucleus is 0, the data puts an upper bound of 20 to 30 % on the transmission of the angular momentum from the initial nucleus to the fragments.

Comparison of experimental data to model calculations provides further insight. The E^*-J correlations are virtually absent in `FREYA`, and the increase in the number of γ rays seen in Fig. 3.11 is predominantly attributed to an increase in statistical γ rays. These correlations are caused by the increase in the neutron separation energy with each emitted neutron, which leads to an increase in the statistical γ-ray yield. Thus, even in the absence of E^*-J correlations, we expect an increase in the γ-ray multiplicity. However, the energy signature of `FREYA` shown in Fig. 3.12 clearly indicates their statistical nature, with little to no structure near $E_\gamma \sim 0.7$ MeV. `CGMF` includes E^*-J correlations, and it thus predicts stronger γ-ray multiplicity correlations with E^x. However, neutrons and statistical γ rays remove a large amount of angular momentum, leading once again to an increase in the multiplicity of statistical γ rays. Some structure is seen to develop for the `CGMF` calculation around $E_\gamma \sim 0.7$ MeV, but not in sufficient agreement with experiment. The best agreement is found with `FIFRELIN`. While the absolute γ-ray multiplicity is slightly underestimated, the increase in the γ rays is due mostly to $E2$ emission, as shown in Fig. 3.12 and in good agreement with our experimental results. `FIFRELIN` has the strongest E^*-J correlations when we take into account that angular momentum is removed by neutron and statistical γ-ray emission. The agreement of `FIFRELIN` with experimental data is thus indicative of E^*-J correlations.

CHAPTER IV

Fragment-Based Correlations

4.1 Introduction

Experimentally, in a fragment-based investigation a fragment detector is used in coincidence with a radiation detector. The detection of neutrons and γ rays is then correlated in time with the fragments. The features of the particle emission can then be analyzed conditionally on the fragment yield. The history of fragment-based investigation is rich, and many seminal results have been obtained throughout the past five decades [5, 50, 51]. Early fragment-based investigations employed silicon surface-barrier detectors to measure fragment kinetic energies and directions. The properties of fragment-correlated neutrons have become benchmark measurements for new experiments and key observables for the development and validation of fission codes. As with all the other sections in this dissertation, γ-ray properties have lagged behind, with significant efforts in the late 1960s and early 1970s [3, 4, 5, 52], and then again in the 2010s and early 2020s [7, 8, 51]. The current chapter will therefore fill a gap in knowledge by providing data on fragment-correlated γ-ray emission, whereas neutron observables, already well studied in the literature, will be used for the purpose of calibration and validation of the measurement.

Fragment-based investigations of fission radiation emission give tremendous insight into the dynamics of the fission process. Specifically, the masses and kinetic energies of fis-

sion fragments are excellent probes of the di-nuclear separation, the fragment distortion at scission, and the amount of intrinsic energy available at scission. For the purpose of this dissertation, we perform a fragment-based investigation to determine the correlations between the fragment angular momenta and excitation energies. This determination is performed by inspecting the relationship between γ-ray multiplicities and fragment excitation energies, which can be approximately inferred on an event-by-event basis.

The result of this chapter is that the generation of angular momentum is statistical in nature, with variations in the production of angular momentum depending on the fragment masses created in fission. Furthermore, it is shown that the angular momentum saturates, *i.e.*, the angular momentum reaches a maximum value after which it becomes approximately independent of fragment excitation energy. Even more interestingly, the value of the saturated angular momentum does not appear to change with the fragment masses.

The experiment analyzed in this chapter is performed using a twin Frisch-gridded ionization chamber (TFGIC) that I have helped design and assemble at Argonne National Laboratory. Without the help and contributions of Fredrik Tovesson, Ivan Tolstukhin, Russell Knaack, and Michael Oberling, this project would not have been possible. Dana Duke and Dana's LANL team provided us with the analysis codes we used to write our fission fragment analysis scripts. Walt Loveland at Oregon State University prepared the Cf target for the experiment.

4.1.1 Outline

We begin this chapter in Section 4.2 with the description of the experimental setup, which consists of two parts, a fragment detector and a radiation-detection array, both of which I have participated in designing, assembling, and testing. The response of the detection system to both fragments and n-γ radiation is described in Section 4.3.

The results of the experiment are presented in Section 4.4. The main observables we present here are the conditionally differentiated neutron and γ-ray multiplicities with respect

to fragment masses and kinetic energies, as well as regression slopes of these observables. In Section 4.5 we discuss the experimental results and extract the E^*-J correlations we seek.

4.2 Experimental setup

The experiment analyzed in this chapter consists of two detector systems used in coincidence with one another: the fission sphere 3 (FS-3) trans-stilbene detection array, and the TFGIC fragment detector.

4.2.1 FS-3 array

The FS-3 detector array, shown in Fig. 4.1, consists of 40 organic scintillators arranged in spherical configuration. Each detector is a 5.08 cm by 5.08 cm right circular cylinder trans-stilbene crystal manufactured by Inrad-Optics. The crystal is optically coupled to a ElectronTube 9214B photo-multiplier tube (PMT). The assembly is wrapped in insulating tape, teflon to reduce optical noise, and mu-metal to reduce the effects of external magnetic field. Finally, the detector is held inside a 3D-printed plastic case which further reduces optical noise, and allows it to be easily handled.

The detectors are arranged in a spherical configuration, with detector holders assembled on three concentric rings. The rings are held in place by aluminum columns, which have been designed to be modular and allow for changes in the vertical position of the detector array. The support structure allows the detectors to be placed at a variable distance from the center of the sphere, from a minimum of 14 cm up to 27 cm. For this experiment, an intermediate distance of 22.5 cm is used. A detailed model of the detectors, the aluminum structure, and the surrounding room has been generated for MCNPX-PoliMi.

The detectors are individually powered using seven CAEN V6533 negative polarity power supplies. The power supply is connected via USB to the DAQ, and is operated through the CAEN GECO2020 control software. The high voltage (HV) on each PMT is adjusted to calibrate all detectors on the Compton edge of a ^{137}Cs source. The calibration is repeated

Figure 4.1: The FS-3 detection array at Argonne National Laboratory. The TFGIC is shown at the center the detector array. Also visible in the background is the electronic readout and high-voltage supply.

daily, but only minor corrections in the calibration are observed after the detectors are thermally equilibrated. The signal from each detector is individually digitized using CAEN V1730 digitizers, with 500 MHz digitization rate, and 2 V dynamic range. Each digitizer can read out 16 channels, and a total of three V1730 digitizers have been used in this experiment. The three digitizer clocks are synchronized with one another.

Just as with Chi-Nu, the detectors of FS-3 are sensitive to both neutrons and γ rays, and particle discrimination techniques are used to distinguish between them. The FS-3 flight path is significantly shorter than Chi-Nu, so we rely to a greater extent on PSD discrimination.

Fortunately, trans-stilbene has excellent PSD capabilities, as shown in Fig. 4.2. A threshold on the total light output of FS-3 of 20 keVee is applied during the measurement, but in analysis a threshold of 50 keVee is enforced to maintain n-γ discrimination. Due to the short flight path and the large time resolution of the TFGIC, neutron spectroscopy is not accurate in this setup.

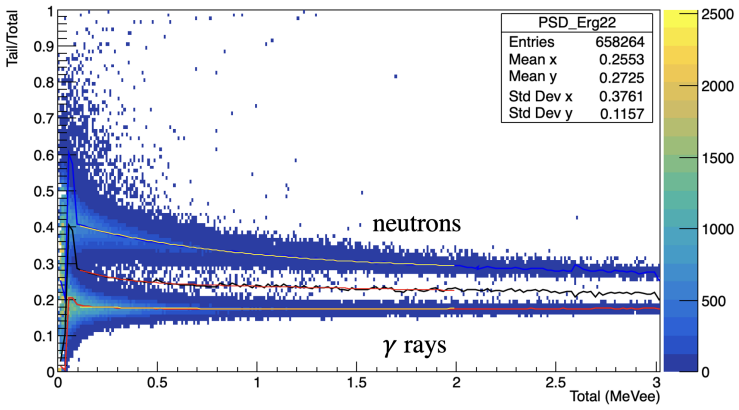

Figure 4.2: Histogram of the PSD parameter (tail/total) to the total light output in each detector (total). The interactions can be seen to divide into two bands, the bottom band characterized by a strong prompt signal, and the top characterized by a significant delayed-light component. These bands correspond to γ-ray and neutron interactions, respectively.

4.2.2 TFGIC

The TFGIC used in this experiment is inspired by the design by Dana Duke [53], with modifications employed to reduce the attenuation of neutrons and γ rays. TFGIC have become very popular in fission studies, and there is a rich literature on their functioning and modes of operation. We maintain the discussion in this section brief, and refer the reader to Refs. [50, 54, 55, 56].

A schematic drawing of the TFGIC used in this experiment is shown in Fig. 4.3. The fragment detector is composed of two identical volumes enclosed between the central cathode plate and the two anode plates. The inner diameter of the chamber is 140 mm and the distance between cathode and anode boards is 47 mm. To minimize the attenuation of the

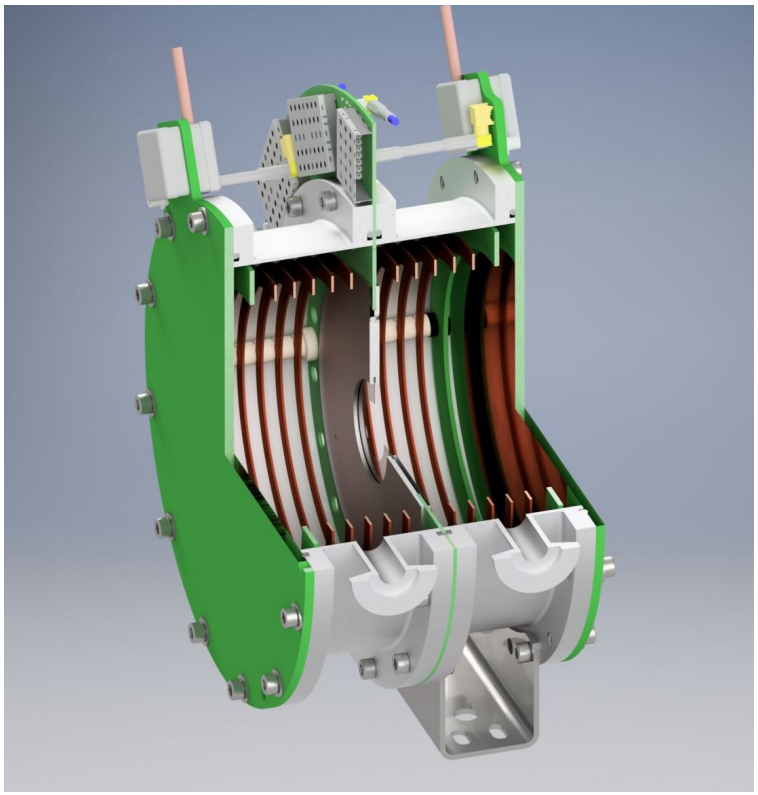

Figure 4.3: Schematic drawing of the TFGIC designed and assembled at Argonne National Laboratory.

radiation, the anode and its associated circuitry are combined in a single 4-layer printed circuit board (PCB). Similarly, the cathode and the associated electronic circuitry, as well as the pre-amplifiers from all the TFGIC signals, are contained in a single PCB.

Frisch grids are used in ionization chambers to eliminate geometric effects from the anode signal, *i.e.*, the dependence of the signal on the direction of the ion track, and to improve the timing resolution of the detector. In this experiment, as has been conventionally done with TFGICs, the signal of the grid and the anode can be compared to extract the polar angle of emission of fragments with respect to the chamber axis. The grids are made of 20 μm gold-plated tungsten wires spaced 1 mm apart and soldered to PCB rings. Frisch grids are placed between the cathode and the anode at a distance of 7 mm from the anode.

The chamber is filled with P-10 gas, Ar(90%)+CH_4(10%)m at 950 torr with continuous flow of 500 cc/min. Each of the two chamber sections of the twin chamber has a gas port,

respectively used as gas inlet and outlet. To allow the gas circulation between sections, 8 holes of 6.5 mm diameter are located on the cathode board on the opposite side of the gas ports. The gas pressure is monitored. Variations on the order of 10 torr have been observed but the signal is not visibly influenced by these small variations.

The TFGIC detector volume is electrified by holding the cathode at a potential of -1500 V, the two grids grounded at 0 V, and the anode boards at $+1000$ V. These potential differences are supplied by CAEN N1470 power supplies. The produced electric field is rectified and made uniform across the chamber through the use of copper *field rings*, five in each chamber section. The field rings are mounted on peek plastic columns that are mounted directly on the cathode board.

A spontaneous fission source is prepared by molecular deposition of 9 kBq of ^{252}Cf on a 100 μm/cm^2 carbon foil. The diameter of the deposit on the backing is 10 mm, and it is determined that the source is offset by about 2 mm with respect to the center of the TFGIC. This effect is deemed negligible, since this distance is much shorter than both typical fragment ranges and the dimension of the detector active volume.

The five signals generated by the TFGIC — one cathode, two grids, and two anodes —are passed through Cremat CR-110 preamplifiers mounted directly on the cathode board, outside of the aluminum walls of the chamber. The preamplified signals have a short rise time, $\sim 20 - 25$ ns, and a long decay time of 150 μs. The grid signals are digitized using a CAEN V1740 digitizer, with 12-bit resolution over a 2 V dynamic range and a 62.5 MHz sampling rate. The signals from the anodes and the cathode are cloned using a CAEN N454 module, with one of the copies of each channel being digitized in the V1740. Three clones of each of the anode boards are provided in channels 0 and 1 of the three V1730 digitizers for coincidence purposes. A clone of the cathode signal is provided to one of the V1730 digitizers, where a digital CFD algorithm determines its timing. We have determined a time resolution of $\approx 5 - 6$ ns FWHM. Another copy of the cathode signal is provided to an oscilloscope and used as a diagnostic.

Aluminum foil is used in the experiment to wrap the sections of the chamber, providing a Faraday cage that reduces electronic noise. We have designed an aluminum bracket and holder system, composed of aluminum and 3D-printed components, that allows the chamber to be re-positioned vertically within FS-3. The holder system also allows the chamber to be rotated. The chamber is aligned with the source at the geometric center of the FS-3 array, and with the axis of the chamber - i.e. the line of shortest distance between cathode and anode, pointed in the direction of one of the trans-stilbene detectors.

Data are collected from the detectors and chamber only when a double coincidence on the two anode boards is observed. This coincidence AND logic significantly lowers the background and virtually eliminates the effects of α decays, as can be determined by pulse-height spectroscopy and comparison of the chamber throughput to the nominal source activity.

The signals from the chamber are analyzed using the $2E$ method. This rather involved technique, explained in full detail in Dana Duke's dissertation, see Ref. [53], uses the fragment kinetic energies to infer their masses through conservation of linear momentum and nucleon number. The procedure is repeated recursively because the fragment kinetic energies are determined from both the chamber signals as well as mass-dependent corrections, including the estimated emitted neutron multiplicities and attenuation effects.

4.3 Experimental response

The response of the system can be divided once again in two components: the response of the FS-3 detector array to neutron and γ ray emission, and the response of the TFGIC to the fragment properties. Conceptually, the FS-3 response can be treated similarly to the way the Chi-Nu response was treated in Chapter II, so more attention will be devoted in this section to the response of the fragment detector, which is new to this experiment.

Unfolding matrices have been constructed for both neutrons and γ rays, yielding acceptance regions of $0.24 < E_\gamma < 3$ MeV and $0.8 < E_n < 10$ MeV. We have determined that for the detector distance used in this experiment, the absolute detection efficiencies are

$\epsilon_\gamma = 0.032$ and $\epsilon_n = 0.036$. The TFGIC and related structures introduce some attenuation of the radiation emitted by the ^{252}Cf source. These effects are simulated in MCNPX-PoliMi, where an accurate model of the ionization chamber is implemented.

4.3.1 TFGIC response

The quantities of interest we want to extract from the ionization chamber are the yield observables: the fragment masses, A, and the total kinetic energy release, TKE. While not of direct physical relevance, the angle of fragment emission determines the corrections for fragment attenuation in the target backing.

The fragment angle of emission is determined by the ratio of the signal induced on the grid to the signal induced on the anode. Thus, the angle is determined independently on either identical TFGIC section. Because fragments in spontaneous fission are emitted back-to-back, the variations between the two independent measurements are used to assess the angular resolution of the TFGIC. Fig. 4.4 shows the difference between the angle determined from the two sides of the chamber. We found an angular resolution of 0.11 FWHM in cosine bins. In data analysis, we will take the fragment angle to be the average between the angles on either side. Thus, we expect an angular resolution of ~ 0.06 FWHM.

The kinetic energy of fission fragments is determined primarily by the signal induced on the anodes. These signals are corrected for grid inefficiencies, *i.e.*, the stray signal induced in the anode as the charge drifts behind the grid, the energy loss in the ^{252}Cf sample and its backing, which has a strong angular dependence, and the pulse height defect, an energy dependent correction addressing the impact of charge recombination in the gas. The kinetic energy is further corrected by reconstructing the energies prior to neutron emission using the mean value $\langle N|A, \mathrm{TKE}\rangle$ determined by Göök *et al.* [50]. However, the fragment mass A is determined by comparing the fragment kinetic energies, and thus the masses and kinetic energies are simultaneously determined in a recursive loop.

Due to the large fragment attenuation in the target and its backing, we find that data

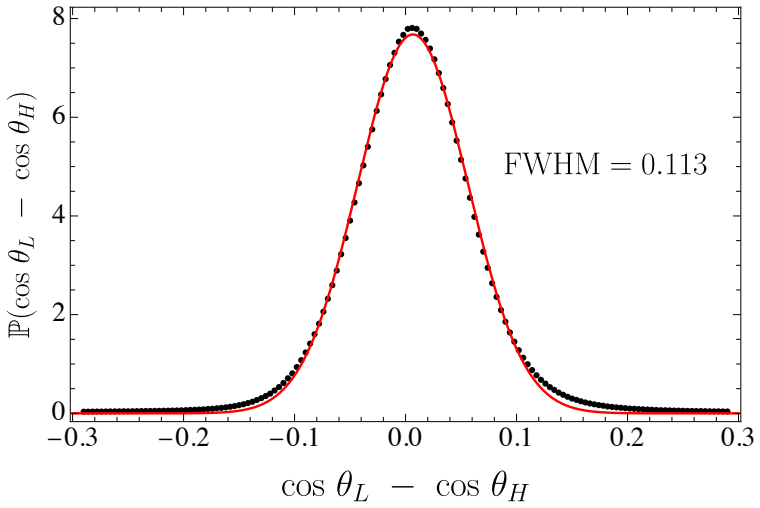

Figure 4.4: Difference between the angles determined by either side of the chamber, which ideally would be identical. The width of this distribution is indicative of the angular resolution of the TFGIC. The red line is an illustrative Gaussian fit applied to the data

still contain angle-dependence in the kinetic energy distributions, even after these effects are addressed with the method indicated in Ref. [53]. To avoid these problems, we selected a narrow emission angle, $|\cos\theta| > 0.9$.

The mass resolution of the TFGIC is shown in Fig. 4.5, where it is compared to the data obtained by Göök *et al.* [50]. We note that because of symmetry, we only need to plot the yield as a function of the light fragment mass A_L, as the same yield would be observed for the complementary fragment of mass $A_H = A_0 - A_L$, where $A_0 = 252$ is the mass number of ^{252}Cf. The agreement between the two experiments is quite good across the mass yields, with some deviations near symmetric fission, $A \gtrsim 120$. Generally, our distribution is slightly wider than the one inferred by Göök *et al.*, indicating a worse mass resolution, approximately $4 - 5$ FWHM.

The distribution of TKE conditioned on the light fragment mass is shown in Fig. 4.6. The figure shows both the mean and the standard deviation of the determined kinetic energy release. The mean kinetic energy is indicative of the accuracy of the TFGIC, while the standard deviation is indicative of its energy resolution. The determined mean $\langle \mathrm{TKE}|A\rangle$ is

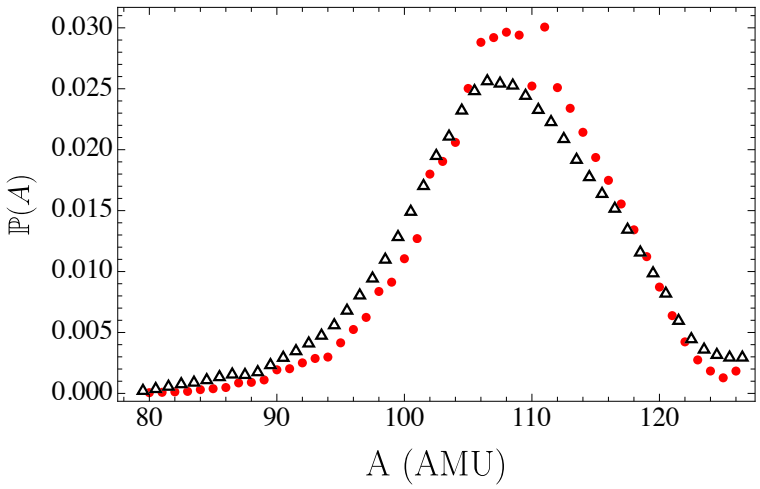

Figure 4.5: Fragment mass yield determined by the TFGIC, black points, compared to the yield determined by Göök *et al.* [50], shown as red points.

found to be in good agreement with Göök *et al.*, with slight deviations at $A \approx 120$. The width of the TKE distribution is larger than the reference experiment throughout the entire mass yields, indicating a kinetic energy resolution of approximately $3 - 4$ MeV FWHM.

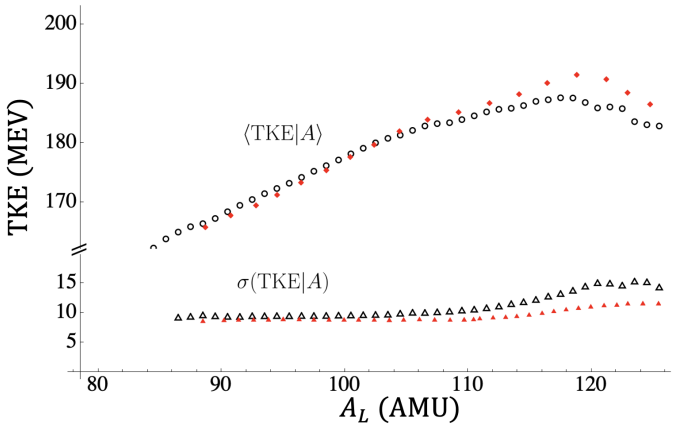

Figure 4.6: Average and standard deviation of the TKE distribution determined by the TFGIC, black points, compared to the yield determined by Göök *et al.* [50], shown as red points.

4.4 Results

The primary result of this chapter are the correlations between γ-ray multiplicities and the total excitation energies of fission fragments E^*,

$$\langle N_\gamma | E^* \rangle \ , \tag{4.1}$$

which will highlight the connection between the fragment angular momenta and excitation energy. The excitation energy is not an observable quantity, but it is derived from the energy balance equation

$$E^* = Q(A,Z) - \mathrm{TKE} \ . \tag{4.2}$$

The total kinetic energy is an observable that can be measured by the TFGIC, while the total energy release Q depends on the mass split. The fragment charge Z, while not an observable in this experiment, can be inferred from Wahl empirical formula [57], which dictates that the average charge distribution in the fragments is the same as that of the initial target nucleus, with a dispersion of approximately $\sigma(Z|A) \approx 0.5$. Even-odd effects in nuclear binding masses lead to rather large variations of the Q value. Considering both the mass resolution as well as the charge dispersion, the TFGIC is capable of determining the event-by-event total excitation energy, E^*, to within 4-5 MeV FWHM. Given this discussion, it is clear that the quantity in Eq. 4.1 can be inferred from the general differential

$$\langle N_\gamma | TKE, A \rangle \ , \tag{4.3}$$

i.e. the simultaneous conditional differentiation of N_γ with respect to both mass and kinetic energy.

4.4.1 Independent analysis

We begin by presenting the conditional differentiation of γ-ray multiplicity with respect to mass and kinetic energy separately since existing experimental data is available for comparison. These quantities have been investigated before, but much uncertainty remained on their validity until a recent paper by Travar *et al.* [8] performed the most accurate measurement to date of these correlations. We compare the results from these investigation to results we have determined in our system in Figs. 4.7 and 4.8. On the same figures, we also compare the neutron emission results to Göök *et al.* [50]. The neutron comparison serves as validation of our γ-ray results. The results of this comparison show that due to the resolution achieved by our system so far, which is slightly larger than the resolution achieved by Göök *et al.*, the features of the multiplicity distributions are slightly broadened, and the correlations of particle multiplicities with fragment mass and kinetic energy are slightly weakened.

In Figs. 4.7 (b) and 4.8 (b), the measured γ-ray emission results are compared to model calculations performed with `FREYA`, `CGMF`, and `FIFRELIN`. It is interesting to note that all codes predict structure in the dependence of the γ-ray multiplicity on mass, which actually is more indicative of correlations between statistical γ-ray emission with varying neutron separation energies rather than angular momentum correlations with E^*. In fact, the neutron separation energy varies considerably over these mass ranges, especially near the shell closure at $A = 132$.

When conditioned on TKE, we observe the same behavior already observed by Travar *et al.* [8], the γ ray multiplicity increases with decreasing TKE until TKE $\approx$ 180 MeV, below which the γ-ray multiplicity stops growing and levels off, and even starts to slightly decrease.

4.4.2 Excitation energy analysis

Finally, we come to the main results of this chapter, namely the dependence of γ ray multiplicity on excitation energy E^*. We show in Fig. 4.9 the dependence of γ-ray multiplicity on the total fragment excitation energy, as determined from Eq. 4.2. The experimental data

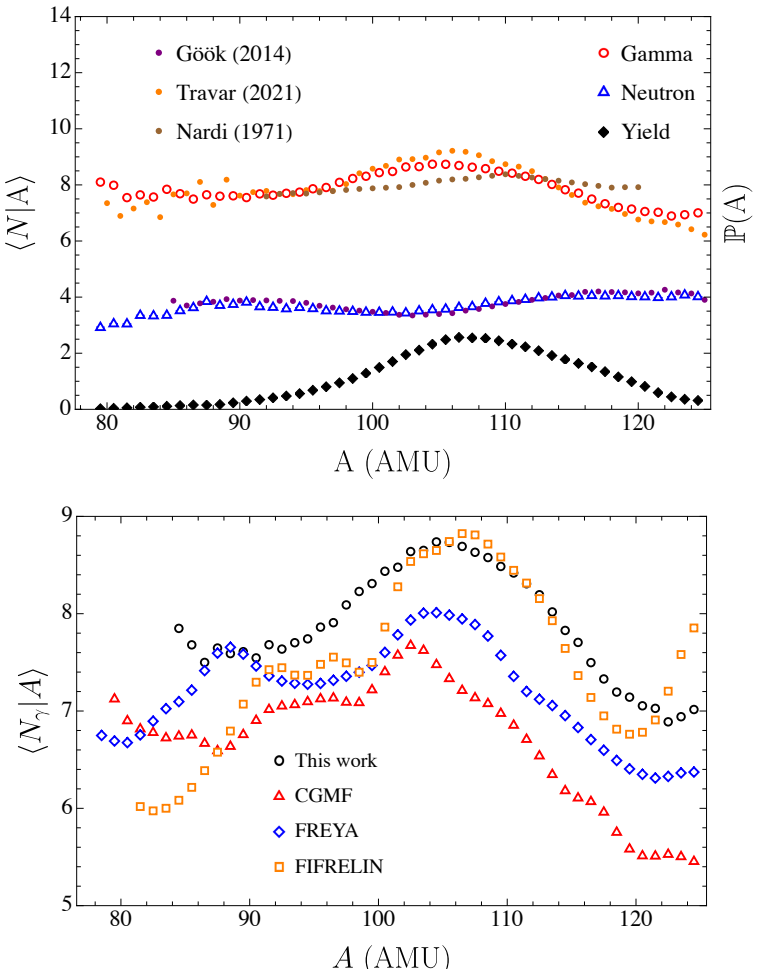

Figure 4.7: Comparison of particle multiplicities dependence on the fragment mass. Note that these results include emission from both fragment, and the mass indicates the mass of the light fragment. In (a) neutron and γ-ray multiplicities are compared to past experiments performed by Göök *et al.* [50] and Travar *et al.* [8]. The yield of fragment TKE is also shown, using the right vertical axis. In (b), the measured γ-ray emission is compared to model calculations.

are compared to model calculations. In the models, the excitation energy is not inferred, but is the actual excitation energy predicted by the models.

It is seen from Fig. 4.9 that $\langle N_\gamma \rangle$ *saturates* at high excitation energies. The γ-ray multiplicity reaches a maximum value of approximately $8-9$ above which it does not increase significantly. We can also observe a slight negative downturn at the highest E^*. While the saturated γ-ray multiplicity appears to be the same for all of fragment masses, $\langle N_\gamma \rangle \sim 8$, the excitation energy required to reach it varies significantly.

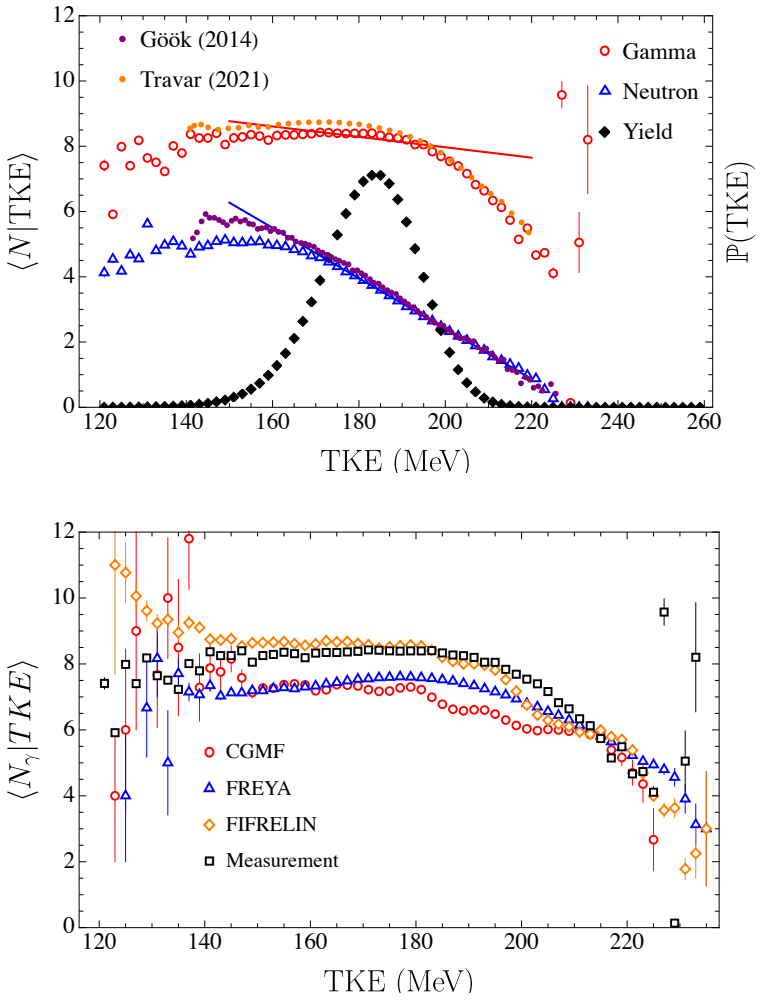

Figure 4.8: Comparison of particle multiplicities dependence on the fragment TKE. In (a) neutron and γ-ray multiplicities are compared to past experiments performed by Göök *et al.* [50] and Travar *et al.* [8]. The yield of fragment TKE is also shown, using the left vertical axis. In (b), the measured γ-ray emission is compared to model calculations.

An important observable that can be extracted from the results shown in Fig. 4.9 is the linear regression slope. It is clear that the increase in γ rays is highly nonlinear; nonetheless, a linear fit to the regression, using relative yields of excitation energies as weights, can be used to reveal important features of γ-ray emission. The regression slope for γ rays is shown in Fig. 4.10. Also shown on the figure are the regression slopes for neutrons, shown again to validate the γ-ray results. The neutron linear regression slope on E^*, equivalent in magnitude to the regression slope against TKE for fixed masses, is in good agreement with the past

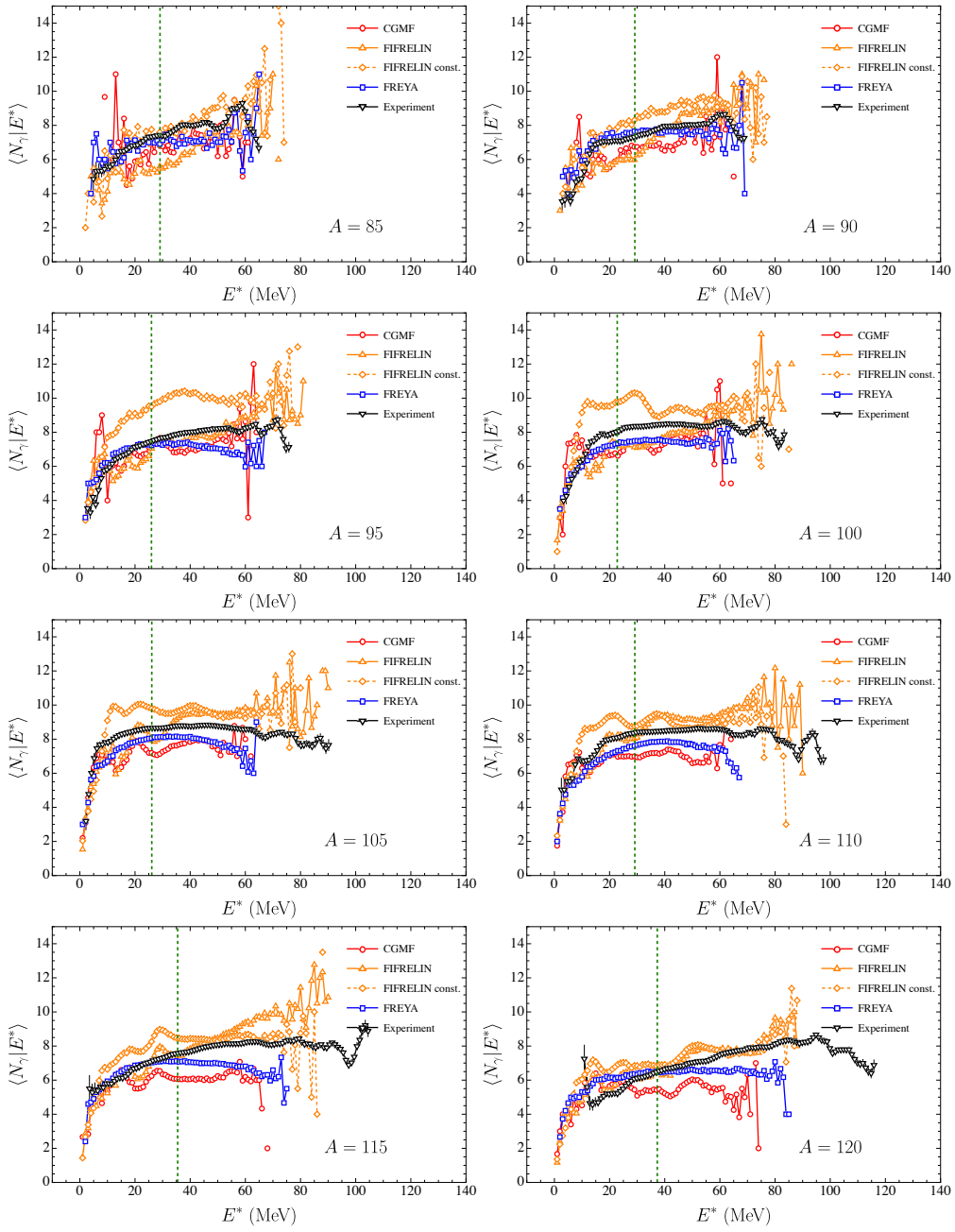

Figure 4.9: Measured γ-ray multiplicities against the inferred excitation energy compared to the results of model calculations. The results are given for specific light fragment masses, and the γ rays are summed between the two partner fragments. The green dashed line represent the average excitation energy we determined for that fragmen pair

investigation by Göök *et al.* The γ-ray results are compared to two previous results: the first by Nifenecker *et al.* [3], and the second by Schmid-Fabian and Glässel *et al.* [14].

Our results deviate from both prior results, as they show a pronounced mass dependence, at variance with Glässel *et al.*, but a magnitude much smaller than that determined by Nifenecker *et al.* The previous investigations have been criticized in the past. The results by Glässel *et al.* have been found to be at odds with recent experimental results by Travar *et al.*, while Nardi *et al.* [52] have pointed out that Nifencker *et al.* could have been biased by an inaccuracy in their neutron removal techniques.

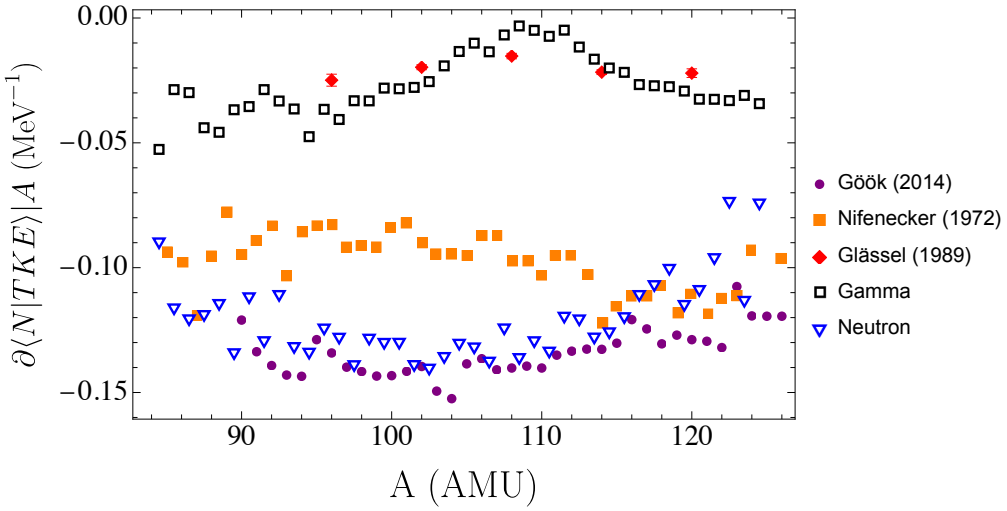

Figure 4.10: Linear fit to the regression of γ rays and neutrons on excitation energy. The measured results are compared to past experiments.

We also show here the energies of γ rays that correlate most strongly with excitation energy. In Fig. 4.11 we show the linear regression slope of the energy-differentiated γ-ray spectrum and its dependence on the excitation energy. We see that the slopes show a clear enhancement around $E_\gamma \approx 0.7$ MeV, and also enhancements at higher energies.

4.4.3 Angular distribution

We present the angular distribution of γ rays with respect to the fission axis, *i.e.*, the direction of motion of the light fission fragment. The angular distributions are further conditioned on the mass of the light fragment to show how the anisotropy of γ rays changes with the mass split. The data are measured by a single detector collinear along the axis of the

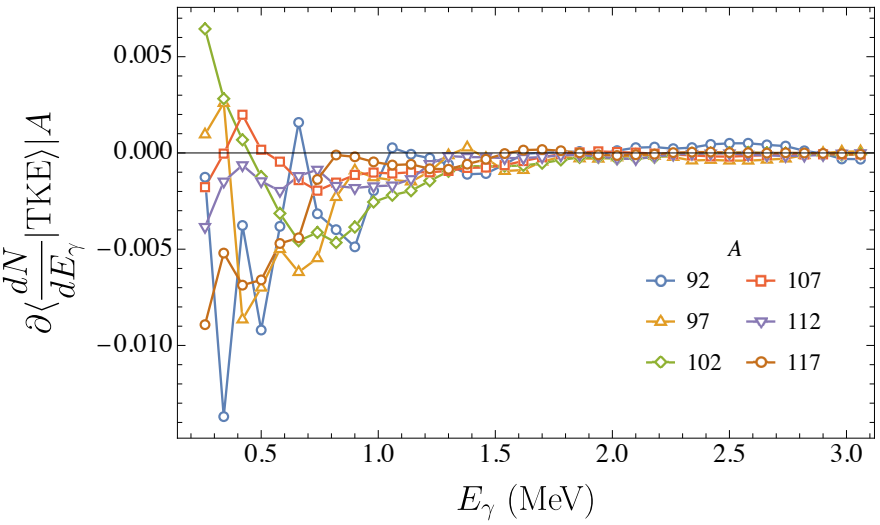

Figure 4.11: Linear regression slopes of γ spectrum on E^* for several fragment masses. The γ rays from both fragments are summed.

ionization chamber. Thus, the angle between the fission axis and the TFGIC, an observable of this experiment, corresponds to the angle of the fission axis with the measured γ ray. Because the chamber is not sensitive to fragments emitted approximately perpendicular to its axis of cylindrical symmetry, only angles $|\cos\theta_F| > 0.3$ are measured.

Our experimental data are in good agreement with the data measured by Kopach *et al.* [58], which were corrected for γ-ray aberration. The agreement with Oberstedt *et al.* [59] is satisfactory, but their correlations appear to be stronger.

The distribution is not symmetric due to a combination of Doppler effect, which increases the yield of γ rays in a direction parallel to the motion of the source, and chamber attenuation anisotropies. Figure 4.12 clearly shows that there exists a strong impact on the anisotropy of γ rays with fragment mass. Specifically, we find that the γ rays are emitted most anisotropically by fragments near the center of the fragment yield $A_L \sim 100-110$, and are more isotropic for very asymmetric and symmetric fissions.

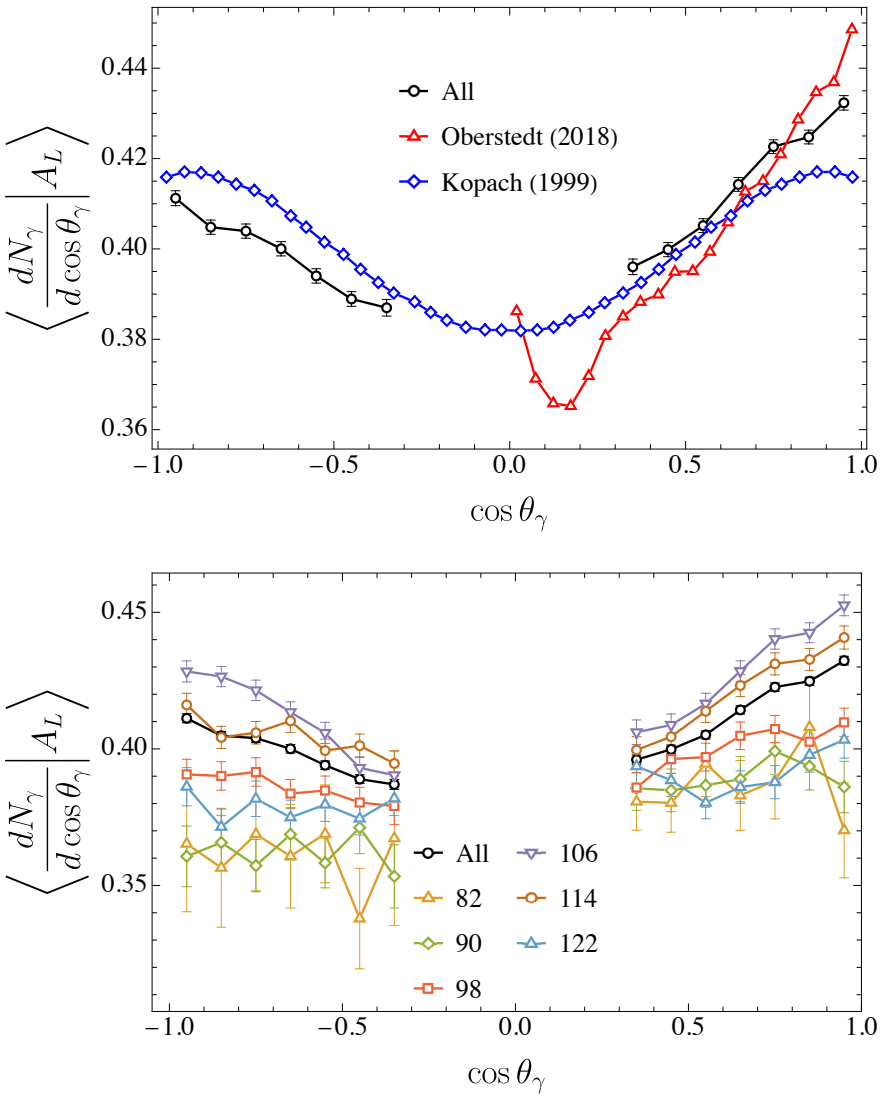

Figure 4.12: Angular distribution of γ rays with respect to the fission axis for several fragment mass splits, based on the light fragment mass. The γ rays are not differentiated with respect to light and heavy fragment, so their yield is summed. The lines labeled "All" are the average of the experimental data over the entire fragment-mass yield.

4.5 Discussion

The increase in γ rays with E^*, after all statistical γ are emitted, is caused by a coupling of the angular momentum to the excitation energy. These correlations would result in an an increase of $E2$ transitions along rotational bands, with a characteristic energy signature around $E_\gamma \sim 0.7$ MeV, as already observed in Chapters II and III. Once again, these energy

have been found to be strongly correlated with excitation energy, as seen in Fig. 4.11.

The γ ray slopes shown in Fig. 4.10 should then be proportional to the increase in angular momentum with excitation energy $\Delta\langle J|E^*\rangle$, with a correction due to the increase in separation energy with neutron emission, which result in an increase in statistical γ rays with excitation energy. The results of this chapter are consistent with the results from Chapters II and III. The regression slope of γ rays on excitation energy gives a value of approximately 0.02 γ/MeV that, assuming it originates only from an increase in collective γ rays, corresponds to an increase of $\approx 0.04\ \hbar$/MeV. This result is slightly lower than those predicted in the previous chapters, but it is still in qualitative agreement.

While the methods of linear regression explain the correlations enhancements of Chapter II, we have observed strong non-linearities in the γ-ray correlations with E^*. In fact, the main result of this chapter is that the angular momentum saturates at high E^*. That is, our measurement indicates that the sum of the angular momenta of fission fragments depends on the total excitation energy E^* only up to a mass dependent energy, above which it becomes independent of E^*.

We have observed that after the angular momentum saturates, it can also start decreasing with increasing E^*. We find two types of decrease: a slight steady smooth decrease, for example seen in $A = 105$ in Fig. 4.9, and a sudden drop, seen at the highest available energies in all fragment pairs. The first effect is likely due to the angular momentum removed by neutrons and statistical γ rays, which has only a very small effect. The second effect is more puzzling; Gonnenwein *et al.* [9] observed a similar trend in the angular momentum of ^{134}Te, and explained it in terms of the deformation energy. In their explanation, Gonnenwein *et al.* postulate that the highest excitation energy given a fixed fragment mass, is the one with the lowest amount of kinetic energy. This reduction of fragment kinetic energy can only be possible if the fragments are extremely deformed, with most of the excitation energy E^* stored in deformation, and thus not available to excite rotational modes. We shall discuss this effect in more depth in Chapter V.

We bring attention now to the feature shown at the lowest excitation energies in Fig. 4.9. This feature correspond to a sudden decrease in γ ray multiplicities correlated with the emission of the first neutron. This effect should be interpreted as the drop in the statistical γ rays when the first neutron is emitted, and has no consequence for the angular momentum. On the other hand, the lack of notches at high E^* is another indication that neutron emission does not dissipate a large amount of angular momentum.

We have observed that, while the angular momentum appears to saturate for all fragment pairs, the *saturation point* has a strong mass dependence, with a low saturation energy for $A_L \sim 100 - 110$, around $E^* \sim 20$ MeV, and much higher for light-fragment masses heavier and lighter than this. This observation can be explained in terms of shell corrections to the level density parameters. In fact, the masses around $A_L \sim 100 - 110$ and $A_H \sim 140 - 150$ correspond to fragments with many particles outside of closed neutron and proton shells. The abundance of these particles implies strong shell corrections to the level density parameters.

The angular distribution of γ rays allows us to infer that the polarization of fragment angular momenta is not effective in very asymmetric and symmetric fission. While on average it is true that fragment angular momenta are polarized perpendicular to the fission axis, this is not the case across the fragment mass yield. In fact, we cannot attribute the loss of anisotropy in SD events purely to a reduction of angular momentum since the multiplicity of γ rays decreases by less than one unit, indicating that the magnitude of the angular momentum is only weakly affected. Furthermore, the studies by Wilson *et al.* [7] indicate that the angular momentum of far-asymmetric fission fragments, $A \lesssim 100$ is in fact larger than for standard fission fragments $A \sim 100-110$. Thus, the anisotropy cannot be attributed to a decrease of the total angular momentum and thus of stretched quadrupole transitions, but rather to a decrease in the polarization of the fragment angular momentum in a direction perpendicular to the fission axis.

CHAPTER V

Angular Momentum of Fission Fragments

The final technical chapter of this dissertation serves as a distillation of the results of Chapters II-IV. The purpose of Section 5.1 is to summarize all the experimental evidence we have gathered in this dissertation, as well as evidence from past experiments, and synthesize them down to a list of observations concerning to the fission fragment angular momenta. The observations we make of n-γ emission can constrain the theoretical models of angular momentum. In Section 5.2 we present a critique of current theoretical models of fission fragment angular momenta. Lastly, we propose a new mechanism for angular momentum generation that may shed light on this problem.

The content of this chapter is partially based on discussions held at the workshop on the angular momentum of fission fragments in Seattle, in June 2022. I especially thank J. Randrup, A. Bulgac, I. Abdurrahman, G. Scamps, J. Wilson, and G. Bertsch for fruitful discussions. A recent publication by N. Schunk and D. Regnier [60], has very recently highlighted the importance of spontaneous symmetry breaking in fission. I was not aware of this publication at the time of writing, but I believe it to be a good introduction to the importance of vibrational motion in fission.

5.1 Discussion of experimental evidence

We begin by summarizing everything we know about the fragment angular momenta as inferred from neutron and γ-ray emission, as well as the fragment properties themselves. These observations are divided into two categories: magnitude and direction.

5.1.1 Magnitude

It has been established in the literature that the magnitudes of the individual fragment angular momenta are approximately $6 - 8\hbar$ [5, 7]. Recently, Wilson *et al.* [7] showed that the fragment angular momentum follows a sawtooth distribution with respect to fragment mass, see Fig. 5.1, with minima corresponding to closed-shell fragments at $A_L = 78$ and $A_H = 132$. This sawtooth is reminiscent of an earlier observation by Wilhelmy *et al.* [5] that the fragment angular momentum is strongly correlated with its ground state deformation [5]. Wilson *et al.* interpret their results in terms of a correlation between angular momentum and nucleons in excess of the closed shell configurations. Nonetheless, it has also been observed by Gonnenwein *et al.* [9] and Chebboubi *et al.* [15] that spherical fragments, $A_H \sim 132$, can acquire angular momentum, although the magnitude of the spin of spherical fragment is suppressed on average, but with a significant energy dependence. The suppression of the fragment angular momentum near shell closures is also clear from the existence of the γ-ray sawtooth, as confirmed by Travar *et al.* [8].

In this dissertation we proved that there exist complex E^*-J correlations. Specifically, we have found highly nonlinear positive correlations at low E^*. The angular momentum saturates at a value of $J_L + J_H = J \approx 15 - 20\ \hbar$ as one can estimate from `FIFRELIN`. Here J_L, J_H represent the individual light and heavy fragment angular momenta magnitude, respectively. This result confirms the observations by Travar *et al.* [8] and Chebboubi *et al* [15]. Finally, our data show that J_s is approximately independent of the fragment split. The fragment masses, however, do have a strong effect on the excitation energy at which this saturation occurs.

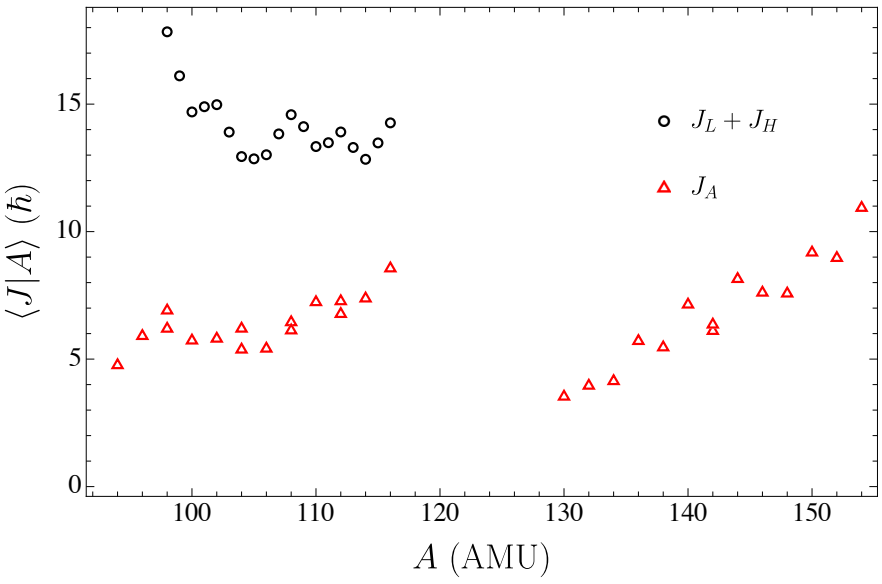

Figure 5.1: Fragment mass dependence of fragment angular momenta in ^{252}Cf(sf) for both single fragments as well as the sum of the angular momenta of both fragments [7].

The existence of an excitation energy dependence on the total angular momentum has been confirmed by all three experiments analyzed in this dissertation. In fact, the existence of E^*-J correlations in Chapter II is interpreted as a local derivative of J on E^* when the former is not fully saturated. Our data in Chapter IV indicate that J drops at the highest values of E^*, in agreement with previous observation by Gonnenwein *et al.* [61]. Specifically, Gonnenwein *et al.* hypothesize that this drop is caused by the scarcity of free excitation energy for hyper-deformed nuclei, all the excitation energy being found in the strong nuclear deformations.

We have found that fragments from fissions with $A_L \sim 100 - 110$ reach their saturated J quickly, $E^* < 20$ MeV, while fragments with $A > 110$ and $A < 95$ tend to saturate at higher energies. This effect is understood in terms of the statistical hypothesis of angular momentum generation, coupled with shell and deformation effects, and a saturation cutoff. In fact, fragments from fissions with $A_L = 100 - 110$, in ^{252}Cf(sf), are the ones with the most nucleons outside of major shells, giving rise to large deformations and shell effects on level densities. The data by Wilson *et al.* also indicate that the total angular momentum

- the sum of both fragment angular momenta shown in Fig. 5.1 - remain approximately unchanged across fragment mass splits. Even more interestingly, data for $A_L < 100$ appear to deviate from the model behavior and give rise to even larger total J than other fragment splits. Therefore, while the more spherical fragments, or more correctly fragments that are spherical in their ground state, receive a reduced share of the total angular momentum in fission, the total angular momentum itself tends to be higher or remain unchanged with mass asymmetry.

We understand the mass dependence of J in terms of neutron-proton shell closures. Looking at Fig. 5.2, we see that light fragments with $A_L \sim 100 - 110$, and their corresponding heavy fragment, have many particles outside of closed shells and are therefore more deformable. Larger and smaller light-fragment masses are associated with nuclei closer to shell closures, and are thus less deformable. Particularly, for larger A_L the heavy fragment tends to be spherical, while for lighter A_L it is the light fragment that tends to become spherical. Thus, these observations are understood in terms of fissioning systems in which one of the two fragments become more spherical, leaving the other approximately deformed. We note that we do not have access to the fragment deformation at the moment of fission, so this discussion assumes that the fragment deformation is related to their ground-state deformation.

We have determined in this dissertation, using data from neutron-induced fission of ^{239}Pu, that the angular momentum of the compound nucleus is not transmitted significantly to the fragment angular momenta. In fact, combining the results of Chapters III and IV, we estimate that increasing the angular momentum of the compound nucleus by one unit raises the total fragment angular momenta by at most 0.3 units, if at all. The observation that the angular momentum continues to increase with excitation energy over the estimated range $24 \leq E^* \leq 38$ MeV seems to be at odds with the saturation effect. However, we must note that the fragment yield of ^{239}Pu(n,f) is concentrated around spherical heavy fragments. It will be interesting to repeat fragment-based experiments with a ^{240}Pu(sf)

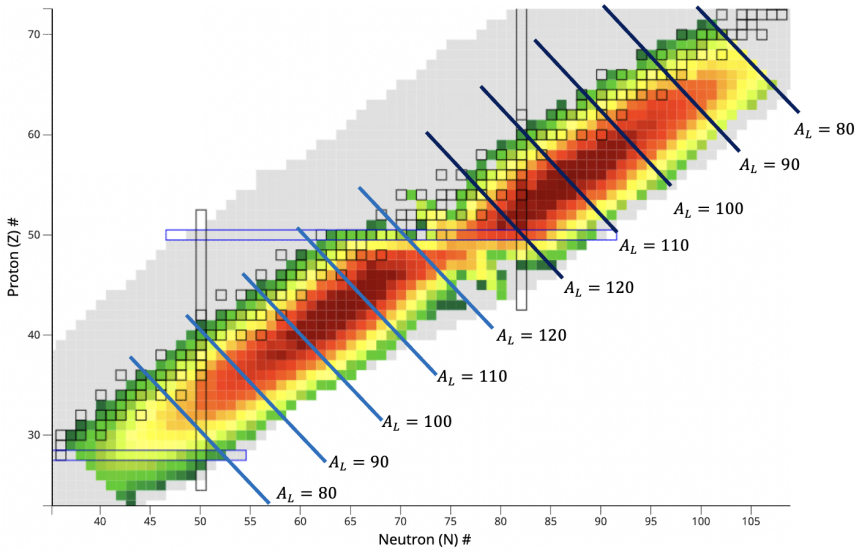

Figure 5.2: Fragment yields from ^{252}Cf, with indicated shell closures at $Z = 26, 50$ and $N = 50, 82$. Nuclei near these shell closures tend to be more spherical. We have superimposed on the base figure, taken from [62], the mass of the light fragment corresponding to that mass split.

source to understand the importance of incident neutrons.

Results obtained using both measurements of quadrupole band transitions in even-even nuclei [7], as well as populations of nuclear isomers [48], suggest that the magnitudes of the fragment angular momenta in fission are approximately uncorrelated. This puzzling result partially mirrors the uncorrelated energies of fission fragments as inferred from neutron multiplicities [38, 39].

The results of this dissertation, specifically the existence of a mass-dependent angular-momentum saturation, is in agreement with the results of past experiments. The data by Travar *et al.* [8] indicate a saturation when the fragment masses are not differentiated. The data by Wang *et al.* [51] show that the γ-ray multiplicity increases quickly with neutron multiplicity for fragments near ^{1}32Sn, and much more slowly for more probable fragments. Wang *et al.* also showed that the γ-ray multiplicity depends non-linearly on neutron multiplicity. This might be a consequence of the varying neutron separation energy, and thus correlations of statistical γ rays with neutrons. However, it cannot be excluded that E^*-J correlations

can sometimes be negative as well for one of the two fragments. More experimental studies are needed.

5.1.2 Direction

The polarization of the fragment angular momenta in a plane perpendicular to the fission axis has been inferred by several experiments [4, 5, 6, 63]. The degree of polarization is a challenging observable to measure, but the data from Hoffman *et al.* [4] indicate that the magnetic substates K of the fragment angular momenta along the fission axis are populated with $\langle K \rangle = 0$ and $\sigma(K)/J \approx 0.2$, although this is only a very crude approximation. This high level of polarization is consistent with our data. We have studied how the anisotropy of γ rays changes with fragment mass split. This study revealed that the angular momentum is most polarized for $A \sim 100 - 110$ and is less polarized for more asymmetric and symmetric fissions. This again reflects the effect that the sphericity of one of the two fragments can have on the polarization of angular momentum. We note also that while having a similar dependence on light-fragment mass, the polarization and the saturation have slightly different shapes. In fact, fragments remain polarized at higher masses, and start to depolarize only at the highest values of $A_L > 115$.

Measurements of the fragment angular distribution in photo-fission, as interpreted by Kadmensky *et al.* [64, 65] have shown that the fission axis does not align exactly along the symmetry axis of the initial target nucleus, but has a narrow distribution around it. This effect is due to a finite value of the orbital angular momentum, Λ between the two fragments, with $\Lambda \lesssim 30\ \hbar$. In fact, if the fission axis was restricted to coincide exactly with the initial symmetry axis, the uncertainty in the orbital angular momentum would grow, as dictated by the Heisenberg principle. The existence of a de-alignment implies that the orbital angular momentum between fragments needs to be large, since too small a value of Λ would imply an isotropy of fragment emission, which is not consistent with experiment.

The emission of charged particles in fission, such as is the case in ternary fission, does

not appear to influence the average angular momentum orientation [58].

As of today, there are no measurements of the correlations between fragment angular momenta directions. The closest measurement of this type was performed by Smith *et al.* [66], who measured the angular correlations between γ rays from partner fragments in the fission of ^{252}Cf(sf) and ^{248}Cm(sf). The measurements showed that the angular correlations of γ-rays from partner fragments is suppressed compared to the correlations between γ-rays emitted by the same fragment. The authors interpreted this result as a de-alignment of the fragment angular momenta, with significant projections along the fission axis. These type of measurements will further refine the role of the scission shape in determining the fragment angular momenta.

5.1.3 Summary

Theoretical models that attempt to describe the angular momenta of fission fragments requires an explanation of all of the preceding observations:

1. Fission fragments possess angular momentum. The average angular momentum of each fragment is 6-8 $\hbar$, and their distribution is wide, $\sigma(J) \sim 0.5\langle J \rangle$.

2. Deformed fragments have, on average, higher angular momentum than spherical fragments.

3. The total angular momentum of a system is not lowered when one of the fragments is spherical.

4. The total angular momentum of a system correlates positively with excitation energy. However, it saturates with excitation energy, and the saturated total angular momentum is approximately the same for all fragment pairs.

5. The energy required to saturate the total angular momentum is higher when one of the fragment is spherical.

6. The total angular momentum drops at the highest excitation energies or, conversely at the lowest TKE.

7. The angular momentum of the initial fissioning nucleus has little to no effect on the fragment angular momenta.

8. The magnitudes of the fragment angular momenta appear to be uncorrelated with one another.

9. The angular momentum is strongly polarized when both fragments are deformed, but can depolarize when one of the fragments is spherical.

10. The orbital angular momentum between the two fragments is large but finite, with $\Lambda \lesssim 20 - 30\hbar$.

In the above, when we say that one of the fragments is spherical, we mean the regions $A_L < 95$ and $A_L > 115$. These mass regions are the ones approaching the closed shell configurations at $A_L = 78$ and $A_H = 132$. In the following, we will simply say "for spherical-deformed (SD) fission events".

5.2 Critique of theoretical models

In this section, we delve into the current theoretical models of fission, explaining how the angular momentum of fission can be interpreted. The purpose of this section is also to bring to light some of the differences between the two most common ideas developed in fission theory, that either angular momentum originates as a result of excitation of di-nuclear modes, or it originates quantum mechanically, because of deformation of the fragments. These very different ideas have come to dominate the discussion on the fission fragment angular momentum, and both have their merits.

The first and most important question that a theoretical model of angular momentum needs to answer is how angular momentum can arise in the spontaneous fission of even-even

nuclei, *e.g*, ^{252}Cf. This special case highlights the existence of an internal mechanism that generates angular momentum in its sub-components, the fragments, while maintaining a 0 overall angular momentum, *i.e.*, the vectorial sum of the fragment angular momenta and the angular momentum of their relative motion.

5.2.1 Statistical di-nuclear excitation

The statistical di-nuclear excitation model posits that angular momentum is generated in fission due to the excitation of rotational modes as the fissioning system *descends* from the saddle point - the deformation point at which further deformation become energetically advantegeous - and into complete scission. The model we discuss here is due to Moretto *et al.* [67], but it is directly and indirectly based on other theoretical studies [68], drawn also from the analysis of heavy ion collisions [69].

A key idea of this model is that, at the moment of scission, the system resembles a diatomic molecule, with the two proto-fragments linked by a neck of nuclear matter. We call this the *di-nuclear* system. During the descent stage of the fission process, the di-nuclear system can undergo both rigid motion as well as intrinsic rotational motions of the two *proto-fragments*, *i.e.* the nuclear matter clusters that will eventually split into independent fragments. Heat, in the form of available excitation energy, can then flow to and excite these intrinsic and rigid rotational degrees of motion.

In the simple di-nuclear model, the distance between the two proto-fragments is taken to be fixed, and not a degree of motion. One can then distinguish between rigid rotation, where the entire di-nuclear system rotates, and intrinsic rotations, where the proto-fragmens are allowed to rotate about their internal axes.

Several classical rotational normal modes are possible: parallel modes, where the fragments rotate in the same sense, and their angular momentum is counteracted by an opposing rigid rotation of the di-nuclear systems; and anti-parallel modes, where the fragments' angular momenta point in opposite senses, cancelling each other and thus not requiring a

counteracting rigid rotation. These modes are further split depending on whether the angular momentum vectors are along the symmetry axis of the system, or in a plane perpendicular to it. The parallel modes are known as *tilting* and *wriggling* for these two cases, while the anti-parallel modes are known as *bending* and *twisting*. These modes are visually depicted in Fig. 5.3. For all of these normal modes, the total angular momentum is 0.

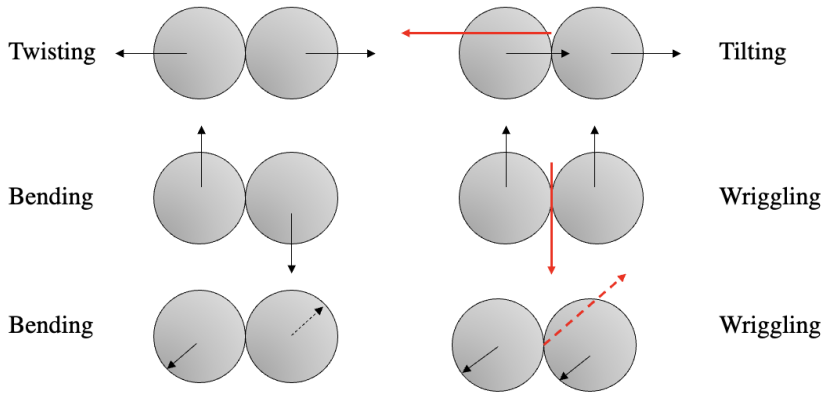

Figure 5.3: Rotational modes of the di-nuclear system. The black arrows indicate the fragment angular momenta, J_L and J_H, and the red arrow represents the orbital angular momentum Λ. Figure recreated on the basis of Ref. [70].

The energy transferred to these rotational modes must be available before scission, and thus from the total E^* we need to subtract the energy stored in the form of fragment deformations. Randrup [69] proposes that the excitation of the di-nuclear rotational modes is due to nucleon transfer between the two proto-fragments causing single particle excitation of angular momentum modes. Theoretical calculations of nucleon transfer show that nucleon transfer excites the wriggling modes most strongly, bending modes to a lesser extent, and twisting still less, while it cannot excite tilting directly. The single particle excitation can then relax into collective nuclear motion, giving nuclei their angular momenta.

The model has several important predictive successes, including the directional distribution of angular momenta [71], the independence of angular momenta [72], and the statistical dependence of angular momentum on excitation energy. Furthermore, the dependence of the

angular momentum on the available heat implies that super-deformed fission events should have little angular momentum. This prediction is somewhat confirmed by the drop in γ ray multiplicities at the highest values of E^*, which are predicted to be representative of super-deformed "cold" fission events. Our experimental results, as well as those of Gönnenwein *et al.* [61], have observed this behavior. Lastly, the di-nuclear model predicts that only a small fraction, $10-20\%$ of the angular momentum of the fissioning system goes to the fragments' angular momenta, also in agreement with our results. It has also been shown [72] that, with modified values of the moment of inertia chosen to best reproduce the quantum mechanical values, the di-nuclear model can also explain the angular momentum sawtooth distribution.

The statistical di-nuclear excitation model, in its current state, does not predict the depolarization of the fragment angular momenta in SD events. In fact, the lack of bending and twisting modes responsible for depolarization is nominally independent of the mass split. Recent investigations employing the statistical model have started to take a closer look at the role played by the bending and twisting modes [73].

It would be possible for the statistical model to predict the observed saturation if the energy not-available at scission was explicitly modeled. For example, the deformation energy would have a strong mass dependence, giving rise to the different E^*-J dependence. The complete saturation of the angular momentum can also be explained in terms of deformation energies, as shown by Gonnenwein *et al.*

In conclusion, we find the statistical di-nuclear excitation model to be quite successful in describing the observed results. The model has strong foundation in the theoretical models of nucleon transfer developed in heavy ion collisions. The model is classical in nature and it can be argued that the excitation of a few units of $\hbar$ should be treated in a quantum-mechanical setting. Nevertheless, we find that this classical explanation can be developed to explain more and more aspects of the fission process.

5.2.2 Quantum mechanical projections

The second major mechanism proposed for the angular momentum generation is based on quantum mechanics and projection methods. The overall idea is that the shapes of the nuclear wave functions contain all the information needed to determine their angular momenta. This procedure is analogous to the decomposition of a position wave function into momentum-representation wave functions.

In microscopic calculations [12, 74], the orbit functionals of the fissioning nucleus are simulated using time-dependent mean field approaches. An initial deformation, in both quadrupole and octupole coordinates, is enforced on the initial nucleus. Using phenomenological models of nuclear forces, the system is evolved in time. It was shown in these microscopic calculations that the dynamics of the fission process can, in fact, be reproduced. Due to the Coulomb repulsion, the deformations of the nucleus increase, eventually leading to the separation of the two fragments. These methods effectively simulate the intrinsic nucleonic density and, from the wave function, all observables can be determined.

The determination of the fragment angular momenta is determined by *angular momentum projection*. The distribution of angular momentum states is obtained by projecting the fragment wave functions on states of good angular momentum, *i.e.*, spherical harmonics. The deformation of the fragment wave function is thus the main source of fragment angular momenta. Deformation is also a source of intrinsic excitation energy in the fission fragments [75], thus explaining the appearance of $E^* - J$ correlations.

Because the computation is very expensive, and only microscopic times, $\sim 10^{-20}$ s, can be simulated, it is as yet impossible to simulate the long times associated with quantum tunnelling. Therefore, the starting conditions of the fission need to be chosen from states across the fission barrier, having a sufficient deformation as to proceed to fission, *i.e.*, at or past the saddle point. The projection methods have several important successes. They correctly predict the overall magnitude of angular momentum, as well as its relationship to fragment deformations. The angular momenta polarization is an assumption of these

calculations, rather than a conclusion. Furthermore, the prediction of angular momentum correlations by Bulgac *et al.* [12] is in good agreement with the experimental findings of this dissertation.

Microscopic methods are extremely powerful and no doubt represent the future of nuclear physics research. However, I argue here that in the present form they are not answering the fundamental question of fission angular momentum, namely how a system with no initial angular momentum splits into components with mutually cancelling angular moment, and predicting the values of the produced angular momenta. I argue this point because in choosing as initial conditions of the simulation a deformed state, and because the fragment angular momenta are calculated from their deformations, the simulation is biased.

A drawback of microscopic calculations based on mean field approaches is that the many-body wave function of the nucleus must be reduced, due to computational resources, to a one-body anti-symmetrized nucleon-density wave function. This procedure is warranted in systems with vanishing entanglements and correlations, but are not as accurate when these effects become significant. The mechanism of angular momentum generation we propose here is based on vibrational motion, a many-body collective motion that can be hard, but not impossible, to model in mean-field calculations.

An observable of interest predicted by these calculations is the relative angle between the fragments' angular momenta. The statistical di-nuclear model predicts that the angle between the two is almost uniform, while angular momentum projections of microscopic wave functions have yielded much more correlated distributions, almost resembling the angle between two random vectors in 3D space, instead of being constrained to the 2D plane assumed in the calculations [12]. It is challenging to separate the microscopic calculations from the angular momentum projection techniques, as both ingredients are needed in order to yield meaningful results. A critique we put forward to the projection techniques is that care must be taken in projecting the wave function to eigenbasis of non-commuting operators. For instance, in the work by Bulgac *et al.* [12, 74], the authors project both fragment angular

momenta as well as their relative orbital angular momentum. Because this latter quantity does not commute with the individual orientation of the fragment angular momenta, we expect the fragment to appear de-polarized, perhaps explaining the surprising predictions regarding the relative angle of the fragments' angular momenta. The magnitude of their angular momenta calculated should nevertheless not be affected by this procedure.

In conclusion, microscopic calculations of the nucleonic wave functions promise to be the most accurate methods of predicting nuclear observables, and their success is undeniable. On the other hand, while quantum mechanical in nature, the calculation is still constrained by the same constraints of other mean-field approaches. Mainly, the wave function calculated is the one-body wave function and highly collective behaviors such as rotations and vibrations will not be properly modeled, unless known *a priori*. Current computational technology also limits the accuracy with which we can simulate nuclear wave functions that abide by all conservation laws. Analytic solutions can help us better understand the scope of validity of numerical results.

5.3 Vibrational Model

In this section, we provide a possible theoretical explanation for the experimental observations of fragment angular momentum. The theoretical framework we present here is not complete, but is intended to provide a different perspective on the subject. We begin by presenting the overall idea: the longitudinal stretching of the di-nuclear system populates vibrational states which in turn couple to fragment angular momenta.

The model proposed here is quantum mechanical in nature, and explains the fission reaction in terms of an overlap of the ground-state wave function with collective phonon states. The angular momentum is conserved throughout the calculation because the intrinsic wave function of spontaneously fissioning nuclei is deformed, and thus already breaks rotational symmetry. Thus the spontaneous breaking of rotational symmetry by heavy actinides indicates the presence of angular momentum in the intrinsic frame of the nucleus. In the lab

frame, on the other hand, the wave function remains spherically symmetrical. Specifically, we propose that the symmetry-breaking ground state of spontaneously fissioning nuclei contains phonon-state components that proceed to fission. These phonons describe the collective motion of the nuclear shape. The coupling between phonon and intrinsic fragment motion gives rise to the observed fragment angular momentum.

The reason for proposing this model is the observed saturation of γ rays, and its indication of a saturation of angular momentum. We propose that the nucleus fissions into separate fragments when a large population of quadrupole phonons are generated. The angular momentum of these phonons is coupled to the fragment angular momenta, giving rise to the observed fragment J. However, large phonon populations are strongly suppressed in the ground-state wave function, and thus only a few different phonon states contribute significantly to the fission decay width. The treatment of fission as a large amplitude deformation and vibration process was already proposed by both N. Bohr [10], as well as A. Bohr and B. Mottelsson [76]. However, this approach was not pursued quantum mechanically, and the effects on fragment angular momenta were not considered, since the existence of the fragment angular momenta was not established until much later.

5.3.1 Path to fission

Let us follow the path of a spontaneously fissioning even-even nucleus, from ground state to complete fragment separation. Because of spontaneous symmetry breaking of the rotational symmetry, the ground state of deformed nuclei, such as ^{252}Cf, is written in terms of an intrinsic and rotational component. The nuclear system can be described by a Hamiltonian containing both intrinsic and rotational terms. For the illustrative purposes of this discussion, the intrinsic coordinate of interest is the amplitude of the elongation of the nucleus, in terms of the elongation parameter β. This amplitude describes the nuclear surface deformation associated with the coefficient of a spherical harmonic with $L = 2$ and $M = 0$. This type of deformation leads to the eventual separation of the two fragments. A potential barrier,

the *fission barrier*, stands between the nucleus ground state and a complete separation, as shown in Fig. 5.4.

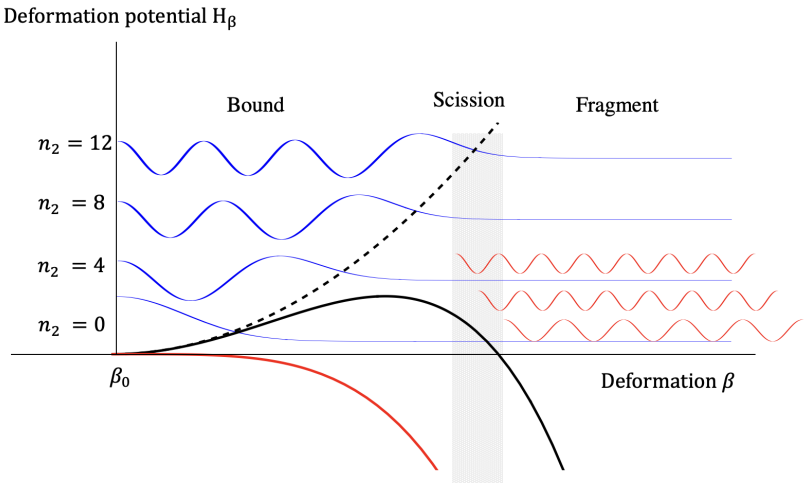

Figure 5.4: The deformation potential (black) can be approximated by a quadratic potential (dashed, black) and a perturbation which gives rise to the fission barrier (red). The unperturbed solutions are collective phonon states (blue), labeled by the phonon population n_2. The ground state of the perturbed Hamiltonian has non-vanishing overlap with phonon states. Specifically, the portion of the wave function on the fissioning side of the fission barrier, contains angular momentum carrying phonons.

We approximate the potential to the left of the fission barrier as an harmonic oscillator in the amplitude β, resulting in quantized bosons of vibrational motion, and a fission-barrier perturbation, giving rise to a finite height of the fission barrier and a negative potential at higher deformation.

$$\mathcal{H}_\beta = \kappa(\beta - \beta_0)^2 - F \ . \tag{5.1}$$

Here, β_0 is the ground-state stable deformation of the fissioning nucleus and F is a perturbation with a quartic dependence on the deformations, such that it dominates at high amplitudes.

We write the ground state of the nucleus as

$$|\Psi\rangle = |n_2\rangle \;\; \mathcal{D}^I_{M,K}(\mathbf{\Omega}) = |\tilde{0}\rangle \;\; \mathcal{D}^0_{0,0}(\mathbf{\Omega}) \;, \tag{5.2}$$

where the state of the nucleus is separated into an intrinsic component and a rotational component. We specify the intrinsic component using the basis of phonon states, fully specified by phonon population number n_2. Importantly, the ground state is not in a pure phonon state because of the perturbation F. The ground state is in a superposition of many pure phonon states, *i.e.*, states of the unperturbed Hamiltonian. To first approximation,

$$|\tilde{0}\rangle = |0\rangle + \sum_{m=1} \frac{\langle m| \, F \, |0\rangle}{E_m - E_0} \, |m\rangle \;\; , \tag{5.3}$$

where E_m is the energy of the m^{th} vibrational state.

Thus, the deformation amplitude remains small and centered around its ground-state deformation, but it possesses non-zero amplitudes, or overlaps, with higher vibrational states with large deformation amplitudes. The rotational component of the ground state is given by the Wigner $\mathcal{D}$ function, which for the ground state is spherically symmetric, since even-even nuclei have angular momentum and parity $I^\pi = 0^+$. The coordinates $\mathbf{\Omega}$ are the angles specifying the orientation of the intrinsic coordinate system with respect to the lab frame. Many more quantum numbers would be needed to specify the intrinsic state, but we focus here on the phonon state only.

Let us then hypothesize that there exists a *scission state* with s quadrupole phonons, that has a significant overlap with states on the other side of the fission barrier. We express this state as

$$|\psi_s\rangle = |s\rangle \, \mathcal{D}^0_{0,0}(\mathbf{\Omega}) \;, \tag{5.4}$$

with phonon population of $n_2 = s$. To explain saturation, we hypothesize that there are only a small number of, or even just a singular, states $|\psi_s\rangle$ that have a large overlap with

the ground state. For this to be the case, the overlap in Eq. (5.3) must decrease with vibrational states faster than the increase in the overlap of the vibrational state with scissioning configurations, *i.e.* states on the other side of the barrier. For simplicity, we shall consider a single scission state, as the extension to several is trivial.

The longitudinal phonons, having a defined orientation with respect to the nucleus, do not have a defined sum of their angular momentum. Specifically, we find that the intrinsic scissioning shape is in a superposition of total angular momentum Λ states. The angular momentum Λ has vanishing expectation values in every direction, but it has non-vanishing fluctuations in the plane perpendicular to the vibrational axis. The angular momentum of the transverse component in a state $|s\rangle$ is $\sqrt{\langle\Lambda^2\rangle} \sim n_\lambda\lambda(1+\lambda)$, proportional to the sum in quadrature of the phonon angular momenta $\lambda = 2$. The existence of angular momentum in the intrinsic shape is not in violation of the conservation of angular momentum. In fact, the wave function remains spherically symmetric and thus of angular momentum 0, through its product with the rotational wave function, as shown in Eq. (5.4).

We express the scission state in terms of states of defined total angular momentum, expressed in angular coordinates for clarity,

$$\psi_s = \mathcal{D}^0_{0,0}(\boldsymbol{\Omega}) \times \sum_{\Lambda=0}^{2s} c_\Lambda Y_0^\Lambda(\boldsymbol{\omega}) \ , \tag{5.5}$$

where the direction $\boldsymbol{\omega}$ specifies the orientation of the total vibration with respect to the symmetry axis, and c_Λ is a geometric coefficient that is easily determined [76]. Due to conservation of parity, only even Λ states can contribute to the sum. The larger the value of Λ, the more the intrinsic wave function will be narrowly pointing in the z direction of the intrinsic frame, *i.e.*, the symmetry axis of ground state ^{252}Cf. At the other extreme, $\Lambda = 0$ represent vibrations that are isotropic with respect to the intrinsic symmetry axis of the nucleus.

The vibrating scission state will have overlaps with free fragment states, as shown in

Fig. 5.4. Therefore, the scission interaction in the intrinsic Hamiltonian has the form

$$\mathcal{H}_{\text{scis}} = \epsilon(J_L, J_H, \beta) \times |J_L \boldsymbol{k}\rangle \, |J_H \boldsymbol{k}\rangle \, \langle s| \tag{5.6}$$

Thus, the scission interaction Hamiltonian can evolve the scission states into states of fragment angular momenta. However, not all states are populated equally. First of all, we must consider the angular momentum. For any Λ in the series expansion of s, we must also require that the fragment angular momenta sum vectorially to the same quantity. The individual light and heavy fragment angular momenta, J_L and J_H respectively, must obey

$$J_L + J_H \geq \Lambda \geq |J_L - J_H| \tag{5.7}$$

We also point out that the quantity $J_L + J_H$ is what we referred to as the total angular momentum J in this dissertation. The inequality in (5.7) puts a lower constraint on J, but the two angular momenta, J_L and J_H can also be very large, and subsequently the total angular momentum can also be large, as long as their difference satisfies the inequality.

Energy considerations and statistical considerations then allow us to further constrain the value of the angular momentum most strongly populated in fission. Energy considerations apply to the total angular momentum J. The configuration with the lowest amount of rotational energy is the one with $J = \Lambda$. This is the configuration in which both fragments are approximately parallel to one another, and both are approximately perpendicular to the fission axis. A strong population of this state can thus explain the polarization of fragment angular momenta. States with $J > \Lambda$ would be energy suppressed, but not unpopulated, and would result in de-polarizations of the fragment angular momenta. We also expect that for these states the fragment magnetic substates to be entangled.

The statistical population of allowed states that satisfy the constraint of Eq. (5.7) implies an anti-correlation in the fragment angular momenta. However, because the scission state $|\psi_s\rangle$ is a superposition of Λ, the variations in Λ result in positive correlations between J_L

and J_H. This is similar to how splitting randomly a cake in two slices results in negative correlations between the sizes of the slices, but increasing the size of the cake overall increases both slices, thus introducing positive correlations. Therefore, we argue that the absence of correlations between fragment angular momenta is due to a cancellation of effects, an example of Simpson's paradox [77].

Angular momentum is still conserved in the entire process, in fact, the angular momenta discussed up to here are generated in the intrinsic coordinate frame, relative to the direction $\boldsymbol{\omega}$, whereas the angular momentum that needs to be identically 0 is the one with respect to the coordinates $\boldsymbol{\Omega}$.

Finally, we explain the observed behavior of the fragment angular momenta using this model. We have already explained their lack of correlations as well as the average angular momentum polarization. One way angular momentum can depolarize is if fragment states with $J > \Lambda$ are populated more significantly. This can be the case if, for example, SD configurations have more available energy, such that the distributions in J for a given Λ include more terms than the lowest energy one. Another explanation of the depolarization can be found including intermediary transitions first to a di-nuclear state followed by a state of separated fragments. At this stage, a bending mode interaction of the type

$$\mathcal{H}_{\text{bend}} \propto \boldsymbol{J_L} \cdot \boldsymbol{J_H} \tag{5.8}$$

can introduce non-longitudinal components to the angular momentum.

The explanation of the saturation is perhaps the most interesting, and also the one that motivated us to develop this illustrative model. The saturation is a consequence of the fact that there are only a few vibrational scission states $|s\rangle$ that decay to fragments. Therefore, the distribution of Λ is fixed to be within only a few states. On the other hand, the total kinetic energy, and hence the excitation energy, are related to the amplitude β at scission, because of its relations to the inter-nuclear distance and the repulsive Coulomb potential. The same scissioning state ψ_s gives rise to a probability amplitude over a range of β, while

having the same distribution of Λ. Thus, the relative population of different vibrational scission states gives rise to the E^*-J correlations, whereas when the highest scission state is populated, the angular momentum saturates.

The mechanism proposed here is only illustrative and more theoretical work will need to be performed in order to assess its validity. Specifically, the model predicts that states with a large number of quadrupole phonons should be populated $n_2 \sim 10 - 15$, but experimental observations of β-vibrational states are still not fully developed. The crude approximations used in describing the model would have to be checked against rigorous numerical calculations, and ultimately microscopic computations. Nevertheless, the principle outlined here could prove to be the source, or most likely one of the sources, of explaining the role of angular momentum in fission.

An interesting prediction of this model is that in induced fission it might be possible to populate higher vibrational states, thus increasing the threshold for saturation. We have seen in ^{239}Pu(n,f) that the E^*-J correlations remain linear longer than what might be expected from the ^{252}Cf(sf) data, but there are too many differences to compare these yields directly.

The model produces a simple prediction for an experimental observable that can be used to assess its validity. Specifically, the angle between the angular momenta of the two fragments is predicted to be small on average. If experimentally this angle were to be significantly different, there is little hope for this model's validity. Experiments aiming to constrain this angle are underway. Interestingly, this observable also discriminates between the di-nuclear excitation model and the models based on angular momentum projection of the fragments' wave functions.

CHAPTER VI

Conclusion

Throughout the chapters of this dissertation, we have delved deeper and deeper into the physics of fragment angular momentum, beginning with an experiment where the only observables were neutrons and γ rays emitted from a fissioning sample, and ending with a model for the generation of angular momentum due to vibrational nuclear motion.

The biggest conclusion of this dissertation is that angular momentum has a non-trivial energy dependence, more complicated then what phenomenological and theoretical models can currently predict. Specifically, the main observables contributed from this dissertation are the angular momentum saturation and its depolarization, giving rise respectively to an approximately constant γ-ray yield at high excitation energies, and a tendency to become isotropic for fragment splits near $A_H = 132$ as well as $A_L = 78$. The evidence presented in Chapter III indicates that the angular momentum does not saturate as quickly in ^{239}Pu(n,f) as it does in ^{252}Cf(sf). However, the different fragment yields of the two reactions complicate the interpretation of these results.

Not much can be done to significantly improve the results of our event-by-event analysis, presented in Chapter II, without the addition of fragment or beam variables. The analysis we have shown is complete in the n-γ variables. The analysis establishes that neutron and γ-ray emissions are correlated at a level of approximately 3-7%, *i.e.*, coincident n-γ measurements can deviate by this amount from the singles rates. It will be interesting to repeat the analysis

on other isotopes and reactions. We have analyzed data from ^{242}Pu(sf) that confirmed the finding of this dissertation. However, the statistics were too low to learn anything new from this reaction.

Beam experiments on fission are extremely important for our understanding of the fission reactions, and they also occupy a privileged role in its future. Ever since humans have discovered how to "split the atom", we have learned much more about how to control long fission chains and reliably produce energy. However, the method by which we split nuclei remains rudimentary, striking it with enough energy and hoping the nucleus will find its way to fission. This procedure is akin to breaking a lock, instead of trying to pick it. It will be important in the future to conduct more beam experiments of the kind shown in Chapter III, but utilizing different types of beam particles and targets. Especially interesting is the use of ions, which will allow us to understand the unknown fission mechanisms in terms of known electromagnetic control variables.

Lastly, experiments involving the measurement of fragments have a rich history. The fragment-correlated analysis we have shown in Chapter IV barely scratches the surface of what can be done when fragments and n-γ radiation are measured in coincidence. Nonetheless, even the simple analysis we have applied to these data already yielded some of the most interesting results in this dissertation. More advanced analysis of these same data will need to focus on the emission of particles in the fragment reference frame, with a specific focus on the angular correlations between emitted particles. Most importantly, improvements to the fragment-correlated analysis will be in the form of improvements to the hardware of the fission chamber and the detectors used. Especially promising and imminent is an experiment combining the TFGIC with the Gammasphere high-resolution γ-ray spectrometer at Argonne National Laboratory.

A subtle challenge in scientific endeavors, especially when applied to complex systems, is clearly defining the scope and objectives of the research. Without these boundaries and goals, the research work risks becoming its own objective. There is a risk that fission re-

search will find its motivation in its own inertia, and important and insightful results will be buried under the weight of aimless research. The cure to this illness, in my opinion, is found in experimentally-grounded theoretical models. Specifically, theories should dictate where experiments go, and it should be the goal of experiments to validate or falsify theoretical models. For this to happen, theoretical models will need to produce falsifiable predictions accessible to current and future experiments. The predictions of the theoretical model developed in Chapter V are testable, and the role of this mechanism in the generation of angular momentum can be experimentally assessed.

BIBLIOGRAPHY

BIBLIOGRAPHY

[1] J. R. Grover. Shell-model calculations of the lowest-energy nuclear excited states of very high angular momentum. *Phys. Rev.*, 157:832–847, 1967.

[2] T. D. Thomas and J. R. Grover. Angular momentum effects in the gamma-ray de-excitation of fission fragments. *Phys. Rev.*, 159:980–984, 1967.

[3] H. Nifenecker, C. Signarbieux, M. Ribrag, J. Poitou, and J. Matuszek. Gamma-neutron competition in the de-excitation mechanism of the fission fragments of ^{252}Cf. *Nucl. Phys. A*, 189(2):285 – 304, 1972.

[4] M. M. Hoffman. Directional correlation of fission fragments and prompt gamma rays associated with thermal neutron fission. *Phys. Rev.*, 133:B714–B723, 1964.

[5] J. B. Wilhelmy, E. Cheifetz, R. C. Jared, S. G. Thompson, H. R. Bowman, and J. O. Rasmussen. Angular momentum of primary products formed in the spontaneous fission of ^{252}Cf. *Phys. Rev. C*, 5:2041–2060, 1972.

[6] K. Skarsvåg. Differential angular distribution of prompt gamma rays from spontaneous fission of ^{252}Cf. *Phys. Rev. C*, 22:638–650, 1980.

[7] J. N. Wilson, D. Thisse, M. Lebois, N. Jovančević, D. Gjestvang, R. Canavan, M. Rudigier, D. Étasse, R-B. Gerst, L. Gaudefroy, E. Adamska, P. Adsley, A. Algora, M. Babo, K. Belvedere, J. Benito, G. Benzoni, A. Blazhev, A. Boso, S. Bottoni, M. Bunce, R. Chakma, N. Cieplicka-Oryńczak, S. Courtin, M. L. Cortés, P. Davies, C. Delafosse, M. Fallot, B. Fornal, L. Fraile, A. Gottardo, V. Guadilla, G. Häfner, K. Hauschild, M. Heine, C. Henrich, I. Homm, F. Ibrahim, Ł W. Iskra, P. Ivanov, S. Jazrawi, A. Korgul, P. Koseoglou, T. Kröll, T. Kurtukian-Nieto, L. Le Meur, S. Leoni, J. Ljungvall, A. Lopez-Martens, R. Lozeva, I. Matea, K. Miernik, J. Nemer, S. Oberstedt, W. Paulsen, M. Piersa, Y. Popovitch, C. Porzio, L. Qi, D. Ralet, P. H. Regan, K. Rezynkina, V. Sánchez-Tembleque, S. Siem, C. Schmitt, P.-A. Söderström, C. Sürder, G. Tocabens, V. Vedia, D. Verney, N. Warr, B. Wasilewska, J. Wiederhold, M. Yavahchova, F. Zeiser, and S. Ziliani. Angular momentum generation in nuclear fission. *Nature*, 590(7847):566–570, 2021.

[8] M. Travar, V. Piau, A. Göök, O. Litaize, J. Nikolov, A. Oberstedt, S. Oberstedt, J. Enders, M. Peck, W. Geerts, and M. Vidali. Experimental information on mass- and tke-dependence of the prompt fission gamma-ray multiplicity. *Phys. Lett. B*, 817:136293, 2021.

[9] F. Gonnenwein, I. Tsekhanovic, and V. Rubchenya. Angular momenta of near-spherical fission fragments. *Int. J. Mod. Phys. E*, 16:410–424, 2007.

[10] N. Bohr and J. A. Wheeler. The mechanism of nuclear fission. *Phys. Rev.*, 56(5):426–450, 1939.

[11] U. Brosa and A. Grossmann, S.and Müller. Nuclear scission. *Phys. Rep.*, 197(4):167 – 262, 1990.

[12] A. Bulgac, I. Abdurrahman, K. Godbey, and I. Stetcu. Fragment intrinsic spins and fragments' relative orbital angular momentum in nuclear fission. *Phys. Rev. Lett.*, 128:022501, 2022.

[13] S. Marin, M. S. Okar, E. P. Sansevero, I. E. Hernandez, C. A. Ballard, R. Vogt, J. Randrup, P. Talou, A. E. Lovell, I. Stetcu, O. Serot, O. Litaize, A. Chebboubi, S. D. Clarke, V. A. Protopopescu, and S. A. Pozzi. Structure in the event-by-event energy-dependent neutron-γ multiplicity correlations in ^{252}Cf(sf). *Phys. Rev. C*, 104:024602, 2021.

[14] R. Schmid-Fabian. *Investigation of the Spontaneous Fission of Cf-252 at the Heidelberg-Darmstadt Crystal-Ball-Spectrometer*. PhD thesis, University of Heidelberg, 1988.

[15] A. Chebboubi, G. Kessedjian, O. Litaize, O. Serot, H. Faust, D. Bernard, A. Blanc, U. Köster, O. Méplan, P. Mutti, and C. Sage. Kinetic energy dependence of fission fragment isomeric ratios for spherical nuclei ^{132}Sn. *Phys. Lett. B*, 775:190 – 195, 2017.

[16] K. J. Kelly, M. Devlin, J. M. O'Donnell, J. A. Gomez, D. Neudecker, R. C. Haight, T. N. Taddeucci, S. M. Mosby, H. Y. Lee, C. Y. Wu, R. Henderson, P. Talou, T. Kawano, A. E. Lovell, M. C. White, J. L. Ullmann, N. Fotiades, J. Henderson, and M. Q. Buckner. Measurement of the ^{239}Pu(n, f) prompt fission neutron spectrum from 10 keV to 10 MeV induced by neutrons of energy 1–20 MeV. *Phys. Rev. C*, 102:034615, 2020.

[17] M. J. Marcath, Robert C. Haight, Ramona Vogt, Matthew Devlin, Patrick Talou, Ionel Stetcu, Jørgen Randrup, Patricia F. Schuster, Shaun D. Clarke, and Sara A. Pozzi. Measured and simulated ^{252}Cf(sf) prompt neutron-photon competition. *Phys. Rev. C*, 97:044622, 2018.

[18] R. B. Oberer. Maximum alpha to minimum fission pulse amplitude for a parallel-plate and hemispherical Cf-252 ion-chamber instrumented neutron source. 2000.

[19] S. A. Pozzi, E. Padovani, and M. Marseguerra. MCNP-PoliMi: a monte-carlo code for correlation measurements. *Nucl. Instr. Meth. A.*, 513(3):550 – 558, 2003.

[20] J. B. Birks. *The Theory and Practice of Scintillation Counting*, volume 148. Elsevier, 1964.

[21] A. Oberstedt, R. Billnert, F.-J. Hambsch, and S. Oberstedt. Impact of low-energy photons on the characteristics of prompt fission γ-ray spectra. *Phys. Rev. C*, 92:014618, 2015.

[22] S. Marin, V. A. Protopopescu, R. Vogt, M. J. Marcath, M. S. Okar, M. Y. Hua, P. Talou, P. F. Schuster, S. D. Clarke, and S. A. Pozzi. Event-by-event neutron–photon multiplicity correlations in ^{252}Cf(sf). *Nucl. Instr. Meth. A*, 968:163907, 2020.

[23] S. Marin, E. P. Sansevero, M. S. Okar, I. E. Hernandez, R. Vogt, J. Randrup, S. D. Clarke, V. A. Protopopescu, and S. A. Pozzi. Directional dependence of the event-by-event neutron-γ multiplicity correlations in ^{252}Cf(sf). *Phys. Rev. C*, 105:054609, 2022.

[24] H.A. Tolhoek and J.A.M. Cox. Angular distribution and polarization of gamma radiation emitted by oriented nuclei. *Physica*, 19(1):101–119, 1953.

[25] P. Glässel, R. Schmid-Fabian, D. Schwalm, D. Habs, and H.U.v. Helmolt. ^{252}Cf fission revisited — new insights into the fission process. *Nuclear Physics A*, 502:315 – 324, 1989.

[26] D. L. Bleuel, L. A. Bernstein, J. T. Burke, J. Gibelin, M. D. Heffner, J. Mintz, E. B. Norman, L. Phair, N. D. Scielzo, S. A. Sheets, N. J. Snyderman, M. A. Stoyer, and M. Wiedeking. Gamma-ray multiplicity measurement of the spontaneous fission of 252Cf in a segmented HPGe/BGO detector array. *Nucl. Instr. Meth. A*, 624(3):691–698, 2010.

[27] V. Metag, D. Habs, K. Helmer, U. v. Helmolt, H. W. Heyng, B. Kolb, D. Pelte, D. Schwalm, W. Hennerici, H. J. Hennrich, G. Himmele, E. Jaeschke, R. Repnow, W. Wahl, R. S. Simon, and R. Albrecht. The Darmstadt-Heidelberg-Crystal-Ball. In W. von Oertzen, editor, *Detectors in Heavy-Ion Reactions*, pages 163–178. Springer Berlin Heidelberg, Berlin, Heidelberg, 1983.

[28] S. R. Lesher, L. Phair, L. A. Bernstein, D. L. Bleuel, J. T. Burke, J. A. Church, P. Fallon, J. Gibelin, N. D. Scielzo, and M. Wiedeking. STARS/LiBerACE: Segmented silicon and high-purity germanium detector arrays for low-energy nuclear reaction and structure studies. *Nucl. Instr. Meth. A*, 621(1-3):286–291, 2010.

[29] P. Talou, I. Stetcu, P. Jaffke, M. E. Rising, A. E. Lovell, and T. Kawano. Fission fragment decay simulations with the CGMF code. *Comp. Phys. Comm.*, 269, 7 2021.

[30] P. Talou, R. Vogt, J. Randrup, M. E. Rising, S. A. Pozzi, J. Verbeke, M. T. Andrews, S. D. Clarke, P. Jaffke, M. Jandel, T. Kawano, M. J. Marcath, K. Meierbachtol, L. Nakae, G. Rusev, A. Sood, I. Stetcu, and C. Walker. Correlated prompt fission data in transport simulations. *Europ. Phys. J. A.*, 54(1):9, 2018.

[31] O. Litaize and O. Serot. Investigation of phenomenological models for the monte carlo simulation of the prompt fission neutron and γ emission. *Phys. Rev. C*, 82:054616, 2010.

[32] O. Litaize, O. Serot, and L. Berge. Fission modelling with FIFRELIN. *Europ. Phys. J. A*, 51(12):177, 2015.

[33] L. Thulliez, O. Litaize, O. Serot, and A. Chebboubi. Neutron and γ multiplicities as a function of incident neutron energy for the ^{237}Np(n,f) reaction. *Phys. Rev. C*, 100:044616, 2019.

[34] J. Randrup and R. Vogt. Calculation of fission observables through event-by-event simulation. *Phys. Rev. C*, 80:024601, 2009.

[35] J. M. Verbeke, J. Randrup, and R. Vogt. Fission reaction event yield algorithm freya 2.0.2. *Comp. Phys. Comm.*, 222:263 – 266, 2018.

[36] L. Thulliez, O. Litaize, and O. Serot. Sensitivity studies of spin cut-off models on fission fragment observables. *EPJ Web Conf.*, 111:10003, 2016.

[37] A. Chalil, T. Materna, O. Litaize, A. Chebboubi, and F. Gunsing. Monte carlo simulations of gamma-ray -directional correlations and their application on fifrelin cascades. *Europ. Phys. J. A*, 58:1–10, 2022.

[38] C. Signarbieux, J. Poitou, M. Ribrag, and J. Matuszek. Correlation entre les energies d'excitation des deux fragments complementaires dans la fission spontanee de ^{252}Cf. *Phys. Lett. B*, 39(4):503 – 505, 1972.

[39] A. Gavron and Z. Fraenkel. Measurement of the variance of the number of neutrons emitted in fission of ^{252}Cf as a function of the fragment mass and total kinetic energy. *Phys. Rev. Lett.*, 27:1148–1151, 1971.

[40] N. Giha, S. Marin, J. A. Baker, I. E. Hernandez, K. J. Kelly, M. Devlin, J. M. O'Donnell, R. Vogt, J. Randrup, P. Talou, I. Stetcu, A. E. Lovell, O. Serot, O. Litaize, A. Chebboubi, C. Y. Wu, S. D. Clarke, and S. A. Pozzi. Correlations between γ-ray multiplicity and compound nucleus excitation energy in ^{239}Pu(n, f). *https://arxiv.org/abs/2207.02743*, 2022.

[41] C. Y. Wu, R. A. Henderson, R. C. Haight, H. Y. Lee, T. N. Taddeucci, B. Bucher, A. Chyzh, M. Devlin, N. Fotiades, E. Kwan, J. M. O'Donnell, B. A. Perdue, and J. L. Ullmann. A multiple parallel-plate avalanche counter for fission-fragment detection. *Nucl. Instr. Meth. A*, 794:76–79, 2015.

[42] D. A. Brown, M. B. Chadwick, R. Capote, A. C. Kahler, A. Trkov, M. W. Herman, A. A. Sonzogni, Y. Danon, A. D. Carlson, M. Dunn, D. L. Smith, G. M. Hale, G. Arbanas, R. Arcilla, C. R. Bates, B. Beck, B. Becker, F. Brown, R. J. Casperson, J. Conlin, D. E. Cullen, M.-A. Descalle, R. Firestone, T. Gaines, K. H. Guber, A. I. Hawari, J. Holmes, T. D. Johnson, T. Kawano, B. C. Kiedrowski, A. J. Koning, S. Kopecky, L. Leal, J.P. Lestone, C. Lubitz, J. I. Márquez Damián, C. M. Mattoon, E. A. McCutchan, S. Mughabghab, P. Navratil, D. Neudecker, G. P. A. Nobre, G. Noguere, M. Paris, M. T. Pigni, A. J. Plompen, B. Pritychenko, V. G. Pronyaev, D. Roubtsov, D. Rochman, P. Romano, P. Schillebeeckx, S. Simakov, M. Sin, I. Sirakov, B. Sleaford, V. Sobes, E. S. Soukhovitskii, I. Stetcu, P. Talou, I. Thompson, S. van der Marck, L. Welser-Sherrill, D. Wiarda, M. White, J.L. Wormald, R. Q. Wright, M. Zerkle, G. Zerovnik, and Y. Zhu. ENDF/B-VIII.0: The 8th major release of the nuclear reaction data library with CIELO-project cross sections, new standards and thermal scattering data. *Nucl. Data Sheets*, 148:1–142, 2018.

[43] J. Fréhaut, A. Bertin, and R. Bois. Measurement of $\bar{\nu}$ and $\bar{E}_\gamma$ in the fission of ^{232}Th, ^{235}U and ^{237}Np induced by neutrons of energy between 1 and 15 MeV. In K. H. Böckhoff, editor, *Nuclear Data for Science and Technology*, pages 78–81, Dordrecht, 1983.

[44] A. Gatera, T. Belgya, W. Geerts, A. Göök, F.-J. Hambsch, M. Lebois, B. Maróti, A. Moens, A. Oberstedt, S. Oberstedt, F. Postelt, L. Qi, L. Szentmiklósi, G. Sibbens, D. Vanleeuw, M. Vidali, and F. Zeiser. Prompt-fission γ-ray spectral characteristics from ^{239}Pu(n_{th}, f). *Phys. Rev. C*, 95:064609, 2017.

[45] L. Qi, M. Lebois, J. N. Wilson, A. Chatillon, S. Courtin, G. Fruet, G. Georgiev, D. G. Jenkins, B. Laurent, L. Le Meur, A. Maj, P. Marini, I. Matea, L. Morris, V. Nanal, P. Napiorkowski, A. Oberstedt, S. Oberstedt, C. Schmitt, O. Serot, M. Stanoiu, and B. Wasilewska. Statistical study of the prompt-fission γ-ray spectrum for ^{238}U(n, f) in the fast-neutron region. *Phys. Rev. C*, 98:014612, 2018.

[46] J.-M. Laborie, R. Billnert, G. Bélier, A. Oberstedt, S. Oberstedt, and J. Taieb. First experimental prompt γ-ray spectra in fast-neutron-induced fission of ^{238}U. *Phys. Rev. C*, 98:054604, 2018.

[47] S. J. Rose, F. Zeiser, J. N. Wilson, A. Oberstedt, S. Oberstedt, S. Siem, G. M. Tveten, L. A. Bernstein, D. L. Bleuel, J. A. Brown, L. Crespo Campo, F. Giacoppo, A. Görgen, M. Guttormsen, K. Hadyńska, A. Hafreager, T. W. Hagen, M. Klintefjord, T. A. Laplace, A. C. Larsen, T. Renstrøm, E. Sahin, C. Schmitt, T. G. Tornyi, and M. Wiedeking. Energy dependence of the prompt γ-ray emission from the (d, p)-induced fission of ^{234}U* and ^{240}Pu*. *Phys. Rev. C*, 96:014601, 2017.

[48] D. Gjestvang, S. Siem, F. Zeiser, J. Randrup, R. Vogt, J. N. Wilson, F. Bello-Garrote, L. A. Bernstein, D. L. Bleuel, M. Guttormsen, A. Görgen, A. C. Larsen, K. L. Malatji, E. F. Matthews, A. Oberstedt, S. Oberstedt, T. Tornyi, G. M. Tveten, and A. S. Voyles. Excitation energy dependence of prompt fission γ-ray emission from ^{241}Pu*. *Phys. Rev. C*, 103:034609, 2021.

[49] K. Meierbachtol, F. Tovesson, D. L. Duke, V. Geppert-Kleinrath, B. Manning, R. Meharchand, S. Mosby, and D. Shields. Total kinetic energy release in ^{239}Pu(n, f) post-neutron emission from 0.5 to 50 MeV incident neutron energy. *Phys. Rev. C*, 94:034611, 2016.

[50] A. Göök, F.-J. Hambsch, and M. Vidali. Prompt neutron multiplicity in correlation with fragments from spontaneous fission of ^{252}Cf. *Phys. Rev. C*, 90(6):064611, 2014.

[51] T. Wang, G. Li, L. Zhu, Q. Meng, L. Wang, H. Han, W. Zhang, H. Xia, L. Hou, R. Vogt, and J. Randrup. Correlations of neutron multiplicity and γ -ray multiplicity with fragment mass and total kinetic energy in spontaneous fission of ^{252}Cf. *Phys. Rev. C*, 93(1):1–14, 2016.

[52] E. Nardi, A. Gavron, and Z. Fraenkel. Total energy associated with prompt γ-ray emission in the spontaneous fission of ^{252}Cf. *Phys. Rev. C*, 8:2293–2297, 1973.

[53] D. L. Duke. Fission fragment mass distributions and total kinetic energy release of 235-uranium and 238-uranium in neutron-induced fission at intermediate and fast neutron energies, 2015. Ph.D. dissertation.

[54] C. Budtz-Jørgensen, H.-H. Knitter, Ch. Straede, F.-J. Hambsch, and R. Vogt. A twin ionization chamber for fission fragment detection. *Nuclear Instruments and Methods in Physics Research Section A: Accelerators, Spectrometers, Detectors and Associated Equipment*, 258(2):209–220, 1987.

[55] L. Gaudefroy, T. Roger, J. Pancin, C. Spitaels, J. Aupiais, and J. Mottier. A twin frisch-grid ionization chamber as a selective detector for the delayed gamma-spectroscopy of fission fragments. *Nuclear Instruments and Methods in Physics Research Section A: Accelerators, Spectrometers, Detectors and Associated Equipment*, 855:133–139, 2017.

[56] S. Mosby, F. Tovesson, A. Couture, D. L. Duke, V. Kleinrath, R. Meharchand, K. Meierbachtol, J. M. ODonnell, B. Perdue, D. Richman, and D. Shields. A fission fragment detector for correlated fission output studies. *Nuclear Instruments and Methods in Physics Research Section A: Accelerators, Spectrometers, Detectors and Associated Equipment*, 757:75–81, 2014.

[57] A. C. Wahl. Systematics of nuclear charge distribution in fission the Z_P model. *J. of Rad. Chem. 1980 55:1*, 55:111–123, 1980.

[58] Y. N. Kopach, P. Singer, M. Mutterer, M. Klemens, A. Hotzel, D. Schwalm, P. Thirolf, M. Hesse, and F. Gönnenwein. Angular anisotropy of prompt γ rays and fragment spin alignment in binary and light-charged-particle-accompanied spontaneous fission of ^{252}Cf. *Phys. Rev. Lett.*, 82:303–306, 1999.

[59] A. Oberstedt, R. Billnert, A. Gatera, A. Göök, and S. Oberstedt. Prompt fission γ rays and their angular distributions. *EPJ Web Conf.*, 193:03005, 2018.

[60] N. Schunck and D. Regnier. Theory of nuclear fission. *Progr. Part. & Nucl. Phys*, 125:103963, 2022.

[61] F. Gönnenwein, M. Mutterer, and Y. Kopatch. Ternary and quaternary fission. *Europhysics News*, 36(1):11–15, 2005.

[62] Nudat 3, https://www.nndc.bnl.gov/nudat3/. Accessed in June 2022.

[63] G. V. Val'ski, B. M. Aleksandrov, I. A. Baranov, A. S. Krivokatskii, G. A. Petrov, and Yu S. Pleva. Some characteristics of the gamma radiation accompanying fission of ^{252}Cf. *Sov. J. of Nucl. Phys.*, 10(2):137–141, 1969.

[64] S. G. Kadmensky and L. V. Rodionova. Angular distributions of fragments originating from the spontaneous fission of oriented nuclei and problem of the conservation of the spin projection onto the symmetry axis of a fissile nucleus. *Phys. At. Nucl.*, 68:1433–1442, 2005.

[65] S. G. Kadmensky. The quantum and thermodynamical characteristics of fission taking into account adiabatic and nonadiabatic modes of motion. *Phys. At. Nucl.*, 70:1628–1633, 2007.

[66] A. G. Smith, G. S. Simpson, J. Billowes, P. J. Dagnall, J. L. Durell, S. J. Freeman, M. Leddy, W. R. Phillips, A. A. Roach, J. F. Smith, A. Jungclaus, K. P. Lieb, C. Teich, B. J. P. Gall, F. Hoellinger, N. Schulz, I. Ahmad, J. P. Greene, and A. Algora. Correlated spins of complementary fragment pairs in the spontaneous fission of ^{252}Cf. *Phys. Rev. C*, 60:064611, 1999.

[67] L. G. Moretto and R. P. Schmitt. Equilibrium statistical treatment of angular momenta associated with collective modes in fission and heavy-ion reactions. *Phys. Rev. C*, 21:204–216, 1980.

[68] J. R. Nix. Further studies in the liquid-drop theory on nuclear fission. *Nuclear Physics A*, 130(2):241–292, 1969.

[69] J. Randrup. Transport of angular momentum in damped nuclear reactions. *Nucl. Phys. A*, 383(3):468–508, 1982.

[70] L. G. Moretto, G. F. Peaslee, and G. J. Wozniak. Angular-momentum-bearing modes in fission. *Nucl. Phys. A*, 502:453–472, 1989.

[71] J. Randrup and R. Vogt. Refined treatment of angular momentum in the event-by-event fission model FREYA. *Phys. Rev. C*, 89:044601, 2014.

[72] J. Randrup and R. Vogt. Generation of fragment angular momentum in fission. *Phys. Rev. Lett.*, 127:062502, 2021.

[73] J. Randrup, T. Døssing, and R. Vogt. Probing fission fragment angular momenta by photon measurements. *Phys. Rev. C*, 106:014609, 2022.

[74] A. Bulgac. Fission-fragment excitation energy sharing beyond scission. *Phys. Rev. C*, 102:044609, 2020.

[75] K. H. Schmidt and B. Jurado. Final excitation energy of fission fragments. *Phys. Rev. C*, 83:061601, 2011.

[76] A. N. Bohr and B. R. Mottelson. *Nuclear Structure (In 2 Volumes)*. World Scientific Publishing Company, 1998.

[77] J. Sprenger and N. Weinberger. Simpson's Paradox. In Edward N. Zalta, editor, *The Stanford Encyclopedia of Philosophy*. Metaphysics Research Lab, Stanford University, 2021.